Study of effect of deformation & irradiation on the microstructure of fcc materials using X-ray diffraction

By

SANTU DEY

Enrolment No: PHYS04201304011

VARIABLE ENERGY CYCLOTRON CENTRE

1/AF BIDHAN NAGAR

KOLKATA - 700064 INDIA

Homi Bhabha National Institute[1]

Recommendations of the Viva Voce Committee

As members of the Viva Voce Committee, we certify that we have read the dissertation prepared by Santu Dey entitled "Study of effect of deformation & irradiation on the microstructure of fcc materials using X-ray diffraction" and recommend that it may be accepted as fulfilling the thesis requirement for the award of Degree of Doctor of Philosophy.

Chairman – Dr. Paramita Mukherjee, VECC, Kolkata	P Mukherjee 18/12/2020
Guide / Convener – Dr. Gayathri N. Banerjee, VECC, Kolkata	Gayathri N. 18/12/2020
Co-guide -	
External Examiner - Prof. Bankim Chandra Ray, NIT, Rourkela	18/12/2020
Member 1- Dr. Pintu Sen, VECC, Kolkata	Pintu Sen 18/12/2020
Member 2- Dr. Prabhat Mondal, SINP, Kolkata	P. Mondal 18/12/2020
Member 3- Dr. Tapatee Kundu Roy, VECC, Kolkata	Tapatee Kundu 18/12/2020

Final approval and acceptance of this thesis is contingent upon the candidate's submission of the final copies of the thesis to HBNI.

I/We hereby certify that I/we have read this thesis prepared under my/our direction and recommend that it may be accepted as fulfilling the thesis requirement.

Date: 18/12/2020

Place: Kolkata

Signature
Co-guide (if any)

Gayathri N.
Signature
Guide

[1] This page is to be included only for final submission after successful completion of viva voce.

A thesis submitted to the

Board of Studies in Physical Sciences

In partial fulfillment of requirements

for the Degree of

DOCTOR OF PHILOSOPHY

of

HOMI BHABHA NATIONAL INSTITUTE

SEPTEMBER 2020

STATEMENT BY AUTHOR

This dissertation has been submitted in partial fulfillment of requirements for an advanced degree at Homi Bhabha National Institute (HBNI) and is deposited in the Library to be made available to borrowers under rules of the HBNI.

Brief quotations from this dissertation are allowable without special permission, provided that accurate acknowledgement of source is made. Requests for permission for extended quotation from or reproduction of this manuscript in whole or in part may be granted by the Competent Authority of HBNI when in his or her judgment the proposed use of the material is in the interests of scholarship. In all other instances, however, permission must be obtained from the author.

Santu Dey.

(SANTU DEY)

Name & Signature of the student

DECLARATION

I, hereby declare that the investigation presented in the thesis has been carried out by me. The work is original and has not been submitted earlier as a whole or in part for a degree / diploma at this or any other Institution / University.

Santu Dey.
(SANTU DEY)

Name & Signature of the student

List of Publications arising from the thesis

Journal

Related to Thesis:

a. Published:

1. S. Dey, N. Gayathri, M. Bhattacharya, P. Mukherjee, In situ XRD studies of the process dynamics during annealing in cold-rolled copper, Metall. Mater. Trans. A. 47 (2016) 6281–6291.doi:10.1007/s11661-016-3768-0.

2. S. Dey, N. Gayathri, P. Mukherjee, Depth profiling of ion-induced damage in D9 alloy using X-ray diffraction, Radiat. Eff. Defects Solids. 173 (2018) 300–317.doi:10.1080/10420150.2018.1438435.

b. Communicated:

1. S. Dey, N. Gayathri, A. Dutta, P. Mukherjee, Binoy K Maji A novel approach to analyse combined pre and post strain rate dependent phase transformation in tensile deformed SS304 using XRD and EBSD;**Communicated to Materials Science & Engineering A.**

Not Related to Thesis:

a. Published:

1. S. Dey, A. Dutta, P. Mukherjee, N. Gayathri, A.D. Gupta, T. Roy, Characterization of ion induced damage as a function of depth in proton irradiated pure Ti and Ti--6Al--4V, J. Alloys Compd. 821 (2020) 153441. doi:10.1016/j.jallcom.2019.153441.

2. A. Giri, S. Dey, P. Barat, Effect of temperature on the complexity of solid Argon system, Indian J. Phys. 90 (2016) 725–732.doi:10.1007/s12648-015-0803-8.

3. A. Dutta, N. Gayathri, P. Mukherjee, S. Dey, S. Mandal, T.K. Roy, A. Sarkar, S. Neogy, A. Sagdeo, An approach in the analysis of microstructure of proton irradiated T91 through XRDLPA using synchrotron and laboratory source, J. Nucl. Mater. 514 (2019) 161–170.doi:10.1016/j.jnucmat.2018.11.038.

b. Communicated:

1. A. Dutta, S. Dey, N. Gayathri, P. Mukherjee, T.K. Roy, A. Sagde, S. Neogy, Microstructural evolution of proton irradiated Fe-2.25Cr-1Mo characterized using synchrotron XRD (SXRD); **Communicated to Radiation Physics and Chemistry.**

2.A.K. Pattanaik, S. Dey, A. Dutta, B.K. Maji, N. Gayathri, N. Kumar, P. Mukherjee, Deformation in Nitronics-40 alloy - characterization of microstructural changes during cold and cryo rolling; **Communicated to Metallurgical and Materials Transactions A.**

Conferences

Related to Thesis:

1. S. Dey, N. Gayathri, P. Mukherjee, and M. Bhattacharya, "The evolution of stored energy during recrystallization along different crystallographic planes in textured electrolytic copper," in *National Conference on Current Trends in Advanced Materials (CTMat-2014)*, 2014, p. 136.

2. S. Dey, N. Gayathri, and P. Mukherjee, "Characterization of ion induced damage as a function of depth using XRD," in *Natinal Symposium of Radiation Physics (NSRP-21)*, 2018, p. 125

3. 3. S. Dey, N. Gayathri, P. Mukherjee, A. Dutta, Pattanaik, and A.K., "The effect of pre-strain and the strain rate on the martensitic phase transformation in SS304," in *International Conference on Current Trends in Materials Science and Engineering (CTMSE)*, 2019, p. 68.

Not Related to Thesis:

4. S. Dey, A. Dutta Gupta, N. Gayathri, and P. Mukherjee, "Depth profiling of proton induced damage in Ti-6Al-4V using X-ray diffraction," in *72nd Annual Technical Meeting of IIM*, 2018, p. 459.

5. S. Dey, P. Mukherjee, N. Gayathri, A. Dutta, and A. K. Pattanaik, "Microstructural study of O6+ irradiated Ti-6Al-4V using XRD Line Profile Analysis," in *International Conference on Nanostructuring by Ion Beams (ICNIB)*, 2019, p. P-15.

Santu Dey.
(SANTU DEY)

Name & Signature of the student

Dedicated to my Parents

&

my teacher

Late Tapas Kumar Modak

ACKNOWLEDGMENTS

It is my great pleasure to acknowledge my supervisor **Dr. Gayathri N. Banerjee** for her academic and personal guidance and constant encouragement during the course. Her consistent involvement in the work and perpetual enthusiasm in discussions had always been a stimulant for me. She was always available to share her deep appreciation of a wide variety of subjects and I have benefitted a lot from the discussions I had with her.

I also express my sincere gratitude to **Dr. Paramita Mukherjee**, Head of the Material Science Studies Division (MSSD) to share her academic knowledge and guide me as my co-guide in my Ph.D. period. She also gave her valuable time to encourage me in my study and suggestion to improve the work quality. I am also grateful to **Dr. P. Barat and Late Dr. M. Bhattacharya** for their academic support to my work. I would like to acknowledge all the **members** of my **Ph.D. evaluation committee** for their valuable suggestion and guidance to focus in my study. It is a great feeling to be a part of MSSD in VECC and I sincerely thank my **Division's members Dr. S.K. Bandyopadhyay, Dr. P. Sen** and **Mr. A. K. Himanshu**. I am grateful to **Dr. Jane Alam**, Head of the Physics Group, VECC for his support and valuable suggestions. I would like to thank **Dr. Parnika Das, Dean Academic, VECC** for her support in official work related to PhD. I must extend my heartiest thanks to **Nilangshu Da, Sanjoy Da, Apu Da, Arnomitra Di, Prasun Da, Ashit Da, Binoy Da, Amal, Kalipada, Argha, Sudipta, Sujan, Sandipan, Nilanjan, Ekata** and **Sinjini** for their academic support and being with me as a friend in any situation to encourage and complete my study. Also I want to acknowledge **Arun Da** and **Pratik** for their invaluable help to carry out the experiment. I would also like to thank all of my **Friends** in different stages of my life for their support to overcome many difficult situation and endless encouragement. My sincere gratitude to **Prof. Prabhat Mandal** and **Moumita** for helping me to carry out experiments using their facility.

I am also grateful to my teacher **Late Mr. Tapas Kumar Modak**, who has taught me at graduate level and shared his very good understanding in physics which motivated me to accomplish my research work.

I also acknowledge my **sister**, **relatives** and **my native villagers** for their constant support from my childhood and for believing in me.

Finally, it is my great opportunity to thank my **parents** for their full selfless support and always be the first person to share their helping hand in any stage of my life. Their great support and encouragement gave me maximum confidence to overcome any difficulties.

My sincere apologies to all those whom I might have missed acknowledging but have been there to encourage me to complete the thesis despite all odds.

Santu Dey.

(Santu Dey)

Contents

List of Figures

List of Tables

Chapter 1

General introduction of deformation, irradiation and annealing induced microstructural changes in metals and alloys

1.1 Introduction:

Microstructure of a material in general, is described by the grain size, description of their structure, size and shape distributions, types of phases present, grain boundaries, hetero-phase inter-phases, dislocations and point defects such as vacancies, interstitials and substitutions. This can in principle be controlled during the metal forming process (which includes both deformation and annealing). However, in-service conditions the microstructure may get altered which in turn affect the properties of the material. Deformation and particle irradiation are two such processes among others during which changes in the microstructure of the material can occur. The effect of this microstructural change on the physical properties may be either beneficial or detrimental. To achieve the desired final properties of the material for a particular application and to understand the changes during in-service conditions, it is required that a comprehensive knowledge of the material be gathered beforehand.

During deformation and subsequent annealing the microstructure is modified due to the arrangement, agglomeration, pileup, annihilation and rearrangement of the defects and also the formation of new defect free grains and its growth [1]. On the other hand, during

irradiation by an energetic ion, the microstructure is altered due to the formation of the point defects and subsequently their agglomeration to form vacancies/interstitial clusters, dislocation loops, voids etc. [2]. Formation of new crystallographic phases has also been observed during deformation and irradiation when the favourable condition for the phase transformation is achieved [1,2]. Hence, understanding the microstructural changes and the phase transformations occurring during deformation and irradiation is utmost important for physicist, metallurgist, materials scientists and others involved in the pursuit of study of materials and their applications. This multi-disciplinary field is not only academically important but also has high industrial relevance.

1.2 Experimental Background:

X-ray diffraction (XRD) has evolved as an important analytical tool for characterisation of materials. After the discovery of X-ray by Rontgenin1895, rigorous experiments were conducted in many labs over few decades before scientists could comprehensively understand the nature of interaction of this ray with matter. One of the major breakthroughs was the discovery of diffraction of these rays from crystals by Max von Laue for which he was awarded the Nobel Prize in 1914 [3]. Besides the extensive application of XRD to study the crystallographic structure of materials, this technique has advanced as a distinctive tool for obtaining the statistically averaged information of the microstructural features of polycrystalline materials. The details of the early studies on this indirect technique for characterising the microstructure has been reviewed by Greenaugh [4], Warren [5] and De and Sengupta [6] and references there in. In this thesis, the capability and versatility of X-ray diffraction as a technique for phase and microstructural characterisation of materials have been exploited to understand some of the pertaining problems in deformation and irradiation of materials. In this study, several line profile analysis techniques (that have been developed so far) have been judiciously employed to understand the various aspects of the

microstructural features of materials [7–12].This analysis has several advantages over the traditional transmission electron microscopy in the investigation of the microstructure of materials and is being used as a complementary tool for several decades [13]. It has the advantages of giving the statistically averaged information about the microstructure from about a volume of 10^6 μm^3 to 10^9 μm^3 of the sample.

The microstructural results obtained from the XRD have been supported by the direct observation of those features using different electron microscopy techniques. In 1931 Ernst Ruska and Max Knoll, fabricated the first electron microscope from the University of Berlin [14]. This invention opened new fields of research for characterisation of materials using electrons as a probe. In 1933, Ernst Ruska developed a new model of the electron microscope which was capable of producing high resolution images [15,16]. Max Knoll created the first Scanning Electron Microscope (SEM) which as subsequently improved by Manfred von Ardenne [17]. However, the commercial version of the instrument was development by Prof Charles Oatley during 1950's and 1960's and he is credited as the father of SEM. The images were displayed on a CRT screen by synchronizing the scanning of the electron beam in the microscope and that of the display. The resolution of the microscope was reported to be between 10nm to 100 nm. Recent advances in improving the electron optics along with the replacement of the electron source by a field emission gun have greatly enhanced the resolution of the SEM (1-4nm). This has extended the applicability of the SEM from observing surface topography to carry out more detailed microstructural analysis of materials. The technique of Electron Back Scattered Diffraction (EBSD) using FESEM where the Kikuchi pattern is captured in a fluorescent screen and further analysed to obtain various microstructural features [18–20]. These include individual grain orientations, local texture, point to point orientation correlation and phase identification and distribution to name a few [18–20]. The high resolution EBSD data has been used for mapping localised strain

distributions on surfaces. Understanding the origin of the localised strains in terms of defects and their spatial configuration has added valuable knowledge to correlate the microstructure with the property of the material [20]. By correlating the observed EBSD pattern with the theoretically calculated one, the role of the collective effects of the dislocations on the sampled area can be inferred [18–20].Thus XRD and EBSD techniques are powerful complementary tools for characterising the microstructure of materials.

In addition, other characterisation tools such as optical microscopy, Differential scanning calorimetry (DSC) and Magnetic moment measurement using vibrating sample magnetometer (VSM) have also been used to supplement the results obtained using XRD and EBSD.

1.3 Deformation and Ion Irradiation:

In engineering, a change in shape or size of an object is referred to as deformation. Concurrently, in physics, the continuum mechanics transformation of an object from an earlier configuration to a current configuration is termed as deformation. This is an unavoidable phenomenon which the materials have to undergo either during the forming process (e.g. Tensile, Rolling, Forging, Extrusion, drawing etc.) or during in-service condition and hence may be both intentional and undesirable. When a material is deformed using an applied stress, the various stages that it passes through (in particular metals and alloys) can be categorize das: elastic stage, yield stage, uniform plastic stage, and necking stage which follows sequentially with increasing stress. Elastic stage refers to the 1st stage of deformation which occurs at low stress values, where the stress-strain relationship is linear and the deformed material returns to its original shape when the stress is removed. In the intermediate stages of stress (yield stage and uniform plastic stage) the deformation is permanent but uniform. At the final stage of stress (necking stage), material develops a crack,

which then grows locally with increasing stress and finally fractures through necking. Another type of classification of deformation is also generally accepted which depends on the nature of applied force or stress on the material. These are uniaxial deformation (e.g. compression and elongation), biaxial deformation (e.g. rolling), triaxial (hydraulic) and multiaxial deformation. The parameter that is generally used to define the amount of deformation depends on the process i.e., in tensile or compression "strain- change in length by the original length" and in rolling "percentages of thickness reduction" is considered as the measurement of deformation. During the metal forming process, the desired final properties of the material are achieved by controlling the deformation and the intermediate annealing stages. Thus understanding the combined effect on the material property and its controlling parameters are required to be understood before a material can be put to practical use.

Irradiation is the general term used for the process of exposing matter to ionizing radiation originating from various sources [2,21]. Ion irradiation is a subset of this wherein, energetic particles originating from an accelerator are used for modifying, characterising etc., the material [2]. A charge particle accelerated and focussed on to a target can be used as a viable tool for material modification, diagnostic, damage and also for probing exotic nuclei depending on the ions energy. Among its various applications in materials science, the one of significant importance is radiation damage studies of nuclear structural materials. Easy availability of accelerators with varying ion species and with different energies, make ion irradiation as a very reliable technique for emulating neutron damage in materials used in nuclear reactors. This has been recognized as a standard technique for investigating the effects of neutron radiation damage on materials that are used in and around the core of nuclear reactors [22]. Apart from shorter irradiation time compared to that of neutrons the major advantage of using ion irradiation is the reduced or no induced radioactivity of the

samples. This enables one to carry out almost immediate characterisation of the irradiated materials. By choosing the ion species, energy, dose, dose-rate and temperature of irradiation, one can achieve one to one correspondence with neutron damage using the ion irradiation [2].

1.4 Microstructure and Defects:

Microstructures of a material (defined in section 1.1) are small-scale structures which play a deterministic role in influencing some of the major physical and mechanical properties of the material. Properties like melting point, thermal expansion coefficient, specific heat, elastic constants etc. are independent of the microstructure of the materials but resistivity, ductility, toughness, yield stress, ultimate tensile strength etc., are strongly influenced by the microstructure [23].

During in-service condition, the microstructure of the material may be modified due to production of new defects which may now tend to modify the material property. In order to understand the changes caused by the defects, it is worthwhile to recapitulate the types of defects and their effect on microstructure.

Any type of deviation from the perfectly arranged regular array of atoms in the crystal structure is called a defect. Defects are generally categorized depending on their dimension as follows (i) Points defects such as vacancies, interstitials, impurities, anti-site atoms etc. are zero dimensional (ii) Dislocations or line defects are one dimensional (iii) Surface defects such as grain boundaries, stacking fault, twinning etc. are two dimensional and (iv) Volumetric defects such as void, precipitates of new phase, stacking fault tetrahedra, tight cluster of dislocations, are three dimensional. All of these defects cause distortion of the regular array of atoms causing a stress field around it. This field dictates the interaction of the defects with similar or dissimilar type of defects and hence plays an important role in the movement and re-arrangement of the defects during deformation or irradiation.

Point defects (vacancies and interstitials) are the only thermodynamically stable defects found in materials. The thermal activation of these defects is driven by the reduction in the total free energy of the material due to their formation. However, the concentration of these defects at a given temperature is dictated by their formation energies. In general, for a given crystallographic structure the formation energy of an interstitial is few times more than that of a vacancy which leads to the equilibrium concentration of vacancies to be ~ 10^5 more than that of interstitials. However, deformation (under special conditions) and irradiation produces vast amount of point defects thus increasing the concentration much beyond the thermodynamically stable value [2,24]. The excess defects can then diffuse, migrate and agglomerate to form higher dimensional defects such as dislocations, voids, precipitates etc. The agglomeration is driven by the local stress fields and concentration gradient of the defects.

Dislocations or line defects can directly form during deformation and indirectly during irradiation. The existence of simplest type of dislocations was suggested by Orowan, Polanyi and Taylor [23,25–27] and were called edge dislocation or Taylor-Orowan dislocations. The mismatch between theoretical and experimental values of shear modulus of the material could only be explained by introducing the concept of dislocation. The presence of dislocation was first experimentally observed in 1950 by Transmission Electron Microscopy (TEM) [28]. Dislocations are primarily of two types, edge or screw depending on the relation between the direction of the lattice distortion (called the Burger's vector) with respect to dislocation line (which runs along the core of the dislocation) [29]. However, in real materials, the dislocations are typically of mixed type i.e. having both the edge and screw character. Dislocations play a major role in the deformation process and control the plastic deformation of a material. When a material is deformed, the dislocations flow through the material dominated by slip mechanism, leading to the ductility of the materials. New

dislocations (either straight or loops) are created and as a consequence the increasing overlap of the strain fields of the adjacent dislocations gradually increases the resistance to dislocation motion causing strain hardening of the material. When more dislocations are formed, they interact more strongly and can eventually pile-up, re-arrange and can form dislocation tangles or small angle sub-grain boundaries. All these can change in the microstructure of the material. During irradiation, dislocation loops (vacancy type or interstitial type) are formed when same type of point defects agglomerate into clusters and eventually collapse or rearrange into loops. These are one of the major irradiation produced defects which control the microstructure and eventually the properties of the material during further irradiation.

Formation of deformation twins and stacking faults are also important microstructural changes that occur during the deformation of a material. The competitive process of twinning (in relation to slip) is dominant in certain crystal systems and under certain conditions. Twinning is a special way of accommodation of deformation strain especially seen in materials where the number of participating slip systems are lower than five independent slip systems required to satisfy the Von Mises criterion for a general deformation of polycrystals (mainly in bcc and hcp materials). Even though fcc materials have a large number of slip systems, they too show formation of twins if the deformation is carried out at low temperature or at high strain rate which prevents activation of required number of slip systems for slipping. Experiments have shown that in bcc and hcp metals and alloys twins often form at very low plastic strain level, whilst fcc metals do not generally twin until appreciable plastic deformation by slip has occurred [30]. Twinning occurs when certain portion of the crystal lattice rearranges itself to form the mirror image of the parent lattice. In polycrystals, because of the favourable stress concentrations and defects most twins nucleate at grain boundaries.

In materials with high stacking fault probability (i.e., with low stacking fault energy), the energy which is pumped into the material is accommodated by the formation of stacking faults in the lattice. Stacking faults are defects which are defined as sudden deviation from the regular arrangement (stacking) of crystallographic planes in a crystal and thus fall under the category of planar defects. Most commonly stacking faults are observed in the closed pack fcc structure which converts to a hexagonal structure in the faulty region. However, there are instances of formation of stacking faults in bcc materials also, even though they are energetically highly unfavourable due to the lack of stacking sequence in the structure unlike fcc and hcp.

Shear bands are commonly observed microstructural feature in a severely deformed material. These are highly concentrated dislocation flow regions in a narrow deformation zone extending over many grains. These usually occur when homogenous dislocation slip is prohibited or when insufficient slip systems are available for deformation to occur and are generally observed in low stacking fault materials. However, they are usually observed in ductile materials throughout the deformation region. Due to the strain localization these shear bands are detrimental to material processing causing sudden softening of the material and thus failure. However, due to their high dislocation densities and large misorientation with the surrounding matrix intersecting shear bands provide an ideal site for nucleation of recrystallization or nucleating sites for new phases (e.g., deformation induced martensite) [1,24].

The formation of 3D defects such as voids and stacking fault tetrahedra require special conditions [2,23]. During deformation at high temperature, where there is excess concentration of vacancies, the voids are seen to form at grain boundary junctions [23]. However, during irradiation, the excess vacancies that are left behind after the preferential absorption of interstitials (in the sinks) may combine to form voids [2]. These voids cause

volumetric changes in the material and hence are highly detrimental to material properties. The three dimensional version of the stacking faults are the stacking fault tetrahedra which are also formed in fcc materials under special conditions during deformation, melt-quenching or irradiation [2,23].

1.5 The effect of deformation on the materials:

The materials that are used in our daily life or in any industrial application are polycrystalline in nature. Polycrystalline materials are made up of many grains with different orientation and this directly affects the deformation process. Dislocation movement play the crucial role in any type of plastic deformation, which depends on the slip systems present in that material. It is well known that there are preferred crystallographic planes in different crystal structures for dislocation slip or glide [29]. The combination of the set of symmetrically identical slip planes and associated family of slip directions in which dislocation motion can easily occur during plastic deformation is called the slip system. The fcc crystal has in total 12 nos. of {111}<110> slip systems with {111} plane being the closely packed plane and <1-10> being the high dense direction in that plane. Though bcc has a total 48 nos. slip system of {110}<111>, {112}<111> and {123}<111> it does not have any closed placed plane. On the other hand, in hcp has a total 3 numbers slip systems of {0001}<1120> (with large c/a ratio) with {0001} as the closed packed plane. At a given temperature, the availability of active slip systems determines the ductility of the material. At ambient temperature, fcc structure has enough number of slip systems to satisfy the von Mises criteria which makes all fcc materials to be ductile. Though bcc has 48 slip systems most of them are inactive at ambient temperature making bcc crystal brittle in most cases. The hcp crystal inherently has only a very few numbers of slip systems and thus remains brittle at ambient temperature. Thus, in the material where enough slip systems are not available or at low temperature when slip

systems are not active or at high deformation rate when slip system does not get time to activate, twinning and shear bands are formed to accommodate the deformation.

The relationship between stacking fault energy and the mode of deformation can be summarized as follows. In fcc materials with high and medium stacking fault energy (Aluminium~ 200 mJ/m^2 and Copper ~ 78 mJ/m^2) the deformation is accommodated by slip rather than by formation of stacking faults and twins [1]. In materials with low stacking fault energy such as silver ~ 20 mJ/m^2 the preferred mode of deformation is by twinning (aided by the formation of stacking faults). It is important to address the evolution of deformation microstructure in metals in terms of dislocation arrangement. The deformation in a material is accommodated by the multiplication and migration of dislocations. At low strains the distribution of dislocations is random and with increasing deformation, depending on the SFE of the material, the dislocations either form planar array of SFs, or remain as dislocation tangles or arrange to form cells or subgrains [1]. In high and medium SFE materials, a balance between the production of large dislocation densities in the slip plane and the decreasing energy due to formation of dislocation boundaries promotes the formation of cells or subgrain boundaries. This is usually called dynamic and/or static recovery [1]. This depends on the nature of the material and the deformation temperature. For example, in Aluminum (high SFE and low melting point) the deformation at room temperature causes the formation of subgrains due to dynamic recovery [1]. On the contrary in copper (medium SFE, reasonable high melting point) the microstructure consists of mainly cells because dynamic recovery in much less compared to Aluminium [1]. In low SFE materials, no dislocation cell structure is formed since the preferred mode of deformation is twinning.

Apart from the formation of twins and shear bands one of the other main microstructural change that happens is the formation of deformation texture (grain orientation). Texture or preferred orientation is a consequence of the fact that deformation

occurs on the most favourably aligned slip system and twinning is formed in order to align the slip systems (to make dislocation movement easy along a particular direction) by the repositioning of atoms [1,23].

Microstructural changes in alloys can also be induced by phase transformations. Most of the phase transformations in general are thermally activated and hence occur at high temperature. However, non-thermally activated phase transformation is becoming important in some ferrous and nonferrous alloys and is induced by deformation of the material [31]. Deformation-induced phase transformations commonly occur during processing or in-service of parts made from steels or non-ferrous alloys. Recent research activities have been directed to utilize this phase transformation as an advantage in improving the properties of the materials example being the transformation induced plasticity steel being developed for outstanding combination of strength and ductility [32]. Since the mechanical properties of the material are determined by the microstructural features, it is important to understand the changes that occur during the phase transformation.

Elastic and plastic deformation in most cases do not induce a change in crystal structure however, the deformation induced martensite phase transformation seen in some steels is an example.

All the above microstructural changes that happen during deformation alter the stored energy in the material. During deformation only around 1% of the total energy is stored inside the material and remaining goes to produce heat [1]. The driving force for all the property changes is provided by this stored energy. If the deformation is carried out at ambient temperature, almost all the stored energy is accommodated in dislocations and their various arrangements. The grain shape change, grain orientation, formation of twins, stacking faults, shear bands, voids and formation of different internal structures within the grain i.e.,

dislocation tangles, sub-grain boundaries etc., are all features which contain the stored energy of deformation in the material. The determination of this stored energy is not easy and is usually measured directly by calorimetry or by X-ray diffraction technique. Indirectly this quantity is measured by changes in physical or mechanical property of the material [1].

1.6 The effect of ion irradiation on the material:

Radiation damage is a branch of ion irradiation study where the energy and momentum transferred to the target atom by an energetic particle, displaces it from its original position. This displaced target atom is called the primary knock on atom (PKA) gives rise to a cascade consisting of secondary knock-ons, tertiary knock-ons and so on. Meanwhile, the projectile moves along the depth of the material and continues to create further PKA until its energy decreases below a value required to create a knock on. At the end of this range(the projected distance up to which one incident projectile penetrates before losing its full energy), it ends up as an interstitial or a substitutional atom [2].This disturbance in the regular array of atoms, results in the production of a large number of vacancies and interstitials which eventually dictate the microstructure of the irradiated material. This is called radiation damage and is specifically important for the study of core structural materials of a nuclear reactor [2].

The energy of the incident ion travelling through the lattice is generally lost by electronic, nuclear and radiation processes. In the energy regime where radiation damage is generally observed, radiation loss is negligible in comparison to electronic and nuclear losses [2]. Among the other two processes, nuclear energy loss is the primary means for causing damage in the material and is dominant only at lower energies of the incident ion and the electronic energy loss is dominant at higher energies only ($\sim E^{1/2}$). However, there is no clear energy boundary between these two losses. Since the nuclear stopping power is maximum at low energy of the incident particle, the maximum number of defects is produced very close to

the range of the incident ion. The first calculation of the numbers of displacement by the PKA was formulated by Kinchin and Pease (K-P model) based on certain assumptions [2]. In the K-P model the total number of defects created by a PKA with energy T is calculated as follows [2]-

$$\left.\begin{aligned} \upsilon(T) &= 0, \quad \text{for } T < E_d \quad \text{Here, } E_d \text{ is the atomic displacement energy} \\ &= 1, \quad \text{for } E_d < T < 2E_d \\ &= \frac{T}{2E_d}, \text{ for } 2E_d < T < E_c \\ &= \frac{Ec}{2E_d}, \text{ for } T \geq E_c \end{aligned}\right\} \quad \textbf{(1.1)}$$

To overcome some of the deficiencies of this model, Norgett, Robinson and Torrens [2] suggested a modified atomic displacement model (known as NRT model) as follows

$$N_d = \frac{kE_D}{2E_d} = \frac{k\,(T-\eta)}{2E_d} \qquad (\mathbf{1.2})$$

Where N_d *is* the numbers of displacements driven by the PKA, E_D is the damage energy, energy available to generate atomic displacements by elastic collisions, T and E_d are the PKA and atomic displacement energy respectively (as mentioned above) and η is the lost electronic energy by electron excitation in the displacement cascade. k iscalled the displacement efficiency with a value of 0.8 and independent of temperature [2].

During irradiation, the formation of a stable Frenkel pair (vacancy-interstitial pair) takes 10^{-11} sec within the material but the defect reaction starts after a time scale of greater than 10^{-8} sec. There are many factors which control the final defects concentration in the material including defects production rate, defect annihilation rate (recombination and absorption at sinks) type of defects, defects density, defects diffusivity (dependent on temperature) etc. Each defect interacts with others driven by the stress field around them. The

nature of the stress fields around the defect depends on the lattice position of defect (interstitial or substitutional position) and type of defect (vacancy or interstitial type). Opposite stress field always try to attract each other and same stress field causes repulsion among them. Defect reaction can cause either annihilation or agglomeration of the defects. During and after irradiation both defects annihilation as well as defect agglomeration starts to occurs. Annihilation of newly formed defects may occur between defects of opposite type (vacancy-interstitial) or with a sink already present in the material. Voids are formed due to vacancy agglomeration and new crystalline phase scan be created due to interstitial agglomeration. Due to the additional channels opening up for the diffusion of the defects due to irradiation (called radiation enhanced diffusion) segregation of the alloying elements may occur causing radiation induced segregation (RIS) [2]. Considering contribution of all factors the defect concentration rate equations can be written as [2] -

$$\frac{\partial C_V}{\partial t} = K_0 - K_{IV} C_I C_V - K_{VS} C_V C_S + \nabla . D_V \nabla C_V \qquad \textbf{(1.3a)}$$

$$\frac{\partial C_I}{\partial t} = K_0 - K_{IV} C_I C_V - K_{IS} C_I C_S + \nabla . D_I \nabla C_I \qquad \textbf{(1.3b)}$$

Where, K_0 = defect production rate; K_{IV} = vacancy–interstitial recombination rate coefficient; K_{VS} = vacancy–sink reaction rate coefficient and K_{IS} = interstitial–sink reaction rate coefficient; C_V & C_I are vacancy and interstitial concentration respectively; D_V & D_I are diffusion coefficient of vacancy and interstitial respectively. The left-hand sides of the above equations are the rate of change of concentration of vacancy ($\frac{\partial C_V}{\partial t}$) and interstitial ($\frac{\partial C_I}{\partial t}$) respectively. The first term in the RHS is the defect production rate; second and third terms are the annihilation with opposite defect type and sink respectively and the last term is the diffusion term due to the concentration gradient of the defects. Thus, the final defect concentration as a function of depth and dose in a material is critically determined by the presence of pre-existing sinks and the diffusion of the defects dominated by their

concentration gradient. We have already discussed the microstructural changes that are caused in a material due to irradiation in section 1.4. Hence, evaluating these changes as a function of dose and depth will help in endorsing the defect evolution in ion irradiated materials.

The above equation clearly indicates that diffusion of defects is the primary rate determining step in the evolution of the defects. The diffusion of the defects produced during irradiation occurs by several possible mechanism determined by the nature of the host lattice (mainly crystal structure) and the diffusing species. Experimentally, it was observed that there is a large difference in the defect accumulation in the fcc, bcc and hcp materials. The observation could not be explained by the dislocation bias model alone where it is assumed that dislocations are preferred sinks for interstitials [2]. This lacuna was overcome by the introduction of the production bias model [2]. The main assumptions in this model are that unequal amounts of freely migrating point defect and point defect clusters are produced in the damage cascade due to the differing pathways available for the migration of vacancies and interstitials. The movement of self-interstitials atoms (SIA) and the SIA clusters could be 1d, 2d or 3d depending on the crystal structure whereas that of vacancies is always 3d in any crystal lattice [2]. The absorption of the defects by dislocations is again determined by the nature of the migrating defects and the dislocation structure which also depends on the crystal structure. Thus, the crystal structure plays a decisive role in the damage accumulation and hence in determining the microstructural changes in ion irradiated material. It is already well known that bcc materials are more radiation resistant than fcc or hcp materials [2,33]. The final stable configuration of defects in the materials is driven by the need to lower the stored energy of the system which was increased during irradiation due to the production of the point defects. Thus, in an irradiated material the formation of point defect clusters and their

collapse to form higher dimensional defect structures such as dislocation loops, stacking fault tetrahedra or voids is due to the necessity to lower the overall energy of system.

1.7 Effect of annealing in deformed or irradiated material:

The thermodynamically unstable defects formed during deformation and irradiation should get spontaneously removed. However, most of them require thermal activation and hence require higher temperatures. Heating a material at high temperature enables the solid-state diffusion which can remove and/or arrange the defects in such a way that the total energy of the system reduces. This is known as annealing.

Annealing is the combination of three different processes (i) Recovery, (ii) Recrystallization and (iii) Grain growth [1]. Recovery is the process during which a material partially restores its microstructure and hence its mechanical properties which were lost during the process of deformation and irradiation. This recovery process is more or less homogeneous throughout the material but mainly modifies the internal structure of the grains rather than the grain boundaries. Recrystallization is the process where further restoration of microstructure as well as material properties can be achieved. New defect free grains are formed at the expense of the stored energy of the material which then grows further consuming the old grains which contain defects. The grain growth process increases the average grain size and decreases the grain boundary area by volume ratio to reduce the grain boundary energy [1]. All the three processes may occur homogeneously (known as the continuous annealing process) or heterogeneously (which is known as the discontinuous annealing process) throughout the material. The process of recovery and recrystallization may also occur during the deformation stage itself depending on the material property (its melting point, stacking fault energy) and the temperature at which the deformation is carried out; this is called dynamic recovery and dynamic recrystallization respectively. Since the process of

annealing restores some of the material properties, a metal forming process thus consists of a combination of deformation (e.g. forging, rolling, extrusion etc.) and heat treatment to achieve the desired property of the material before it is put to use. Hence the metal forming process is also called thermo-mechanical process. Thermal annealing studies of irradiated materials is important to reveal the presence of different defect clusters and understand the occurrence of radiation induced precipitates and dynamics of the vacancy clusters [2,34].

1.8 Deformation-irradiation and Crystal structure:

It is already well established and also discussed in section 1.5 and 1.6 that the deformation and the irradiation process are crystallographic structure dependent [1,2,23]. Different crystallographic structure has different numbers of slip systems (for deformation) or different diffusion pathways (for irradiation) which control the defect dynamics and finally the microstructure of the material.

In this thesis we have tried to address some of the unresolved problems related to the defect dynamics and phase transition in materials. The choice of a particular crystal structure is imminent from the various advantageous the fcc system offers from the experimental point of view. We have tried to utilize the XRD technique to critically address the problems and would like to choose a structure which is more symmetric nature. This leaves us with the choice of either fcc or bcc compared to hcp. Next, since we would like to address questions related to deformation and irradiation induced effects in the materials, we need to choose a material where the advantage of dislocation movement and the defect dynamics can be most conveniently studied. At ambient temperature, among fcc and bcc crystal structure, fcc offers the maximum number of active slip systems [29]. Also, irradiation induced defects such as vacancies and SIAs are more mobile at room temperature for most fcc materials [33]. Stage III recovery of the irradiation induced defects where both type of defects are highly mobile,

causes the formation of different defect clusters such as loops and SFT in fcc materials at ambient temperature and hence the signatures of these can be clearly ascertained using XRD technique [33].

Hence the choice of the crystal structure as fcc is driven by both the experimental technique used and the need to follow the dynamics of the defects (dislocations in the case of deformation and point defect and their clusters in the case of irradiation) at ambient temperature.

1.9 Different techniques to characterise the deformation and irradiation induced effects in materials:

Deformation and irradiation will affect the microstructure of any material which will change the properties of the material. Thus for the deformation and irradiation studies, proper characterising tools for determining the microstructure and material properties have to be employed. Microstructure characterisation e.g. measurement of grain size distribution, grain shape, twin boundary etc. can be carried out directly using optical or electron microscope. Microstructure details such as defects type, defect arrangement and concentration, crystallographic orientation etc. can be characterised indirectly by XRD, Positron annihilation spectroscopy (PAS), Electron back scattered diffraction (EBSD) by scanning electron microscopy, Transmission electron microscopy etc. On the other hand the characterisation of the material properties can be carried out using universal tensile testing, microhardness measurement, nano indentation measurements etc.

Direct microstructure measurement gives the visualisation of grain size, shape etc. but it is not enough to understand it in detail. Simple optical micrograph and the secondary electron image show only the grain distribution, twin boundary etc. The indirect XRD method measures the strain inside the materials, sub-grain structure (coherent domain),

orientation distribution function (ODF) of grains etc. which are the very important parameters to determine the material properties. Since XRD gives good statistically averaged information, this data is quite reliable to explain the material properties. PAS can be used to measure the selective depth wise concentration of defects and the type (or dimension) of defects. EBSD gives the idea of crystallographic orientation in a very small scale. This also gives the local misorientation which is connected to the coherent domain size in the material and the band contrast which is related to both domain size and the strain caused by the dislocations within the domain. Misorientation distribution also gives a rough idea about the stored energy in the material. Selected area diffraction measurements carried out using TEM gives the details characteristic of defects e.g. type and crystallographic position and orientation of the defects. All these indirect microstructure characterisation techniques give a details understanding of nature of defects and the arrangement of it.

Change in mechanical properties of the materials due to irradiation or deformation can be quantified using hardness, tensile test etc. Hardness measurement gives the different hardness (Brinel's, Vickers, Rock well etc.) of materials in a macro scale, as well as in micron scale. Localised micro-hardness measurement gives the possibility of measuring the hardness in a selective area of the microstructure. It is a very useful tool to determine hardness of different phases present in the material. Also tensile testing gives the strength and the ductility of the material which is very important properties for a material in service. This measurement give the Young's modulus, yield strength (Y_S), ultimate tensile strength (UTS), fracture toughness of materials. Some miniature sample use for the irradiation studies which also can be used for tensile test in a miniature tensile testing machine.

The details of all the techniques used in this thesis have been explained in the "Experimental" chapter.

1.10 Scope of this thesis-Motivation and materials selection:

In this thesis, we have tried to address some of the unaddressed highly relevant questions related to deformation and irradiation phenomena in fcc materials. The evolution of the microstructure during deformation, subsequent annealing and during irradiation is highly crucial study to understand the material properties in detail.

The three problems addressed in this thesis and the materials chosen to study each of them are summarized below.

1. Emulation of neutron damage in nuclear structural materials is being carried out routinely using ion irradiation. Simulation of the damage profile in the material using available Monte Carlo codes indicate that the damage is highly inhomogeneous along the range of the ion with the maximum damage occurring at the end of the range. However, it is well known that the diffusion of the defects is an important phenomenon that has to be considered while evaluating the properties of the ion irradiated material. The final microstructure will be dictated by the mobile defects, their annihilation in the pre-existing sinks and the formation and annihilation of new defect clusters as the irradiation proceeds. Hence it is important to evaluate the changes in the microstructure as a function of dose and as a function of depth. We have chosen to carry out this study on alloy D9 (Ti-modified SS316) which is an important nuclear structural material.

Stainless steel of SS316 series have been studied extensively for application as clad and wrapper applications in Na-cooled fast breeder reactors due to its good strength and compatibility with the coolant. 20 % cold work SS316 material has already been used as a core structural (clad and wrapper) material in Fast Breeder Test Reactor (FBTR) [35]. However, these steels show the phenomena of void swelling which limits its life time in the reactor and hence restricts achieving higher fuel burn up. Fine dispersion of Ti in SS316

(Alloy D9) helped alleviate this problem [36]. In alloy D9, fine particles of Ti carbide helps traps the vacancies thus preventing their agglomeration to form voids and hence improving the void swelling properties. This alloy also has lower creep rate and higher creep rupture strength than SS316 alloy [37]. More improved version of D9 alloy (IFAC-1) is being used as the clad material in the 1st Prototype Fast Breeder Reactor where optimising the titanium, phosphorous and silicon contents has improved the void swelling and creep resistance properties [38]. Normal alloy D9 has been used for our radiation damage study.

2. Deformation induced phase transformation (austenite to martensite) in stainless steel is being studied extensively for obtaining new materials with improved properties of strength and ductility [32]. The transformation induced plasticity (TRIP) steels can be tailor-made by controlling the deformation and annealing conditions to achieve the desired mechanical properties. The amount of martensite formed in a particular material depends on the temperature, strain rate and the sample history. Various studies have indicated that even though high strain rate helps in nucleating martensite at a lower strain the growth of the martensite is restricted [39]. On the contrary, it was also seen that at low strain rate, the nucleation of the martensite begins at a larger strain value but the growth is aided by the low strain rate thus helping to achieve larger martensite percentages [40]. In this thesis we have addressed the question as to what will be the effect of changing strain-rate and the strain-state on the percentage of martensite formed. In order to carry out this study, one needs to identify a material where the deformation induced martensite formation can be easily achieved at room temperature and within the deformation rates easily available in universal testing machines. After an extensive literature survey, SS304 was chosen for this purpose.

SS304 is the most popular among the stainless steels because of its high corrosion resistive property, good formability and welding property. This is an austenitic stainless steel containing approximately (18-20) weight percentages of Cr and (8-10) weight percentages of

Ni. In this steel Cr gives the corrosion resistance and Ni acts as an austenite stabilizer. It is very commonly used in nuclear industries at the nuclear fuel reprocessing plant and waste management plant. Nuclear fuel reprocessing plant normally uses nitric acid which is highly corrosive in nature, where SS304 is used because of its high corrosion resistive nature even in nitric acidic environment. Except of this use, SS304 is also used where corrosion is a crucial issue in the nuclear industry, mainly where water is in contact at high temperature service condition. This material is also used in many others industrial purposes mainly in food processing equipment, heat exchangers and marine applications.

3. Thermo-mechanical processing of materials is an important industrial procedure to arrive at the final product. During a metal forming process, a combination of deformation and annealing is chosen for a material to arrive at the desired final properties. It is already known that there is a large difference in the mobility of the defects in the different crystallographic planes of the fcc materials. Hence, it is important to understand and follow the recovery and the recrystallization process along the different planes to arrive at the right time scales for achieving the desired properties during the annealing stage of the thermo mechanical process. To show the importance, we have carried out the deformation and annealing study on fcc Copper. It is important to choose a material where the dynamics can be clearly followed by the available X-ray diffraction technique (to match with the time scales of the measurement).

Among the fcc materials, copper has the medium SFE and also reasonably high melting point (~1063°C). The combination of these two facts helps in accessing the annealing study near room temperature. Taking clue from the discussion presented in section 1.5 earlier, we can reason out this choice. Among the other available fcc materials, aluminium with high SFE has a low melting point (~630°C) and hence deformation at room temperature causes dynamic recovery. It is already reported that Aluminum shows the formation of subgrains after deformation at room temperature hence limiting the annealing study only to

recrystallization [1]. On the other hand, silver has a low SFE and the deformation is accommodated mostly as twins in the material. Hence, this material is also not a good choice since distinct recovery and recrystallization regions may not be observed due to the presence of the twins. So, the best choice is copper. Due to its medium SFE the dislocations are likely to remain as tangles or might form cells hence the dynamics of the dislocations can be clearly studied using the time scales and temperatures accessible in the laboratory [1].

This thesis is organized as follows: Chapter 2 outlines all the experimental tools and the analysis techniques used throughout this work. The depth wise assessment of the irradiation damage in alloy D9 is presented in Chapter 3. The Chapter 4 describes the uniaxial deformation study on SS304 and Chapter 5 contains the deformation and annealing study on cold rolled Copper. In Chapter 6, the final conclusion and future scope of the work are outlined.

Chapter 2

Experimental procedures and Methods of Analysis

2.1 Introduction:

An appropriate sample preparation and experimental procedure are essential to get experimental results with better accuracy. Standardisation of sample preparation procedure and planning experiments are big tasks as these greatly affect the parameters of interest. The thorough understanding of experimental procedures and selection of appropriate parameters is also very important since they affect the quality of the data. Proper analysis of data is also a crucial step to get the required parameters with minimum error. The best way of analysis depends on choosing the right methods for extracting the relevant information (microstructural parameters) from the data which comes from experience.

2.2 Sample preparation procedures:

The reason for choosing fcc materials for the studies in this thesis was discussed in detail in Chapter 1, section 1.8. The three works that have been addressed in this thesis required the preparation of the samples specific to the problem studied. We shall describe them in detail below.

2.2.1 Preparation of sample for irradiation study:

The first study addressed in this thesis involves the characterisation of the microstructure of ion irradiated material as a function of dose and depth. This work has been carried out on

alloy D9 (Ti-modified stainless steel) irradiated to different doses using 35 MeV α-particles from the Variable Energy Cyclotron at VECC, Kolkata. The alloy D9 was obtained in the form of rods of 30mm diameter. The rod had been prepared by hot rolling and then solution annealed at 1373 K for 30 min followed by water quenching. To carry out the irradiation, discs of 22 mm diameter and 1mm thickness were cut from the rod along the cross-section. These discs were fine polished before irradiation using an automated polishing machine Tegramin-25 (Fig. 2.1) with different grades of polishing cloths and SiC suspensions till a final mirror finish. This ensured that after irradiation, the front surface XRD study could be performed without any further sample preparation. It is essential because any type of sample preparation will remove the information available from the surface.

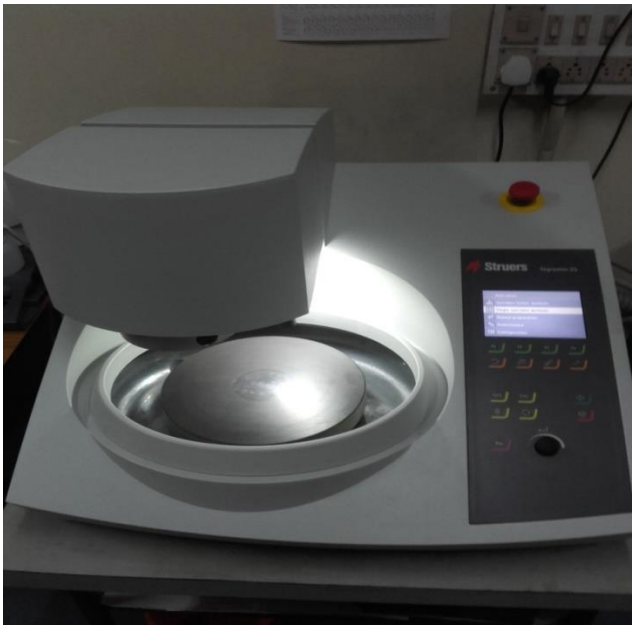

Fig. 2.1: Automated polishing machine

Irradiation was carried out at Channel 1 beam line of the Variable Energy Cyclotron as shown in Fig. 2.2.The sample was mounted on the centre of the aluminium flange (shown in Fig. 2.3 using a thin coat of silver paste and a collimator made of aluminium (with an opening of 20 mm diameter and 10 cm length) was used in front of the sample to hold the

Fig. 2.2: Channel 1 beam line of the Variable Energy Cyclotron

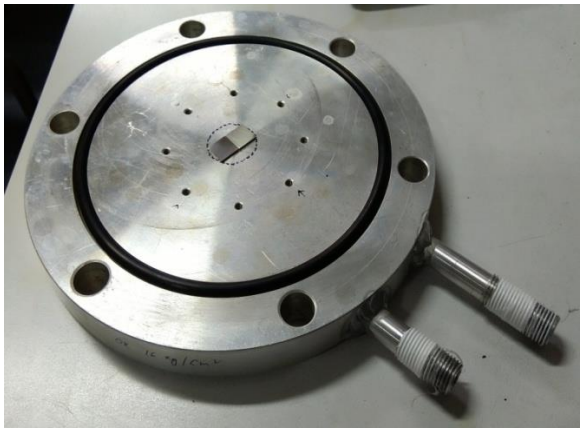

Fig. 2.3: Sample mounted on the Aluminium flange

Fig. 2.4: Diamond wheel cutter

sample as well as to collimate the ion beam. This collimator also served the purpose of secondary electrons suppressor since it was electrically connected to the target flange. The flange was continuously cooled by low conductivity water to remove the beam heating. This setup was electrically insulated from the beam line using a Perspex ring and the sample current was directly measured from the flange. The fluence of the ions required for calculating the irradiation dose was calculated using a current integrator. A small ring made of Macor was mounted on the front part the collimator which faced the beam, so the ions falling beyond the 20 mm opening of the collimator are not erroneously counted.

After irradiation, the samples with different doses were cut to dimension 10mm x 10mm using diamond wheel cutter (Fig. 2.4) for further study.

Different thickness has been accessed by systematic material removal using the same polishing machine with a rotating speed of 50 rpm and using 300 grade polishing paper. Care was taken regarding the sample heating during material removal. Further details of the depth wise sample preparation are presented in section 3.4.3, Chapter 3.

2.2.2 Preparation of samples for deformation study:

Deformation studies have been carried out using uniaxial tensile and biaxial rolling. The details of the sample preparation for each of the study are as follows:

The uniaxial deformation (tensile) study has been carried out on SS304 samples using the universal tensile testing machine (shown in the Fig. 2.5(a)). The tensile samples (shown in the Fig. 2.5(b)) of gauge length of 25 mm, width 10 mm and thickness 3 mm were prepared using the wire EDM machine available at VECC from the rolled sheet of SS304 as per ASTM standards [41].

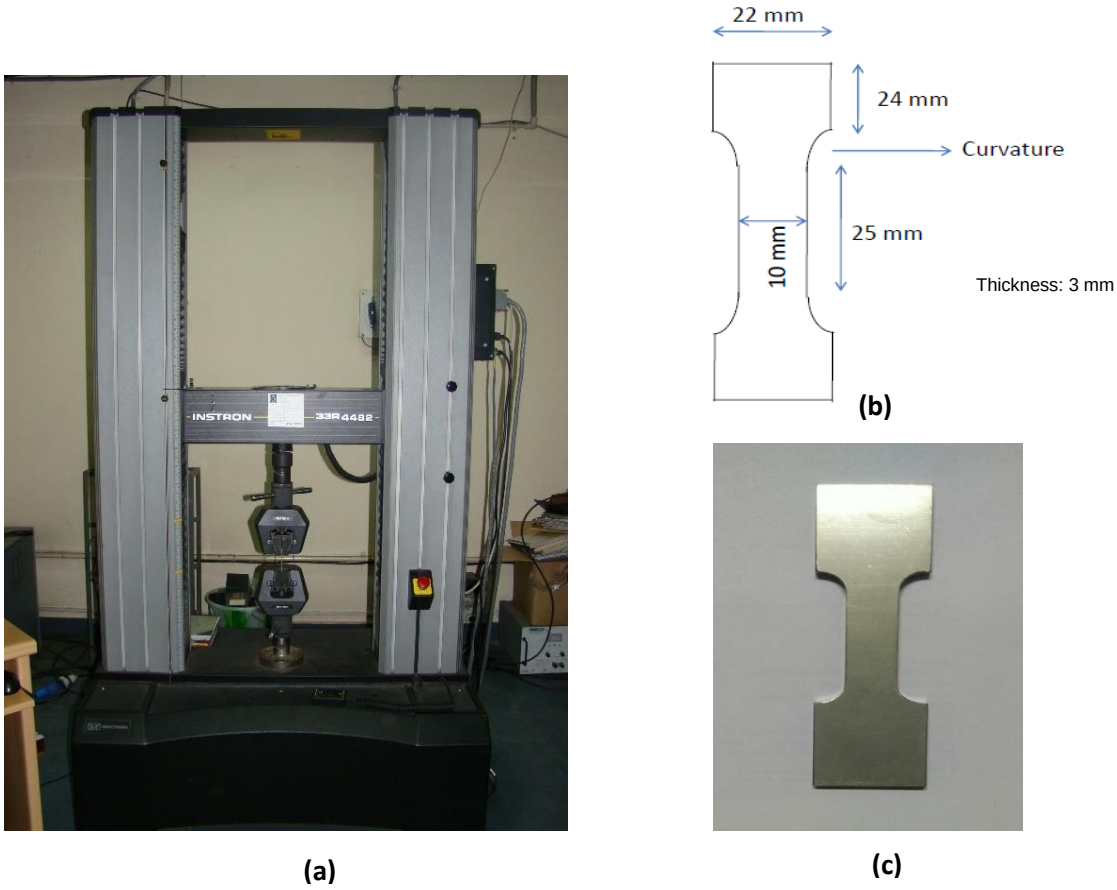

Fig. 2.5: (a) Universal tensile testing machine (b) Schematic representation of tensile sample along with dimensions & (c) Tensile sample specimen used in the experiment

Uniaxial tensile deformation was carried out on these samples for specific strain rates (explained in Chapter 4, section 4.4) by controlling the extension rate in the universal tensile testing machine. For further characterisation, square samples have been cut out from near the fracture region of the samples using the diamond wheel cutting machine with appropriate cooling to avoid any localized annealing due to heat. XRD study was performed on these square samples which were surface finished using the automated polishing machine (Fig. 2.1) to get good XRD pattern. The samples were electro polished using the Struers-make Lectopol-5 (Fig. 2.6) for further studies using FESEM-EBSD. Vibrating sample magnetometer (VSM) and Differential scanning calorimetry (DSC) measurements were

carried out on very small samples cut out from the fracture region again using the diamond wheel cutting machine.

Fig. 2.6: Electro polishing machine

The rolled copper sheets (20 cm x 15 cm) with different percentage of deformation were used for the deformation and annealing study detailed in chapter 5. The biaxial deformation was done at room temperature using a roller mill of diameter 16.5 cm at a speed of 20 rpm. Square samples (approximately 12 x 12 mm^2) were cut from the different rolled sheets using jewellery hacksaw. At the time of sample cutting, precautions were taken so that the sample temperature does not increase above room temperature in order to avoid thermal activation of the defects which could cause changes in the microstructure which is undesirable. The samples were mechanically polished sequentially using different grade (600, 800, 1000, 1200) silicon carbide (SiC) papers and finally polished to mirror finish using fine grain (9 μm, 3 μm, 1 μm and 0.25 μm) diamond paste to get proper XRD data.

In order to determine the temperature for the in-situ XRD studies, the initial experimental was carried out ex-situ using a silicone oil bath on a thermostat controlled magnetic stirrer (shown in Fig. 2.7). This ensured homogenous sample heating and

prevention of oxidation of the sample surface at elevated temperatures. The actual sample temperature was measured using a thermometer inserted into the oil bath.

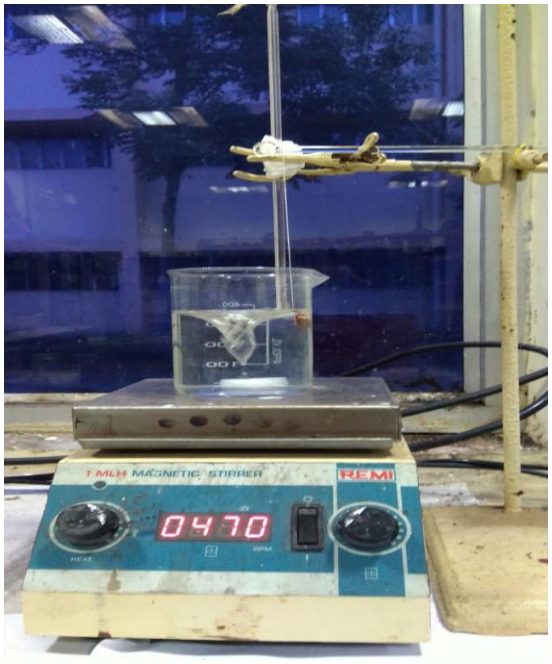

Fig. 2.7: Silicon oil bath heated by Magnetic Stirrer

Room temperature XRD measurements could be carried out on samples with varying thickness since the Bragg-Brentano (BB) geometry could be satisfied using a special sample mount. However, for the high temperature XRD measurements the sample has to be mounted on a Pt strip heater. If a thick sample is mounted on the strip heater, the extra height coming from the sample thickness changes the focusing condition of BB geometry. Thus, the use of thin sample is recommended during the recrystallization study. Here, each piece of the rolled samples were thinned down to <0.2 mm before mounting for the high temperature stage. Finally, the surface was electrochemically etched to get a good microstructure using Optical Microscope and FESEM.

2.3 X-ray Diffraction:

X-ray diffraction (XRD) is a popular technique for material characterisation used extensively in various scientific and industrial applications. It is a rapid analytical technique primarily

used to identify the crystalline phase and subsequently quantify the crystallographic parameters such as unit cell dimensions and atom position etc. Additionally, since this technique determines the three-dimensional array of lattice, any deviation of that array i.e. formation of the defects affect the XRD patterns and understanding the underlying reasons will help in identifying and quantifying the defects.

2.3.1 Details of the X-Ray Diffractometer:

All the data used in this thesis have been collected using the Bruker AXS D8 Advance Diffractometer. The front view of the diffractometer is shown in the Fig. 2.8. X-Ray Diffractometer has three main basic components: (i) X-ray generator tube, (ii) Sample holder and (iii) X-ray detector. Different sealed tube sources e.g. Cu, Co and Mo etc. for different wavelengths can be used in this diffractometer depending on the requirement. Soller slits are connected to the source tube for collimating the X-rays. Two type of sample stages are

Fig. 2.8: The front view of the X-ray diffractometer

available with the system; (i) conventional room temperature spinner stage for performing the room temperature XRD (Fig. 2.9) and (ii) high temperature sample stage (Fig. 2.10) which can be attached with this system to perform XRD at different temperatures up to 1500℃. In the high temperature stage, platinum strip acts as both the heater and the sample holder. The high temperature experiments were carried out in vacuum to prevent oxidation of the samples. The temperature of the platinum strip (stage temperature) and the sample temperature are measured using two different thermocouples. One is attached to the lower side of the platinum strip just below the sample position. The other can be positioned on the sample surface to measure the actual sample temperature to avoid any discrepancies in the measurement due to the thermal conductivity of the sample. During the measurement using the high temperature stage the samples were mounted on the platinum strip using a thin layer of silver paste which acted as the thermal contact between the strip and the sample.

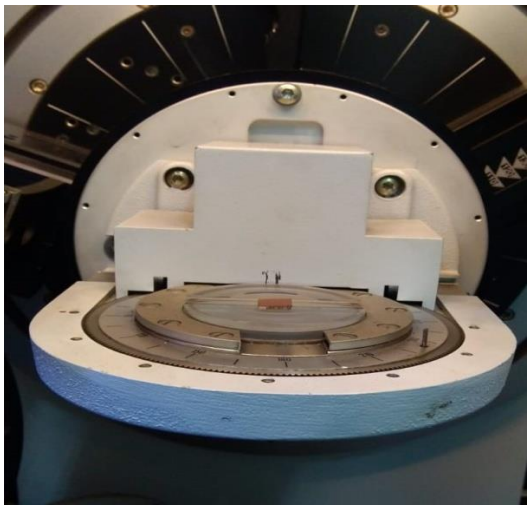

Fig. 2.9: Room temperature XRD spinner stage

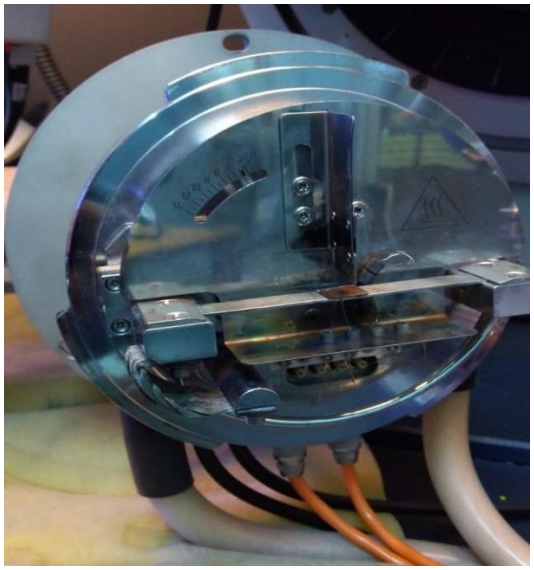

Fig. 2.10: High temperature XRD sample stage

The diffracted X-rays from the sample were collected using the Lynx-Eye^{TM} detector. This is a one-dimensional detector patented by Bruker AXS and is based on compound silicon strip technology. This detector provides an enormous advantage in terms of intensity, peak-to-background-ratio and lower limits of detection. It gives a high-count rate (increase in intensity per unit time) without sacrificing the resolution and peak profile. This detector is capable of recording approximately 200 times the intensity of ordinary point detector while maintaining same data quality. This is required for reliable and accurate microstructural analysis using the XRD line profile.

Diffractometers generally work under two geometries (i) "θ-2θ Bragg-Brentano geometry", where the source is fixed but the sample and the detector are moved as θ degs and 2θ degs respectively and (ii) "θ-θ Bragg-Brentano geometry", where the sample stage is fixed whereas both source and detector are moved by θ degs with respect to the sample. The Bruker AXS D8 Advance diffractometer used in this study has a θ-θ Bragg-Brentano geometry measurement system. It has advantage of dealing with any type of samples (e.g. any solid, liquid or powdered samples) as the sample stage is fixed. Details of the parameters used during the data collection for the different studies are discussed in the respective chapters.

2.3.2 Different model based techniques of XRDLPA:

Ideally, a sharp diffraction line (Dirac delta function) is expected due to scattering of X-rays from an infinite regular array of atoms. In reality, crystalline materials are never ideal and contain lattice defects which can cause broadening of the diffraction line [42]. The X-ray line is mainly broadened due to small size of the crystallites, dislocations, planar defects (twins and stacking faults), chemical inhomogeneity etc. More specifically, in a chemically homogenous material, fragmentation of the material into domains with different crystallographic orientations and the strain field of crystal lattice defects are the two major causes for the broadening of the X-ray line profile. The broadening caused by the fragmentation of material into some small coherent crystal is called "size broadening" and on the other hand the broadening due to lattice distortion of the individual defect strain field is called "strain broadening". During deformation or irradiation, a large number of different types of defects are produced which results in disturbance of the regular lattice. These defects can rearrange causing the formation of lower misorientation boundaries in the lattice which decreases the size of the coherent region from which the diffraction takes place thus causing the "size broadening" of the peak. On the other hand, the individual defects inside the coherent domains, will produce lattice strain which causes the "strain broadening" of the X-ray line profile. These two broadenings can be separated from the total line shape using the various X-ray Line profile analysis (XRDLPA) techniques. Thus XRDLPA will help to extract the different parameters related to size and strain broadening.

The peak broadening in the experimentally measured X-ray diffraction profile is mainly coming from the two parts (i) Instrumental broadening and (ii) Sample broadening. The instrumental broadening contribution is decided by the X-ray source, detector, the different collimators, etc., that are used in the experimental setup. This contribution is usually fixed for a particular set of hardware. The instrumental broadening parameters are calculated

from the data of a NIST standard sample (LaB_6 or Si-powder) collected under the same experimental conditions that were used for that the samples. The instrumental broadening is modelled using the Caglioti relations [43]–

$$FWHM^2 = U\ tan^2(\theta) + V\ tan(\theta) + W \qquad (\mathbf{2.1}\boldsymbol{a})$$

$$\eta = a + b\ (2\theta) \qquad (\mathbf{2.1b})$$

Where, U, V, W are the variables defining the Full Width at Half Maximum(FWHM)as a function of $tan(\theta)$ and ηrepresents the fraction of Gaussianity of pseudo-Voigt (pV) function defining in terms of variables a and b.These parameters are listed in Table 2.1 for the Cu and Co sources which were in this thesis.

Table 2.1: List of Caglioti parameters for Cu and Co source

Parameters	Cu-source	Co-source
U	1.4E-3±4.8E-4	1.7E-3±4.5E-5
V	-8.9E-4±1.8E-4	-1.6E-3±8.6E-6
W	2.9E-3±1.3E-4	3.9E-3±1.4E-4
a	0.41±0.01	0.43±0.01
b	5.2E-3±2.3E-4	5.2E-2±1.0E-3

Several ab-initio and model based approaches have been developed to calculate the microstructural parameters using XRDLPA and they have been successfully adopted to evaluate the microstructure of irradiated and deformed materials [5,13,51–56,42,44–50]. They can also be broadly categorized according to whether the analysis is carried out using individual peaks or using the whole XRD pattern. Each of the model-based technique has their own unique approach and use different mathematical functions to model the peak broadening. Using different methods thus help in characterising the microstructural

parameters to different levels of complexity. All the methods, which have been used throughout this study, are explained below.

Scherrer Equation:

Scherrer equation is used in XRD method to calculate the size of sub-micron crystallite from the broadening of the peak in a diffraction pattern [57]. This is approximated by considering that the peak broadening comes only from size factors. Strain contribution in the peak broadening does not consider here. The Scherrer equation can be written as [57]–

$$D_V = \frac{K\lambda}{\beta \cos(\theta)} \qquad (\mathbf{2.2})$$

Where, D_V is the mean coherent crystallite size (domain size), K is a dimensionless shape factor with a value of close to unity. In general it is considered as 0.9 but it depends on the actual shape of the crystallite. β is the total integral breadth, θis the Bragg angle and λ is the wavelength.

Williamson-Hall (WH) analysis:

This is a primary method to get an idea of the relative contribution of size and strain broadening in the XRD pattern and qualitative understanding of the strain anisotropy [9]. In this method, both these contributions are modelled using the Cauchy functions and hence the total integral breadth is the sum of the integral breadth of two Cauchy functions.

$$\beta_{total} = \beta_{size} + \beta_{strain} \qquad \mathbf{(2.3)}$$

According to the Uniform Deformation model for an elastically isotropic solid (No Strain anisotropy [58], the order independent volume weighted domain size (D_V) and order dependent microstrain (ε) is given by

$$(\beta \cos\theta/\lambda) = 0.9/D_V + 2\varepsilon((2\sin\theta)/\lambda) \qquad \mathbf{(2.4)}$$

Where, β is the total integral breadth, θ is the Bragg angle and λ is the wavelength. In case of elastically isotropic solid, WH plot (β* Vs d* plot, Where, β* =$(\beta \cos\theta/\lambda)$ and d* =

$(2\sin\theta)/\lambda)$ should be a straight line in which the intercept determines the coherent domain size and the slope of the straight line dictates the micro-strain inside the domain. Non linearity of the WH plot indicates the non-isotropic strain induced inside the domain. This analysis helps us to choose the model (Isotropic or non-isotropic) for further detail analysis.

Modified Williamson-Hall (MWH) technique:

In order to correct the strain anisotropy contribution to the peak broadening (inherently present in the material caused by the non-isotropic elastic properties) Ungár et al. [59] proposed a modified Williamson-Hall technique assuming that the strain broadening is caused only by dislocations. The strain anisotropy was introduced using a scaling factor C (dislocation contrast factor) [60], thus modifying the above eqn. to -

$$\frac{\beta cos\theta}{\lambda} = \frac{0.9}{D_V} + a\left(\frac{2\sin\theta}{\lambda}\right)\bar{C}^{\frac{1}{2}} + b\left(\frac{2\sin\theta}{\lambda}\right)^2 \bar{C} \qquad (\mathbf{2.5})$$

Where, a is related to the effective outer cut-off radius of the dislocation, Burgers vector, and dislocation density and b is related to corresponding fluctuations in the dislocation density. The average contrast factor $\bar{C}$ related to the elastic constants of the material and can be theoretically calculated using the program ANZIC [61].

The values of β used in both the above analysis are calculated using the program Winplotr [62] after including the instrumental broadening correction file. This file is also generated using the Winplotr program from the NIST standard sample data.

Double-Voigt technique:

In this technique, Voigt functions are used to separate the size and the strain broadening contribution in the XRD line profile [63]. The surface-weighted domain size (D_S), volume weighted domain size (D_v) and the root mean square microstrain$(<\varepsilon(L)^2>)^{\frac{1}{2}}$ can be calculated using this technique after appropriately modelling the peak profiles.

The Fourier transform of the Voigt function used to calculate the Fourier coefficients F(L) in terms of a distance L, perpendicular to the diffracting planes can be written as [63] -

$$F(L) = (-2L\,\beta_C - \pi L\beta_G^2) \quad \textbf{(2.6)}$$

Where, β_C and β_G are the Cauchy and Gauss components of the total integral breadth respectively. β_C and β_G can be written as -

$$\beta_C = \beta_{SC} + \beta_{DC} \quad \textbf{(2.7)}$$

$$\beta_G^2 = \beta_{SG}^2 + \beta_{DG}^2 \quad \textbf{(2.8)}$$

β_{SC} and β_{DC} are the Cauchy components of the size and strain contributions to the integral breadth respectively and β_{SG} and β_{DG} are the corresponding Gaussian components.

The size and the strain coefficients are obtained by considering at least two reflections from the same family of crystallographic planes. The area/surface and volume weighted domain sizes are respectively [63]-

$$D_S = \frac{1}{2\beta_{SC}} \quad \textbf{(2.9a)}$$

$$D_V = \frac{\exp(k^2)}{\beta_{SG}}(1 - \mathrm{erf}\,(k)) \quad \textbf{(2.9b)}$$

Where, $k = \frac{\beta_{SC}}{(\pi^{1/2}\beta_{SG})}$, the characteristic integral-breadth ratio of a Voigt function. Also, the mean square strain is expressed as function of the averaging distance *L* as -

$$< \varepsilon(L)^2 > = \frac{1}{S_0^2}\left(\frac{\beta_{DG}^2}{2\pi} + \frac{\beta_{DC}}{\pi^2}\frac{1}{L}\right), \quad \text{where } S_0 = 2\sin\theta / \lambda \quad \textbf{(2.10)}$$

The values of the micro-strain at averaging distance $L = D_s/2$ and at $D_v/2$ are usually considered for comparison of the results.

The values of β_C and β_G are calculated using the program Winplotr after including the instrumental broadening correction file. The program BREADTH by Balzer [63] is used for calculating the microstructural parameters.

Modified Rietveld method using MAUD:

Rietveld method is a time-tested analysis technique used for quantification of phases from XRD data [64]. This is a whole pattern fitting method where the contributions of all diffracted peaks in the observed XRD pattern are used for calculating the average microstructural parameters.

The XRD pattern has been represented in this method as a function of the diffraction angle (2θ) as [8,65–67] -

$$Y_C(2\theta) = [B * (I_S * I_a)](2\theta) + bkg \quad \textbf{(2.11)}$$

In the above, 'B' represents the true line broadening related to the sample. Also, the symmetric and asymmetric parts of the instrumental broadening function are represented by I_S and I_a respectively. Here 'B' and 'I_S' are modelled using a pseudo-Voigt (pV) function and they are convoluted first using the procedure described by de Keijser *et.al.* [10]. Then, 'I_a', represented by an exponential function [64] is numerically convoluted with earlier result. To get the final XRD pattern, the background 'bkg' is added to the convolution of 'B', 'I_S' and 'I_a'. The pV function can be written explicitly-

$$pV\ (2\theta) = \sum_{\alpha_1\alpha_2} I_{nt}\,[(1-\eta)(1+S^2)^{-1} + \eta \exp(-\ln 2 \times S^2)] \quad \textbf{(2.12)}$$

$$Where,\quad S = (2\theta - 2\theta_0)/HWHM$$

And, HWHM and η are considered as shape parameters in the above pV function. L. Lutterotti *et.al.*, introduced the contribution of the size and strain broadening in the Rietveld technique, by modifying the width and the mixing parameter of the pseudo-Voigt function which is used to model the diffraction line in this method and implemented it in the software MAUD (Materials Analysis Using Diffraction) [8,67,68] [Note: For the analysis of the XRD data in Chapter 5, the program LS1 (earlier version of MAUD) and MAUD have both been used. The publication arising from this chapter contains the results obtained using LS1 and hence the same has been shown in the thesis. A few of the other analysis (not included in the

publication) were carried out using MAUD at a later stage and have been included in Chapter 5. However, the results from both the analysis are consistent with each other and did not depend on the software used]. The relation of the coherent domain size (D), and the r.m.s. microstrain ($<\boldsymbol{\varepsilon}^2>^{1/2}$) (assuming a Gaussian strain distribution) with the pV function for the true line broadening are given below [8,67,68] -

$$Z/(Z+1)\exp[-(Z+1)^2/(16\ln 2)] + 1/(Z+1)\exp[-(Z+1)/2] = \exp\left[-\pi^2 < \varepsilon^2 > \frac{D^2}{(2d^2)} - 1/2\right] \quad \textbf{(2.13a)}$$

$$HWHM = \arcsin[\lambda\ (Z+1)/(4\pi D) + \sin\theta_0] - \theta \quad \textbf{(2.13b)}$$

$$\eta = Z/\left[Z + (\pi/\ln 2)^{1/2}\right] \quad \textbf{(2.13c)}$$

This modified Rietveld method is then used to fit the experimental data profile with D and $<\varepsilon^2>$, as fit parameters.

Preferred orientation, or texture in crystalline materials can cause serious systematic errors in fitting the XRD data during the evaluation of the crystallographic (lattice constants) and microstructural parameters. Among the various models available in the program MAUD for correcting the texture the most popular is the generalized spherical harmonic model [69]. While fitting, the harmonic expansion parameter is gradually increased till the required results are obtained. The size and strain anisotropy in the MAUD program is treated using the POPA anisotropy model. In this model, the direction dependent domain size is given by [70,71] -

$$< R_h > = R_0 + R_1 P_2^0(x) + R_2 P_2^1(x)\cos\phi + R_3 P_2^1(x)\sin\phi + R_4 P_2^2(x)\cos 2\phi + R_5 P_2^2(x)\sin 2\phi \quad \textbf{(2.14)}$$

Where, x and φ have a relation with the miller indices (hkl) of the different crystallographic planes. Also the dependence of the micro strain with (hkl) for the material with cubic symmetry is given by [70] -

$$< \varepsilon_{hh}^2 > E_H^4 = E_1(h^4 + k^4 + l^4) + 2E_2(h^2k^2 + k^2l^2 + h^2l^2) \quad \textbf{(2.15)}$$

Where, $E_H = aH$, with 'a' is the lattice parameter and $H = 2sin\theta / \lambda$.

The calculation of the instrumental broadening parameters (which determine the contribution of instrumental broadening) is carried out using MAUD from NIST standard LaB_6data collected with the same experimental parameters. Then the sample XRD data is first fitted by considering the instrumental parameter files, background of the XRD profile and the crystallographic parameters (e.g. lattice parameters, crystallographic structure etc.). The crystal structure information for the particular sample is introduced into the program as the CIF file (Crystallographic Information file) which is available online. In the next step, the microstructural parameters are also refinement (crystallite size (D_S) and r.m.s. microstrain $<\varepsilon_L^2>^{1/2}$) sequentially by first considering the isotropic DELFT model and then refining the texture parameters and finally the anisotropy parameters [10,67,72].

Convolutional Multiple Whole Profile fitting (CMWP):

In this method, ab-initio theoretical functions are used for size and strain broadening to fit the diffraction profile [44]. The Fourier coefficients of size and strain profiles are expressed in terms of refining parameters. All the Fourier coefficients along with the instrumental contributions are multiplied and then inverse Fourier transformed to match with the observed profile [44]. For the determination of size Fourier coefficient, it is assumed that the crystallites are spherical in shape and has a log-normal size distribution [44]. The refining parameters for obtaining the size profile are the median and variance of the distribution. One

can obtain size distribution and also the average value of surface and volume weighted domain sizes from the refined values of these parameters [44].

On the other hand, the strain broadening contribution is assumed to arise from dislocations only. Hence, the strain Fourier coefficients are expressed as a function of dislocation density (ρ), average contrast factor of dislocation $(\overline{C})$ and arrangement of dislocation $f(R_e^*)$ in matrix [5,44,73–75]

$$A_D(L) = exp\left[-2\pi^2 g^2 L^2 \left(\frac{b}{2\pi}\right)^2 \pi\rho\overline{C} f\left(\frac{L}{R_e^*}\right)\right] \quad \textbf{(2.16)}$$

Here, L is the coherent length and R_e^* is the outer cut-off radius of dislocation where strain field diminish to zero. The average contrast factor of dislocation $(\overline{C})$ defines the relative orientation of burger vector (b) with respect to the diffraction vector (g). It depends on the elastic properties of the material. For cubic materials, it can be calculated using the following equation [44,60]

$$\bar{C}_{hkl} = \bar{C}_{h00}(1 - qH^2) \quad \textbf{(2.17)}$$

Where, H^2 can be expressed as a function of diffracting plane {hkl}. The theoretical value of average contrast factor for $\{h00\}$ reflection $(\bar{C}_{h00})$ and q which defines type of dislocation can be calculated using $\bar{C}_{hkl}$ values obtained from the online programme ANIZC [61]. Depending on the elastic constants and the type of dislocation (pure screw and edge dislocation) the program calculates the $\overline{C}_{hkl}$. The experimental value of 'q' is then compared with the theoretically obtained one to know the type of dislocations present in the system. Another parameter called Wilkens arrangement parameter was introduced by Wilkens for describing the arrangement of dislocation in the matrix using R_e^* [44,61,73]

$$M^* = R_e^* * \sqrt{\rho} \quad \textbf{(2.18)}$$

The large value of M* indicates random arrangement of dislocation whereas small value indicates that the dislocations are arranged to screen their strain field [44].

2.4 Universal testing machine (UTM):

The uniaxial deformation of SS304 samples for carrying out the study of austenite to martensite phase transformation has been performed using the universal tensile testing machine INSTRON (Model: 4482) at room temperature shown in the Fig. 2.5. The sample is mounted between the fixed and the movable arms of the instrument. The system is fully computerised and servo controlled. The control parameter is the extension rate (mm/sec) which controls the movement of the upper (movable) arm. The load on the sample is measured by the load cell which is mounded on the movable arm. The details specification of the universal tensile testing machine is given in the Table 2.2 In the system, one can control the extension rate and that is related to the strain rate through the gauge length of the tensile sample. Thus, one has to choose the extension rate for your specific sample such that it can satisfy the required strain rate. To end the experiment at a specific strain value (pre-strain value used in the case of the SS304 study), the option "End criteria", available in the software was used. The specific extension value corresponding to the required strain value was input as the parameter (which depended on the gauge length of the sample from which the strain could be calculated).

Table 2.2: Parameters of the UTM

Parameters	Specification	Parameters	Specification
Load capacity	100 kN	Return speed	600 mm/min
Maximum speed	500 mm/min	Position control resolution	0.006 mm
Minimum speed	0.001 mm/min	Crosshead speed Accuracy	±0.10 mm or 0.15% of displacement
Maximum force at full speed	75 kN	Load measurement	±0.5% of reading down to 1/50 of load cell capacity
Maximum speed at full force	250 mm/min	Strain measurement	±0.5% of reading down to 1/50 of full

		Accuracy	range
Position measurement accuracy	±0.10 mm or 0.15%	Position control resolution	0.006 mm

2.5 Vibrating sample magnetometer (VSM):

Quantification of martensite is very important in the austenite to martensite phase transition study. Austenite phase is non-magnetic whereas the martensite phase is magnetic. Thus the

Fig. 2.11: Vibrating sample magnetometer (VSM)

magnetic study can be used to quantify the martensitic phase. In our study, VSM (Shown in Fig. 2.11) was used to measure the saturation magnetic moment of the samples. When a magnetic material is situated in an external magnetic field, magnetic dipole moments of the sample are aligned in the direction of the external field. The measure of the moment in the sample gives an indication of the magnetic susceptibility of the material. In the VSM, the induced magnetic moment is measured using a stationary pick-up coil. When the sample is vibrated inside the coil, the emf induced (in the coil) is a direct measure of the magnetic

moment of the sample. Thus, measuring this emf at the same frequency as the sample vibration using a lock-in amplifier gives the magnetic moment which is then converted in terms of emu/gm using a calibration standard.

The experiment has been carried out at room temperature, only to quantify the amount of magnetic phase in the deformed SS304. Quantification has been done by measuring the magnetic hysteresis loop up to 3 Tesla over the full cycle (0T to 3T to 0T to –3T to 0T). The saturation magnetisation and the coercivity of the samples were evaluated from the hysteresis loops obtained.

2.8 Differential Scanning Calorimetry (DSC):

DSC allows the measurement of reaction heats and heats of transitions, heat flow rates and their changes. In both the deformation study carried out in this thesis, DSC measurements were used to supplement the XRD measurements. DSC measurements were carried out in the Netzsch-make Simultaneous Thermal Analyser 449-F1 shown in the Fig. 2.12. In this technique, the sample and the reference pans are heated at the same rate by an external

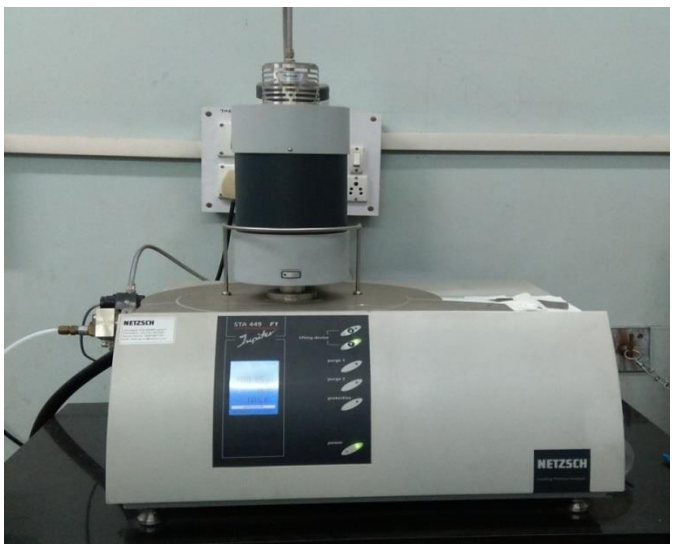

Fig. 2.12: Simultaneous Thermal Analyser

furnace. The temperature difference between the two pans is monitored using a differential thermocouple connected to the bottom of the pans. The lead or lag of the temperature of the

sample pan over that of the reference pan is then measured as a function of the heating rate. This temperature difference is calibrated in terms of the heat flow to/from sample giving indication of the endothermic/exothermic process the sample is undergoing a thermodynamic process. This is a sensitive method for evaluating the stored energy in the deformed materials and also to any heat absorbed during phase transition. The DSC scans can be performed upto 1200 ℃ using either Pt, Pt-lined alumina or Alumina crucibles. If the thermograms have to be measured below 600 ℃, then Aluminum crucibles are the best choice due to their improved thermal conductivity.

2.9 Optical microscopy:

Optical microscope uses visible light as the probing tool and a system of lenses to magnify the object size. Present day optical microscopes have complex designs to improve the resolution and contrast of the optical images. For our study of metallic surfaces, we have used the inverted optical microscope of Carl Zeiss make (shown in Fig. 2.13). Due to its versatile nature the applicability of the microscope has been extended to various materials science applications including grain sizing, inclusion counts, layer thickness assessment, phase determination etc. The illuminating system consists of a light source, condenser lenses/filters/polarisers, an aperture diaphragm (for controlling the amount of light entering

Fig. 2.13: Carl Zeiss make inverted Optical microscope

the objective lens), and a plane glass reflector. The objective lenses are of varying magnification (5x, 10x, 20x, 40x) are available along with the eyepiece of 10x magnification. The images can be captured using a CCD camera attached to the side port in the microscope. In our study the optical micrographs have been used as the first technique to understand the microstructure of the samples during different stages of the studies. Proper sample preparation using grinding, polishing and surface etching/electropolishing was done according to the sample before capturing the micrographs.

2.10 Field Emission Scanning Electron Microscope based Electron back scatters diffraction (FESEM- EBSD):

Scanning electron microscopy (SEM) provides topographical and elemental information at useful magnifications of 10x to 1,00,000 x, with virtually unlimited depth of field. This instrument uses a finely focused electron beam which is scanned across the surface of the sample. The resulting secondary electrons, backscattered electrons, and characteristic X-rays are collected by detectors and displayed real time on a CRT screen. Topographical images of the sample are generated using the secondary electrons. Backscattered electron imaging gives the elemental contrast within the top few layers of sample (usually < 150 nm) and can be used for mapping the spatial distribution of elements or compounds. Recent developments on improving the electron source to Field Emission Guns (which can provide narrower electron beams) have enabled the visualization of the images at an ultra-high magnification (up to 3,00,000x) and higher resolution (~ 1.5 nm) than the conventional SEM.

For our study we have used the Carl Zeiss-make SUPRA 55 FESEM (shown in Fig. 2.14). It is equipped with a patented GEMINI^{TM} column which is designed to provide superior beam brightness with ultrahigh resolution for the entire voltage range together with high probe currents for analytical applications. It has an internal beam booster which maintains a high beam energy throughout the entire column, regardless of the electron beam

Fig. 2.14: Front view of Field Emission Scanning Electron Microscope (FESEM)

energy selected by the operator. The beam is decelerated to the selected energy only after passing through the scanning system. The electron beam path is also designed to eliminate crossover of beam electrons between source and specimen. It is equipped with both the in-lens secondary electron detector (located within the column), an independent Everhart-Thornley secondary electron detector and 4-Duadrant solid state back scattered electron detector. Additional detectors for EDX (Oxford Liquid Nitrogen free SDD X MAX 20) and WDX (INCA WAVE 500 wavelength dispersive spectrometer) measurements are also available with the instrument. The features of the SUPRA-55 are listed in Table 2.3

Table 2.3: Features of the SUPRA-55

Parameters	**Specification**	**Parameters**	**Specification**
Resolution	1.0 nm at 15 kV, 1.7 nm at 1 kV, 4.0 nm @ 0.1 kV	Standard detectors	High efficiency In-lens detector, Everhart-Thornley Secondary Electron Detector
Gun Vacuum	$\leq 1x10^{-10}$ mbar	Chamber	330 mm (Ø) x 270 mm (h), 2 EDS ports, CCD-camera with IR illumination, free ports

Magnification	12-900,000 x	Specimen stage	5-Axes Motorised Eucentric Specimen Stage
Emitter	Thermal field emission type	Image processing	Resolution: Up to 3072 x 2304 pixel, Noise reduction: Seven integration and averaging modes
Acceleration Voltage	0.1-30 kV	Image display	Single 19" TFT monitor with SEM image displayed at 1024 x 768 pixel
Probe Current	4 pA-10 nA	System Control	SmartSEM™ with Windows®XP, operated by mouse, keyboard and joystick with optional control panel

One of the main advantages of the focused electron beam available with the FESEM is that it can be used for collecting the crystallographic micro texture data from the sample surface using the Electron back scatter diffraction (EBSD) technique. The measurements are carried out using the Oxford Integrated Advanced Aztec HKL EBSD with fore scatter detector system with 4 diodes for Nordlys II Analysis. The sample is mounted on a 70 deg pre-tilted holder. The experiments are carried out on electro-polished surfaces of the samples.

Chapter 3

Depth profiling of ion induced damage in D9 alloy using X-ray Diffraction

3.1 Introduction:

Radiation damage of structural materials is of foremost importance and also a limiting issue for many applications including nuclear power production, medical applications, or components for scientific radiation sources. The lifetime of a component is largely restricted by the damage a material can sustain in the extreme environments of radiation, temperature, stress, and fatigue, over long periods of time. Since the beginning of the nuclear reactor era, the damage properties of a variety of materials have been widely studied in nuclear reactors and spallation neutron sources [2,34]. However, ion beam irradiations using particle accelerators are a more lucrative alternative to study radiation damage in materials in a rather short period of time [2,76,77] due to its fast cycle length and low cost. Extensive studies have been carried out on nuclear structural materials using ion beams to emulate the damage caused by neutron in the reactor [2,34]. Easy availability of ion sources, controllable irradiation conditions (dose, dose rate and temperature of irradiation), and low radioactivity of materials makes ion irradiation studies a rapid means for screening of materials and also for understanding various basic radiation damage processes [2]. However, the damage created by an energetic ion, is limited only to a certain depth depending on the energy and momentum of the incident ion unlike neutron where the penetration depth is several orders more than that of the ion with same energy. The incident ion loses its energy by both

electronic and nuclear losses thus coming to rest within the material at a certain projected range [2]. At the end of the trajectory, the nuclear energy loss becomes high and hence the damage distribution normally peaks at this region(called as Bragg peak after William Henry Bragg who discovered it in 1903) [78].

Thus, the ion irradiation results in a non-uniform damage profile as a function of depth. This is represented in Fig. 3.1(a), which shows the plot of target displacement in D9 alloy by a 35 MeV Helium ion. It is clear from the plot that up to nearly 2/3 of the range of the ion, the target displacements are almost constant and hence can be referred to as homogenous damage region. Near the peak damage region (Bragg peak) the target displacements vary significantly and hence this region can be referred as the inhomogeneous damage region. It has been a general practice among researchers to use the Monte Carlo simulation code (SRIM) [79] for understanding the ion energy deposition profile in a material and subsequently to calculate the damage profile for a given incident ion. The damage profile in SRIM is calculated assuming that for each incident ion the target is a perfect (but amorphous) material. It does not consider any pre-existing defects or the damages already created by the previous ion [79]. Hence at the end of the calculation (typically carried out for one lakh incident ions), one obtains a statistically averaged damage profile as a function of depth for a single incident ion. Moreover, SRIM does not take into account the diffusion of the freely-migrating point defects that are formed during the displacement cascade. The time scale of diffusion of these freely migrating defects is $>10^{-8}$ sec and can continue to time as high as10^{6} sec [2]. This migration is mainly aided by the new pathways that have been created for the diffusion of the vacancies and the interstitials by irradiation [80]. This increased diffusion phenomenon is known as Radiation Enhanced Diffusion (RED) [2]. As already discussed in Chapter 1, these defects agglomerate and cause a change in the microstructure of the material which dictates the properties. Due to the phenomenon of RED,

the microstructure near the peak damage region and also away from this peak along the depth (towards the homogeneous damage region) will not be as expected from the damage profile obtained from SRIM [Fig. 3.1(a)]. So, it is interesting to study the microstructural parameters along the depth of the sample from the peak damage region to the homogeneous region.

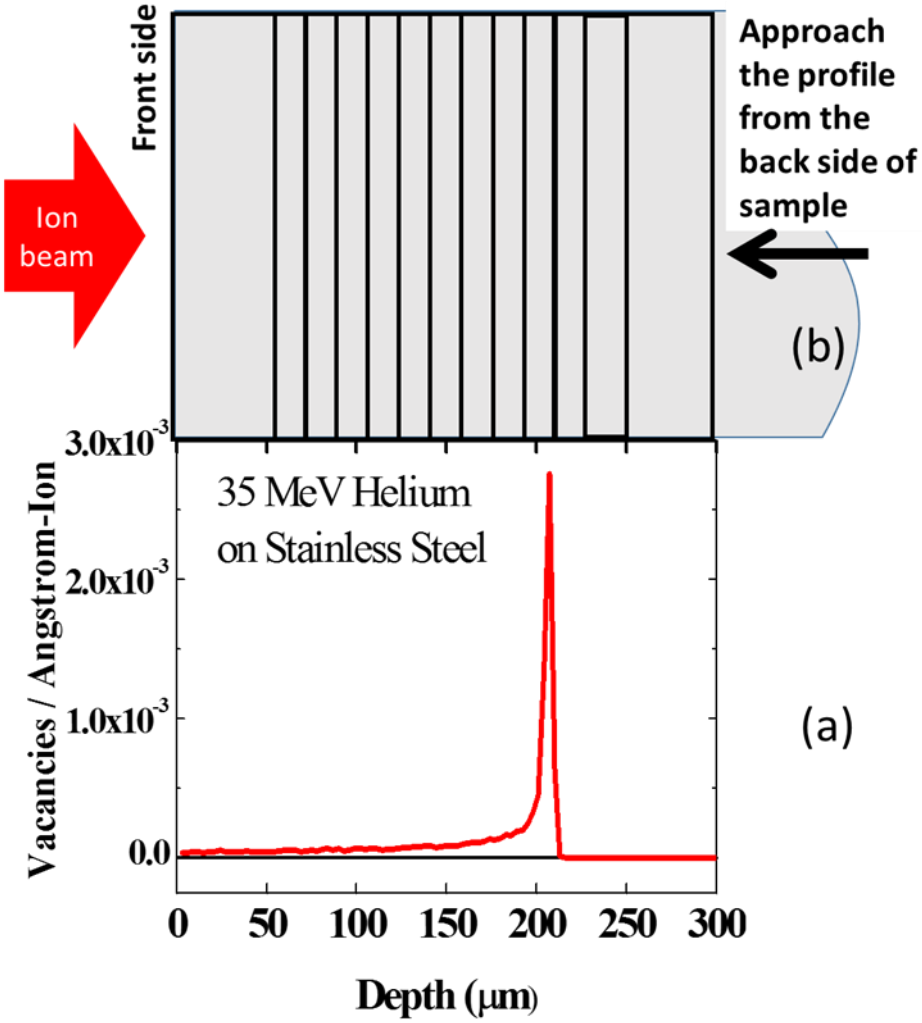

Fig. 3.1: Schematic diagram of the depth profiling of the sample where the bottom panel (a) shows the Damage profile obtained from the SRIM code and top panel (b) shows the methodology followed for accessing the damage profile.

3.2 Previous studies and motivation:

Several experimental studies were carried out to evaluate the damage profile along the depth in irradiated materials [81–86]. Whitley *et.al.* used cross sectional Transmission Electron Microscopy to evaluate the void-swelling in Ni after self-ion and Cu ion irradiation [87].

They found out that the swelling was higher in the middle of the ion range and decreasing significantly at near the end-of the range. They also observed that in the case of the Cu ion irradiation, the ions were confined to the end of its trajectory [87]. Shiraishi and Fukai carried out depth dependent damage profile study on 24 MeV He ion irradiated Stainless steel using micro-Vickers hardness measurement and cross sectional TEM [88]. They observed that the hardness values showed a peak at the end of the ion range [88]. Se-Hwan Chi *et.al.* measured the Vickers hardness as a function of depth to evaluate the depth profile in 12 MeV proton irradiated 12Cr-1Mo-V steel [89]. They found out that the peak damage region was shifted towards a lower depth, which they attributed to either work hardening during the sample preparation for hardness measurement or due to the thermal effects during the irradiation. Xu Wang *et.al.* had used micro Raman spectroscopy to evaluate the depth profile in 20MeV C ion irradiated SiC samples [90]. They had quantified the damage using the intensity and the area of the characteristic Raman modes of the SiC sample as a function of depth. They had also reported that the peak damage region was shifted from that calculated using SRIM and had attributed the shift to the stopping power values used in the calculation. An interesting observation reported by them was the non-linear increase in the damage as a function of dpa at a particular depth (Fig. 4 of [90]). Gigax*et.al.* had used cross-sectional TEM to study the radiation response of 3.5 MeV Fe ion irradiation on T91 alloy up to damage levels of 1000 dpa [86]. They exploited the variable damage along the depth to study the void swelling and precipitation in this alloy. All the previous studies showed inhomogeneous radiation damage along the penetration depth of incident ions. However, in order to understand the various phenomena revealed in the material due to ion irradiation it is crucial to systematically study the radiation induced microstructural changes as a function of depth on a few samples with different doses. It is important that while evaluating the material property as a function of depth sample preparation is carried out carefully so that the methods used do not introduce

unwanted errors in the experimental results. Undertaking a study on samples with different doses will also help to overcome this problem.

3.3. Brief description of work:

In this study, we have used X-ray diffraction line profile analysis (XRDLPA) for evaluating the microstructural parameters (such as coherent domain size and the microstrain within the domain) of an irradiated material as a function of ion penetration depth and at three different doses. The effect of irradiation on changing the microstructure of the material has already been discussed in detail in Chapter 1. In brief, irradiation induced defects (defect clusters, dislocation loops, new phases, precipitates etc.) disturb the periodicity of the crystal lattice. This causes a broadening of the X-ray peak thus giving the opportunity to indirectly evaluate the effect of irradiation on changing the microstructure as a function of depth and dose. This study has been carried out using alloy D9 (Ti-modified stainless steel) irradiated using 35 MeV α beam from the variable energy cyclotron at VECC, Kolkata. Alloy D9 gained importance as a structural material for Na-cooled fast breeder reactors [91]. The material showed a very good combination of high temperature tensile and creep strength properties, irradiation creep resistance and resistance to irradiation induced void swelling [36,37,91]. The percentage of minor alloying elements in this material have been specifically tuned to form precipitates (such as TiC etc.) which act as trapping centres for the point defects (especially vacancies) produced during irradiation. This prevents agglomeration of vacancies to create voids thus suppressing the phenomena of void swelling. The introduction of various other minor alloying elements such as Si and P in this alloy also helped in delaying the onset of void-swelling with irradiation dose [92]. Due to the importance of this alloy (or its variant) as a clad material in the Prototype Fast Breeder Reactor, it was chosen as material to carry out the study of damage depth profile in irradiated materials.

3.4 Experimental and characterisation details:

3.4.1 Sample description and preparation:

The alloy D9 used in this study has a nominal composition (in wt%) [91] as given in Table 3.1. The details of the samples and the irradiation were outlined in section 2.2.1, Chapter 2. The irradiation was carried out using a defocused beam of Helium ions of 35 MeV energy and a beam current of about 100 nA. The sample temperature was always below 313K during irradiation as measured by the thermocouple connected very close to the sample. Three samples were irradiated to final doses of 5×10^{15} He^{+2}/cm^2, 6.4×10^{16} He^{+2}/cm^2 and 2×10^{17} He^{+2}/cm^2 (a variation of about 3 orders).

Table 3.1: Chemical composition (in wt %) of Alloy D9

C	Mn	Ni	Cr	Mo	N	Ti	S	P	Fe
0.05	1.50	15.04	15.09	2.26	0.006	0.21	0.003	0.01	Rest

The depth-wise study has been performed by systematically removing the material from one side of the sample using a polishing machine. The details of the sample preparation have been described below in section 3.4.3.

3.4.2 Stopping and Range of Ions in Matter (SRIM):

Monte-Carlo simulation code SRIM 2013 [79] has been used for calculating the ion range and the damage profile of the 35 MeV alpha particles in alloy D9 and the result shown in Fig. 3.1(a). It can be seen that the maximum damage (Bragg peak) occurs at the depth of around 203 μm +/- 3 μm. Henceforth, the sample side facing the ion beam will be called the front face of the sample and the sample beyond the Bragg peak will be called the back face of the sample.

3.4.3 X-ray diffraction measurement:

Initially, the front side XRD data was collected from all the samples including one unirradiated sample. The depth-wise information of the microstructure was collected by systematically removing the material from the back of the sample. At each step as described below, the sample thickness was reduced by the automated polishing machine using a fine polishing cloth and distilled water. Initially, the thickness of the sample was 1mm which was reduced to about 300 μm from the back side. Subsequently, the thickness was reduced to 250 μm, 220 μm, and then brought down to 60 μm by removing material in each step by 20 +/- 2 μm. The lower depth limit was restricted to 60 μm due to the problem of handling (lower thickness) samples during further characterisation. The X-ray data was collected from the back surface of the sample at each step. Fig. 3.1(b) shows the experimental scheme used to carry out the study on the irradiated samples. All diffraction profiles were obtained using Co-Kα X-ray source in the range of 2θ from 45^0 to 124^0 with a step of 0.02^0. For calculating the instrumental broadening, standard LaB_6 powder sample was used and X-ray data was collected using the same experimental parameters.

3.4.4 X-ray Diffraction Line profile analysis (XRDLPA):

In this study, two main techniques have been used for extracting the microstructural parameters as a function of ion penetration depth in the He ion irradiated D9 sample. Among the various ab-initio and model-based approaches of XRDLPA for extracting the microstructure related parameters described in Chapter 2, (i) Double-Voigt technique [63] using diffraction peaks from two parallel set of planes and the (ii) whole pattern fitting technique using modified Rietveld method (with the program MAUD) [11,93] have been used in this study.

3.4.5 Optical microscopy:

During the experiments, it was observed that the XRD peaks of the unirradiated sample were broader compared to the irradiated sample. This is possible only if there are pre-existing defects in the unirradiated sample. In order to understand this, the unirradiated sample was annealed and the optical micrographs of unirradiated and annealed samples were obtained using a Carl Zeiss inverted optical microscope. The samples were mechanically polished followed by chemically polishing using 10% perchloric acid solution and then chemically etched using 10% oxalic acid solution to reveal the microstructure.

3.5 Results and Discussion:

Fig. 3.2 shows the X-ray diffraction pattern obtained from the unirradiated sample and those taken from the front side of the irradiated samples. At the initial dose of irradiation i.e. at a

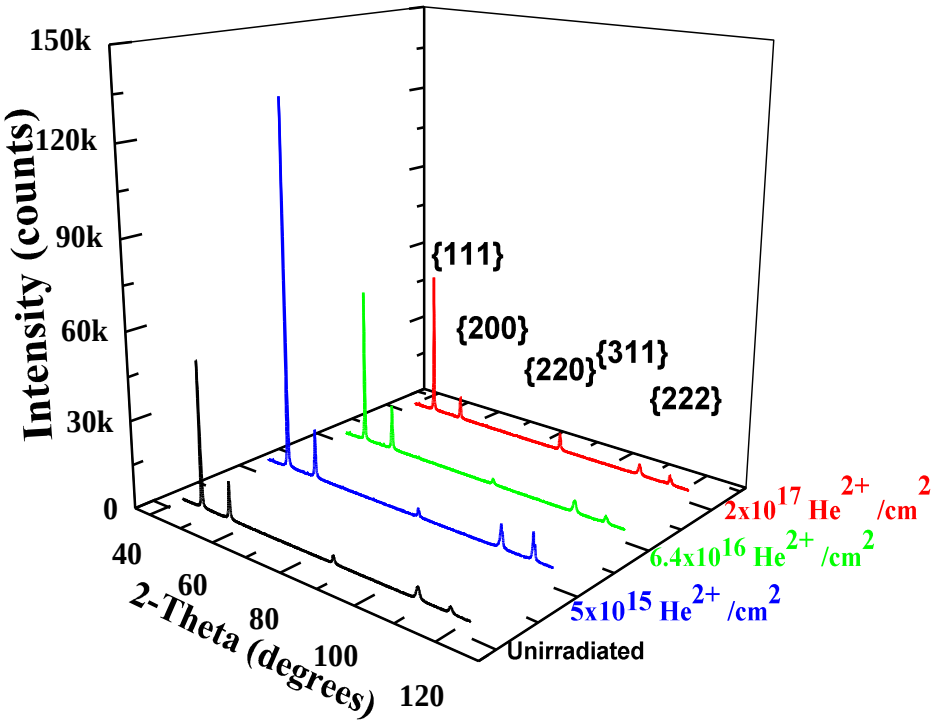

Fig. 3.2: X-ray diffraction pattern of the unirradiated and the three irradiated samples.

dose of $5x10^{15}$ He^{2+}/cm^2, we can see that there is an increase in the peak intensities accompanied by a decrease in the peak broadening. With increasing dose, the peak intensity is found to decrease with an increase in peak broadening.

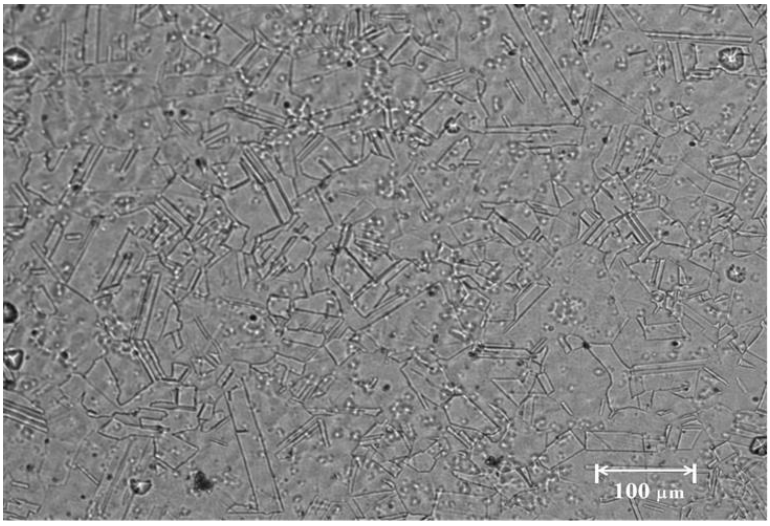

Fig. 3.3: Optical micrograph of the unirradiated sample.

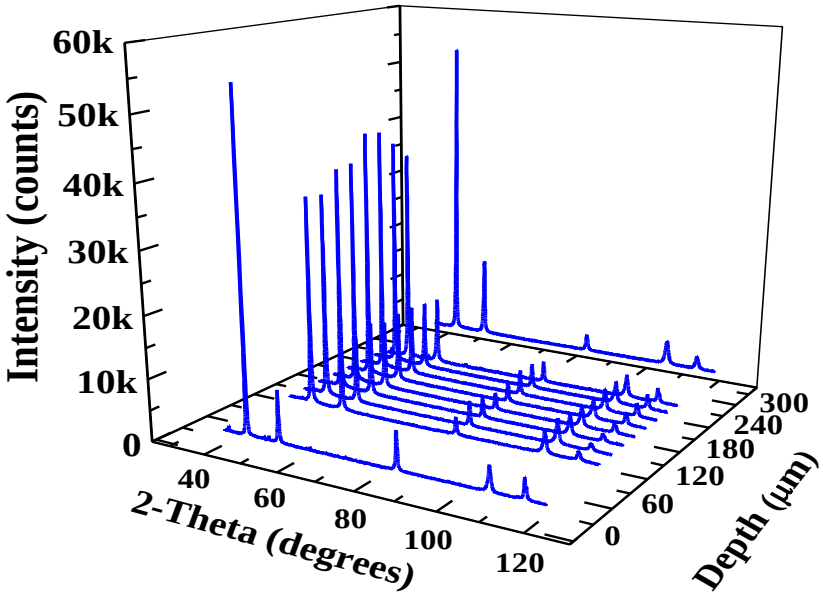

Fig. 3.4: X-ray diffraction pattern as a function of depth for the D9 sample irradiated to the dose of 2x1017 He2+/cm2.

Fig. 3.3 shows the optical micrograph of the unirradiated sample. One can see that the grain boundaries are not clearly visible and the grains show the presence of twins. This microstructure is typical of a solution annealed and rapidly quenched material. Fig. 3.4 shows

the X-ray patterns obtained from the highest dose ($2x10^{17}$ He^{2+}/cm^2) sample as a function of depth. Except for the data from the front face, 250 μm and 300 μm where the X-ray peak intensities are higher, the X-ray data from 60 μm to 220 μm show lower peak intensities and there is no significant change among them as a function of depth.

In the data taken at 250 μm and the 300 μm depth, it can be seen that these are more or less similar to the data of the unirradiated sample shown in Fig. 3.2. This shows that the sample at these depths is not affected by the irradiation. To extract the exact nature of the microstructural evolution, XRDLPA was carried out using the double Voigt technique and the Modified Rietveld method using MAUD. The volume weighted domain size and the r.m.s. microstrain (at $D_v/2$) of the unirradiated sample from the double Voigt analysis was found to be 574 ± 46 Å and $1.1x10^{-3}$ ± $1x10^{-4}$ respectively. Fig. 3.5 shows the variation of the

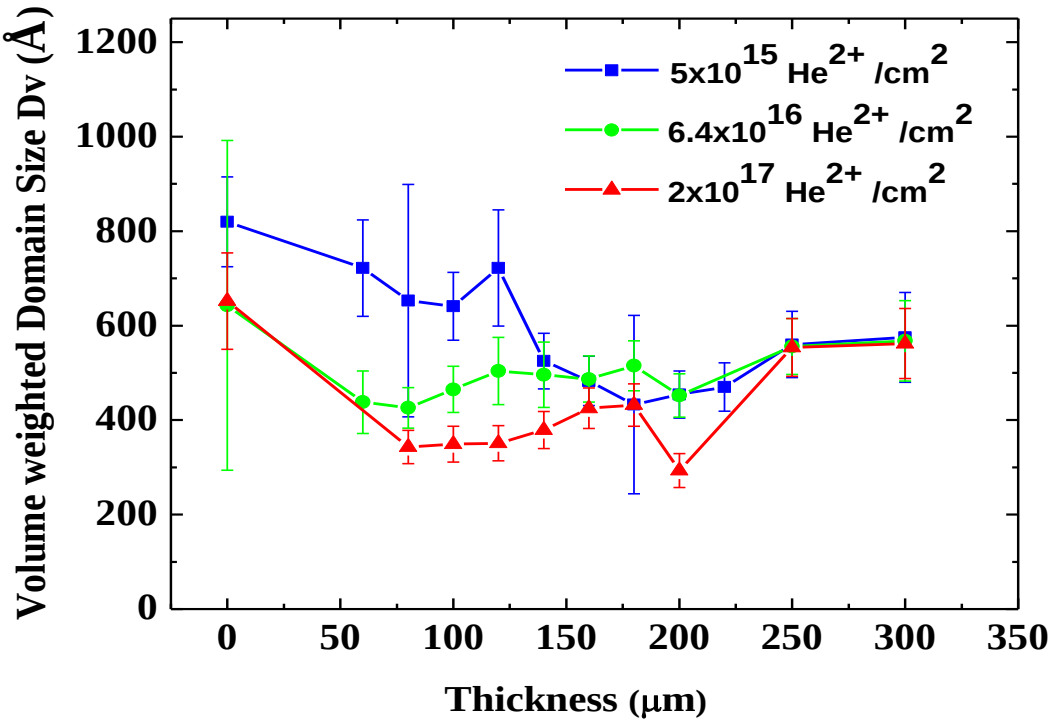

Fig. 3.5: Volume weighted domain size as a function of depth of three irradiated samples obtained from the Double Voigt analysis

volume weighted domain size obtained as a function of depth for the three irradiated samples using the double Voigt technique.

The following are the significant observations that can be inferred from Fig. 3.5:-

(a) In all the irradiated samples, the value of the domain sizes obtained in the front side of the sample is larger than that of the unirradiated region.

(b) The domain size of all the samples at 250 μm and 300 μm matches well with that of the unirradiated sample.

(c) In the lowest dose sample i.e., $5x10^{15}$ He^{2+}/cm^2, the domain size shows an increase compared to the unirradiated value at lower depths of up to 150 μm. Beyond 150 μm and up to the peak damage region, the value is lower than that of the unirradiated region.

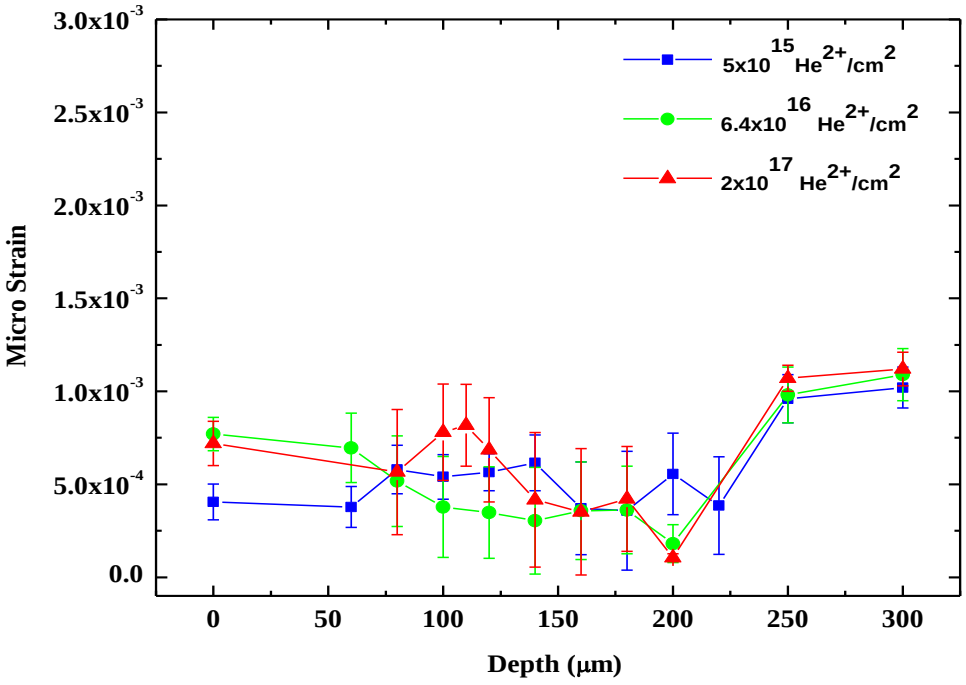

Fig. 3.6: Root mean square (r.m.s.) microstrain at Dv/2 as a function of depth of three irradiated samples obtained from the double Voigt analysis.

(d) In the other two doses of irradiation (6.4×10^{16} He^{+2}/cm^2 and 2×10^{17} He^{+2}/cm^2), the domain size is lower at all depths (except the front face, 250 μm and 300 μm) than that in the unirradiated region.

(e) The highest dose sample (2×10^{17} He^{+2}/cm^2) has a lower domain size than the 6.4×10^{16} He^{+2}/cm^2 sample at all depths except at 250 μm and 300 μm where the value almost coincides with the unirradiated region value.

Fig. 3.6 shows the r.m.s. microstrain obtained as a function of depth using the double Voigt technique for all the three irradiated samples. It can be seen that the r.m.s. microstrain are lower than the value at the unirradiated region ($\sim1x10^{-3}$) at all depths and does not show any systematic change as a function of depth contrary to the variation of the domain size (Fig. 3.5). The microstrain values are varying between $1x10^{-4}$ to $8x10^{-4}$ for all the three samples. The double Voigt analysis technique has been carried out only on the family of parallel set of planes i.e., the (111) and (222). But, it is well known that the defect diffusion and annihilation are inherently anisotropic in irradiated materials [94]. During irradiation, the production of the point defects depends on the displacement energy of the lattice atom. This energy depends on the potential barrier surrounding the equilibrium lattice atom and is thus not uniform in all directions. This causes a variation in the number of point defects produced along the different directions. In addition, the diffusion of the surviving point defects is determined by the easily available diffusion pathways. In general, the diffusion of the defects is controlled by the atomic density in a particular plane and hence is crystallographic plane dependent. Apart from this, the radiation enhanced diffusion also plays a significant role thus resulting a different microstructure along different crystallographic planes. In order to understand the defect migration and evolution in a comprehensive manner, the whole pattern fitting technique of modified Rietveld analysis has been carried out on all the samples as a function of depth.

Fig. 3.7 shows a typical graph of fitting of the data using the MAUD software for the unirradiated sample. The fitting was carried out including both texture and anisotropy. According to Popa [70], the first term in the polynomial expansion (Eq. 2.14) gives the

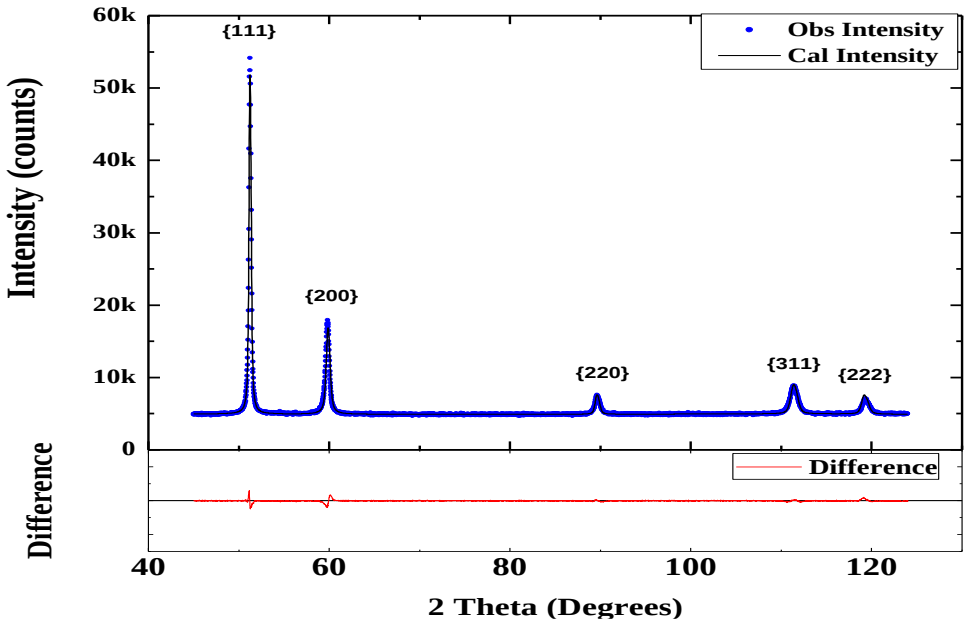

Fig. 3.7: Representative fitting pattern of the unirradiated sample by modified Rietveld method using MAUD

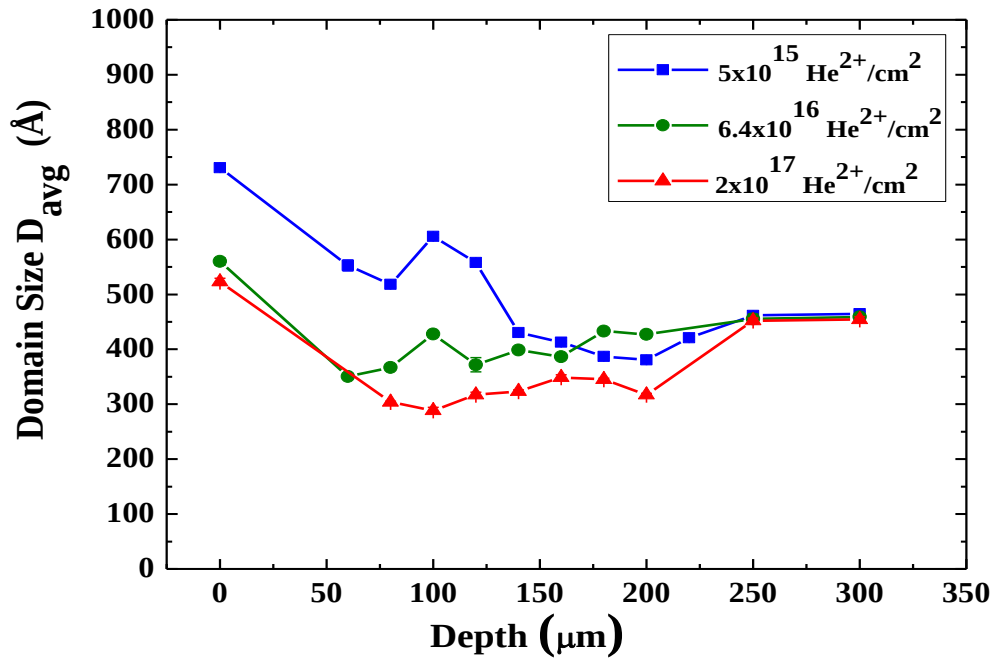

Fig. 3.8: Variation in domain size as a function of depth for three irradiated samples obtained from MAUD analysis

average radius of the composite crystallite. In the program MAUD [11,93], Eq. 2.14 is implemented in terms of the diameter of the crystallite (which can be called the average domain size). The value of the average domain size and the r.m.s. microstrain for the

unirradiated sample are found to be 460 ± 7 Å and 1.2 x 10^{-3} ± 1 x 10^{-4} respectively. Fig. 3.8 shows the variation of the average domain size obtained from the analysis of all the three irradiated samples as a function of depth. This is more or less similar to that seen in Fig. 3.5.

Table 3.2 shows the variation of the micro-strain as a function of depth for the irradiated samples. The results do not show much variation as a function of depth similar to that seen in the double Voigt analysis.

The advantage of using the whole pattern fitting procedure is that, one can calculate the effective domain size in each crystallographic plane. This helps in understanding the anisotropic contribution to the peak broadening. Fig. 3.9 (a-d) shows the plot of the effective domain size along the major crystallographic planes of the fcc structure (i.e. {111}, {200}, {220} and {311}) contributing to the analysis. The results along the {111} plane (Fig. 3.9(a)) is similar to that obtained by the double Voigt technique (Fig. 3.5) which is expected. But,

Table 3.2: Microstrain as a function of depth from the modified Rietveld analysis using MAUD

Depth	Dose: $5x10^{15}$ He^{+2}/cm^2	Dose:$6.4x10^{16}$ He^{+2}/cm^2	Dose:$2x10^{17}$ He^{+2}/cm^2
0	4.28E-4	4.70E-4	4.76E-4
60	4.11E-4	3.03E-4	-
80	4.16E-4	3.83E-4	3.00E-4
100	4.93E-4	3.17E-4	2.55E-4
120	5.27E-4	2.96E-4	2.46E-4
140	6.07E-4	3.28E-4	2.70E-4
160	1.28E-4	2.78E-4	3.02E-4
180	3.17E-4	4.16E-4	3.47E-4
200	3.26E-4	4.22E-4	3.35E-4
220	3.75 E-4	-	-
300	1.20E-3	1.20E-3	1.20E-3

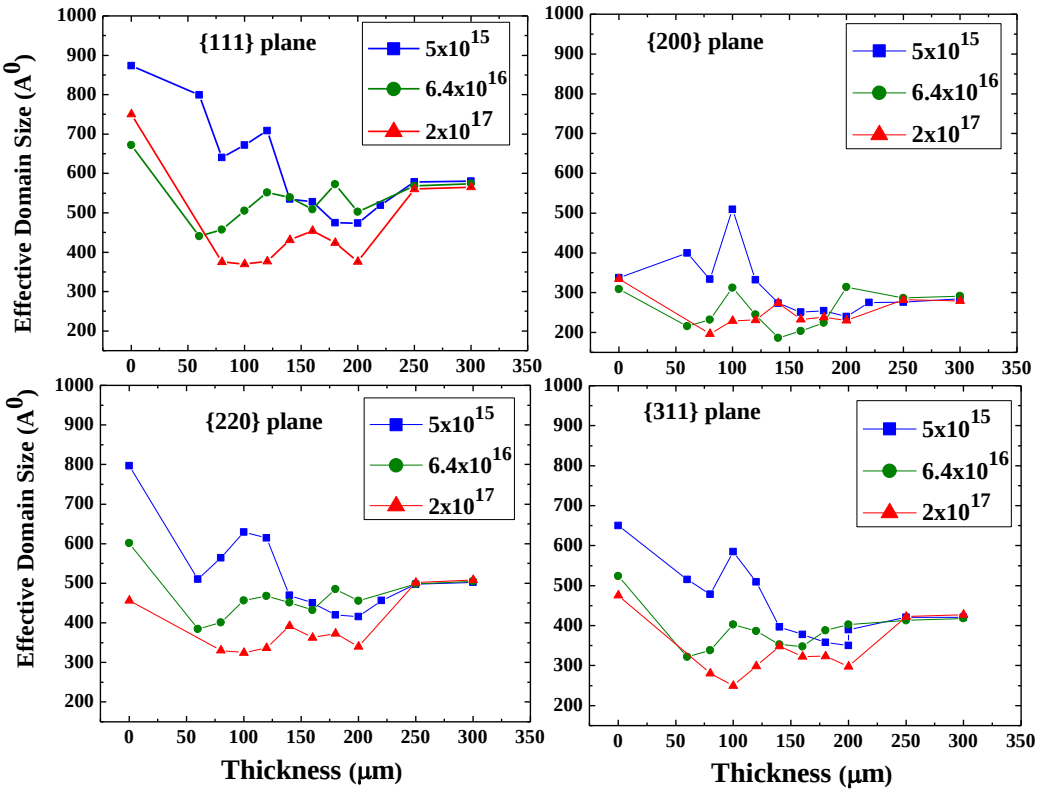

Fig. 3.9: Variation of effective domain size on each crystallographic plane (a) {111}, (b) {200}, (c) {220} and (d) {311}, for three irradiated samples, with depth obtained from Maud analysis

the domain size along the {200} plane is lower than the domain size in all other planes and does not show any significant change as a function of dose or depth.

On the other hand, the variation in domain size along the {220} and {311} plane shows more or less similar trend as that on the {111} plane. The change in the domain size is more prominent in the front face of the sample, where the domain size has increased in the first dose of irradiation and then decreased as a function of dose. Hence, the changes seen in the average values of the domain size (Fig. 3.8) can be attributed to the averaging effect of the changes seen mostly in the {111}, {220} and {311} family of planes.

All the above experimental observations can be reconciled as follows: The first and foremost observation is the increase in the domain size up to a certain depth in the lowest dose of irradiation. This can happen only if there are significant microstructural defects present in the unirradiated sample which can act as possible sinks for the irradiation produced

defects. In order to confirm this, the unirradiated sample was vacuum annealed at 1073K for 10 hours.

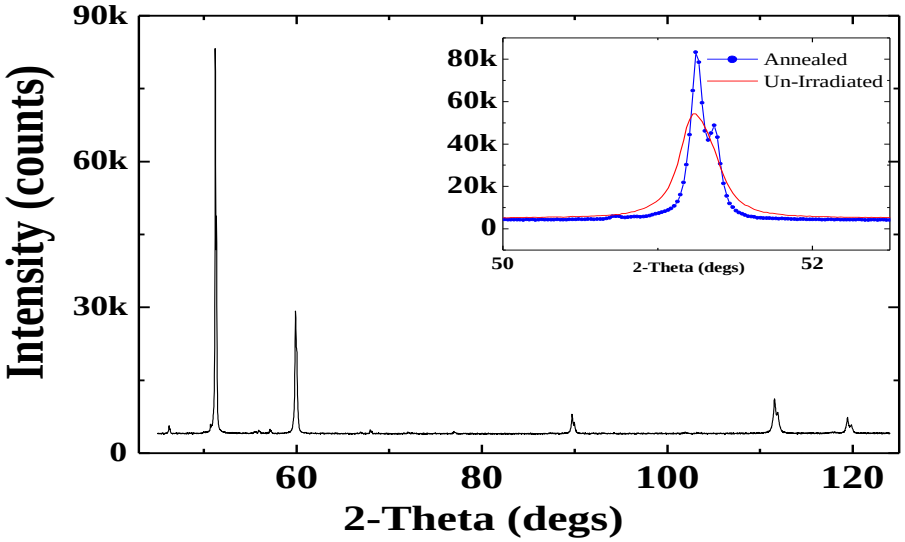

Fig. 3.10: X-ray diffractogram of the annealed sample. Insert shows the comparison of the (111) peak of the unirradiated and the annealed sample.

The X-ray diffractogram and the optical micrograph of the annealed sample are shown in Fig. 3.10 and 3.11 respectively. Insert of Fig. 3.10 shows comparison of {111} peak from unirradiated and the annealed sample. It is clearly evident from the figure that there is considerable decrease in the peak broadening. This indicates that the defects present in the

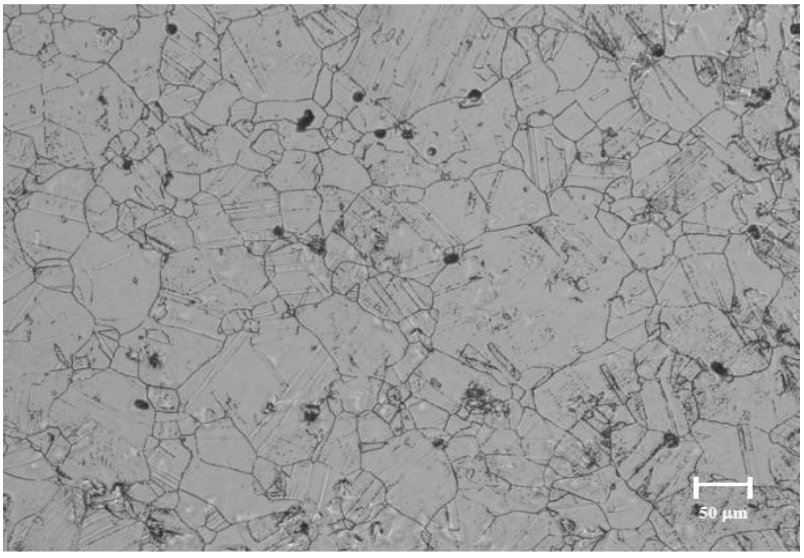

Fig. 3.11: Optical micrograph of the annealed sample.

unirradiated sample have annealed out causing a considerable increase in the grain size with a more homogenous distribution as seen in Fig. 3.11.

The X-ray data of the annealed sample was fitted using the modified Rietveld method (MAUD) and the average domain size and microstrain were found to be 1125 ± 13Å and $4.8x10^{-4} \pm 0.5x10^{-4}$ respectively. This clearly indicates that there is a significant change in the microstructure of the sample which can also be corroborated with the clear and prominent grain boundaries in the sample as seen in the optical micrograph (Fig. 3.11). Comparing the domain size and the microstrain values of the annealed and the unirradiated sample, it can be concluded that the sample used in this study had a large concentration of pre-irradiation defects in the form of network of dislocation clusters, dislocation loops etc. For low stacking fault energy materials such as stainless steel the pre-irradiation dislocation network will remain as dislocation arrays instead of forming cells [1]. The material under study is a variant of the stainless steel 316L and Hughes et al. have shown that the dislocations remain as arrays [95]. Further, helium ion irradiation is expected to produce spatially spread small clusters of point defects [2].The final microstructure resulting from the irradiation will then strongly depend on the interaction of the newly formed defects (vacancies and interstitials spatially spread as small clusters) with the pre-irradiation microstructural defects and also among themselves.

The observations in this study can be explained by taking recourse to the point defect balance equation for irradiation induced defects [2,80] and considering defects diffusion due to the defects concentration gradient. Thus defects concentration rate equations recalled from Chapter 1 (Eq. 1.3a and Eq. 1.3b) for further explanation.

$$\frac{\partial C_V}{\partial t} = K_0 - K_{IV} C_I C_V - K_{VS} C_V C_S + \nabla \cdot D_V \nabla C_V$$

$$\frac{\partial C_I}{\partial t} = K_0 - K_{IV} C_I C_V - K_{IS} C_I C_S + \nabla \cdot D_I \nabla C_I$$

The exact variation of the point defect concentration with time is complicated because of the influence of the various parameters in these equations. Nevertheless, an approximate solution for the time evolution of the defects and hence subsequently their influence on the properties were explained by Sizmann in a concise manner [2,80]. To a first approximation, the equations can be solved by assuming $\nabla C \approx 0$ and one can obtain two characteristic times τ_1 and τ_2 with $\tau_1 = (K_0 K_{iv})^{-1/2}$ and $\tau_2 = (K_{is} C_s)^{-1}$. τ_1 is the time up to which linear build-up of defect concentration occurs and τ_2 is the time to achieve quasi-steady state [2,80]. Sizmann [80] had obtained solutions for the point-defect rate equation depending on temperature and also on the concentration of pre-irradiation sink densities in a sample (low, medium and high). Our observations of variation of the domain size as a function of depth and dose can be explained by considering the case of low temperature irradiation and high sink density in solving the point-defect balance equation as suggested by Sizmann [80]. In this regime, $\tau_2 < \tau_1$ and since the mobility of the interstitials are more than that of the vacancies, the interstitials are annihilated in the pre-existing sinks before they can annihilate/recombine with the vacancies [2,80]. This causes an excess concentration of vacancies to be freely present for migration and further interaction among themselves or with sinks. In addition, the irradiation causes inhomogeneous damage along the depth of the sample (Fig. 3.1(a)) resulting in a large concentration gradient of defects within the range of damage (~200 μm). This inhomogeneous defect concentration opens up new channels [80] for the diffusion of the defects which results in an increase of migration of vacancies within the damaged region which finally may cluster and collapse to form dislocation loops or arrays thus changing the microstructure as a function of depth. This migration can occur over large time scales (~10^6 secs) and hence can alter the microstructure of the material even after a significant period of irradiation.

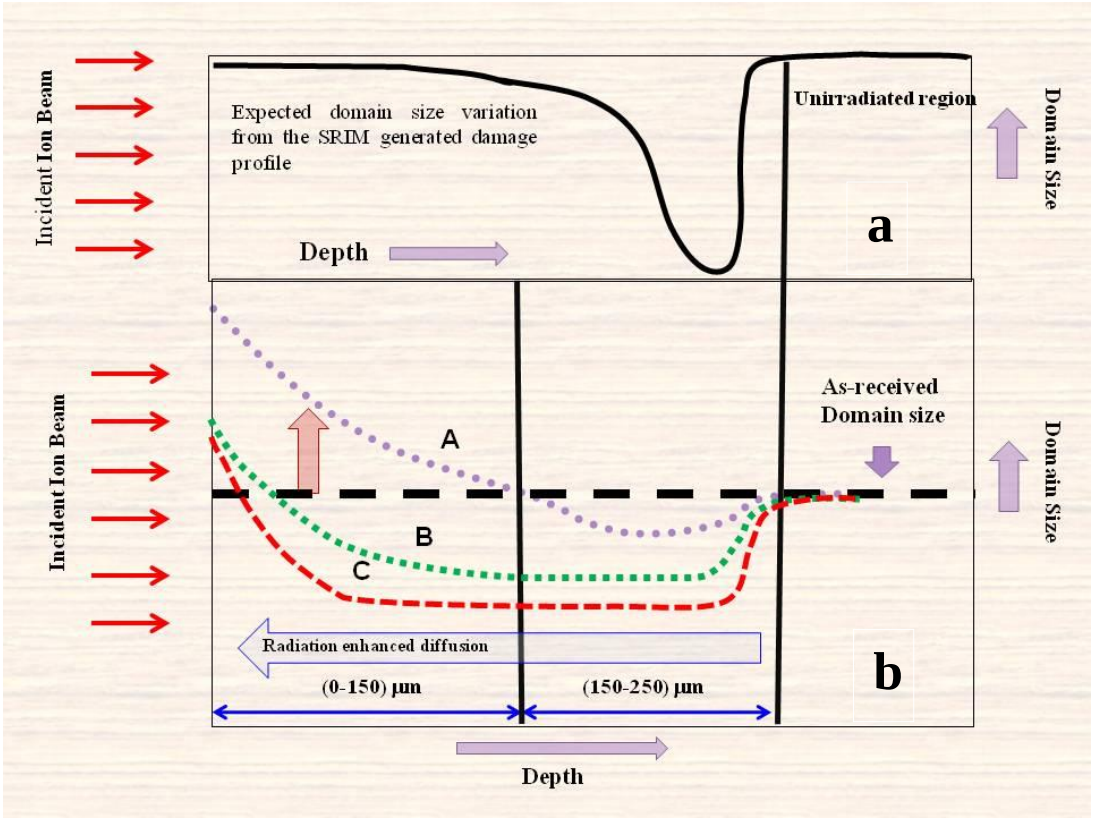

Fig. 3.12: The schematic diagram showing (a) Expected domain size variation as a function of depth assuming SRIM generated target displacement profile. (b) Summary of the results obtained in this study. Black dashed line indicates the domain size of the unirradiated sample. Curve A, B and C shows the variation in the domain size for the three doses of irradiation $5x10^{15}$ He^{2+}/cm^2, $6.4x10^{16}$ He^{2+}/cm^2 and $2x10^{17}$ He^{2+}/cm^2 respectively. Red arrow shows the increase in the domain size upon irradiation above the unirradiated value indicating that the defects that are produced during irradiation are annihilating in the pre-existing sink and hence decreasing the sink density. The blue arrow indicates the flow of defects due to radiation enhanced diffusion towards the front surface of the sample.

The schematic diagram (Fig. 3.12) summarises the results obtained in this study on the three samples. Fig. 3.12(a) shows the expected domain size variation as a function of depth from the damage profile obtained from the SRIM calculation (assuming that the irradiation has been carried out on a well annealed sample and no defects migration). The black horizontal line in Fig. 3.12(b) shows the domain size as a function of depth in the unirradiated sample (which is constant as a function of depth). Curve A, B and C show the variation of the domain size observed in 5×10^{15} He^{+2}/cm^2, 6.4×10^{16} He^{+2}/cm^2 and 2×10^{17} He^{+2}/cm^2 dose samples respectively.

Curve A in Fig. 3.12(b) shows the schematic representation of the variation of the domain size seen in the lowest dose sample ($5x10^{15}$ He^{2+}/cm^2). The domain size at the front surface is found to be much higher than that of the unirradiated region (see also Fig. 3.5 and Fig. 3.8). The value decreases as a function of depth but still remains higher than that of the unirradiated region till about 150 μm (This is indicated by the red arrow in Fig. 3.12(b)). Beyond this depth, it decreases below the value of the unirradiated region and shows a minimum at around 180-200 μm. This variation in the domain size as a function of depth can be explained by considering both diffusion of the defects from the peak damage region to the homogenous region and the annihilation of these defects at the pre-existing sinks in the sample. In the low dose sample, the defect density produced due to irradiation is low in the homogenous region and hence most of the freely migrating defects that are produced in the irradiation cascade are absorbed in the pre-existing sinks. In addition, the defects that are produced in the peak damage region can diffuse down the concentration gradient and also annihilate in the pre-existing sinks decreasing their concentration and hence increasing the domain size (This process of diffusion is shown as the blue arrow in Fig. 3.12(b)). The annihilation of the defects is predominant in the lower depth (< 150 μm) and hence this region can be called the annihilation dominated region.

Beyond 150 μm excess defects that are available after their annihilation at the pre-existing sinks can agglomerate and form new defect clusters in this region of the sample. These new defect clusters (dislocation loops or arrays) will now become predominant and affect the coherent region as seen by X-ray diffraction. Hence, the size of the coherent region will now start decreasing below that seen in the unirradiated region and this is seen as the decrease in the domain size beyond 150 μm and up to the peak damage region. This region can be called the irradiation induced damage dominated region. The value of the domain size at 250 μm and 300 μm depth in all the samples are almost the same as that of the unirradiated

sample. This indicates that the diffusion of the irradiation induced defects occur mainly towards the irradiated surface of the sample. This is because the diffusion is aided by the new channels that are made available due to irradiation which is only available in the depth from the irradiated surface up to the peak damage region.

With increase in dose (irradiation time), both the defect concentration and their migration increases (due to the concentration gradient) and hence, the formation of new defect clusters will become more uniform throughout the damage region. This is represented by the curve B (in Fig. 3.12(b)) which is a representative of the dose of 6.4×10^{16} He^{2+}/cm^2. On further increase in dose, these newly formed defect clusters may themselves start acting as sinks for the defect forming during the irradiation. Hence a quasi-steady state where there is both formation of defect clusters and their annihilation results in the tendency towards saturation of the domain size beyond a certain dose. This has also been observed in the irradiation studies of Ne^{6+} on SS316 samples [53]. The curve C shows schematically the variation of the domain size obtained in the highest dose (2×10^{17} He^{2+}/cm^2) sample in this study, where there is only a small decrease in the domain size in comparison to that of the intermediate dose sample (6.4×10^{16} He^{2+}/cm^2).

It is seen that in all the three samples the domain size in the front face of the sample is larger than the unirradiated sample. This could be due to the fact that in general surfaces act as infinite sinks for the defects [2]. However, with increase in dose, the domain size decreases marginally and shows a saturating trend. This could be due to the onset of the quasi-steady state where the formation of new defect clusters will act as sinks for subsequent irradiation formed defects.

The results obtained in this study are in contrast to that reported on 24MeV α irradiated Stainless steel by Shiraishi and Fukai [88]. Apart from the sharp increase in the Vickers hardness values near the end of the ion range, they have also reported sharp

variations in the Helium bubble density, bubble diameter and swelling across the peak damage region. We have not observed such variations in the domain size and/or microstrain as a function of depth. But, the results obtained in this study for the 5 x 10^{15} He^{2+}/cm^2 sample indicates that there is a systematic variation of the domain size as a function of depth which could only be explained if the diffusion of the defects is considered to play a significant role in the defect annihilation process in the pre-existing sinks and at higher doses, the more or less constant domain size (indicating a homogenous defect profile) seen as a function of depth indicates that enhanced defect diffusion is important in deciding the final microstructure of the irradiated sample.

3.6 Conclusion:

In summary, with the help of detailed X-ray diffraction line profile analysis, we could clearly show that there is significant variation of the microstructure caused by the irradiation induced defects as a function of depth in ion irradiated materials. The results clearly support the fact that the changes in the microstructure is decided by the combination of the presence of pre-existing sinks, the defect production rate, their enhanced diffusion and their annihilation rate in both existing and newly forming sinks. It is worth mentioning that the presence of pre-existing sinks plays a critical role in determining the damage homogeneity in the material. These help in preferential trapping of a particular type of defects thus enabling the diffusion of the complimentary defects much further away from the collision cascade region and hence paving way for a homogenous damage profile in the material. In our study of Helium irradiated D9 alloy, the unirradiated sample had significant amount of pre-existing sinks. It is seen that at low doses of irradiation when the defect concentration is less, the domain size shows a significant variation as a function of depth. As irradiation proceeds and the defect concentration increases, the pre-existing defects are completely annihilated and the defect diffusion now causes a more or less homogenous microstructure as a function of depth.

Chapter 4

A novel approach to analyse combined pre and post strain rate dependent phase transformation in tensile deformed SS304 using XRD and EBSD

4.1. Introduction:

The martensitic phase transformation is a reversible, diffusionless, crystallographic structural phase change observed in a class of steels, Ti-alloy, Ni-alloy etc. [31,32]. It is name after the German metallurgist Adolf Martens. The mechanism of this transformation was first described in a simple way by the metallurgist, Edgar Collins Bain and hence came to be known as Bain model [31,32], where the transformation is considered from fcc to bct or bcc. He showed that in steels a simple distortion can transform a fcc lattice structure to a bct or bcc lattice structure. Later, several other models were also proposed to explain this transformation i.e. KSN model (by Kurdjumov, Sachs and Nishiyama), Bogers and Burgers model etc. The transformation mainly goes through the two stages of (i) Nucleation and (ii) Growth of martensitic phases. It was observed that the nucleation of martensitic phase during the phase transformation occurred heterogeneously [96]. The elastic strain energy contributed by the shear related with the Bain transformation will suppress the homogeneous nucleation, though the interfacial energy of two phases is relatively low. The most favourable heterogeneous nucleation site is considered to be a dislocation whose strain field helps to nucleate new phase. The dislocation interaction energy will reduce the nucleation energy

barrier for this transformation. This martensitic phase also can form even at very low temperature where diffusion of atoms is not possible [24]. Martensitic phase can grow at a speed of sound in metal or metallic alloy like steel [24]. Also the chemical composition of martensitic phase is identical with the parent austenitic phase [24]**.** Since this phase transformation occurs at low temperature and at high speed fast with no change in chemical composition it also came to be known a diffusionless phase transformation. The growth rate of martensitic phase is determined by the movement of the inter-phase boundary of austenite and martensitic phases. Thus the interphase characteristic is very important for this transformation. During this phase transformation the atoms of parent phase will re-arrange but displacement of atoms does not exceed one atomic distance [96]. This phase transformation may occur due to the external stress or by change in temperature during cooling. The lattice will expand during this phase transformation and results a compressive residual stress in the parent austenitic phase [97]. This compressive stress will limit the maximum martensitic phase formation and significantly increase the fatigue strength [97]. Since this is a crystallographic structural phase transformation, thus a dramatic discontinuous change in elastic constant may be seen due to this transformation [98].

Present day challenge is to tailor materials with desirable properties and functionality to suite the diverse engineering applications. The need to utilize phase transformation and plasticity for designing high performance materials has revived the research interest in materials showing martensite transformations especially transformation-induced plasticity (TRIP) steels [99]. In general austenite stainless steels are low strength but high ductile alloys [100,101]. These steels are composed of metastable austenite phase and on deformation, these phases transform to strain induced ε-hcp and α'-bcc martensite phases. The martensite phase increases the work hardening of the material and thus leads to higher values of ultimate tensile strength but with a loss of ductility. Ductility can however be recovered by reversing

some of the martensite to austenite due to grain size refinement by controlled annealing [83]. The loss of ductility due to the martensite transformation can be prevented and also reversed if the deformation is carried out above a characteristic temperature which depends on the steel composition. Here the formation of martensite occurs only at high strains preventing the onset of necking and hence improving the ductility. This is referred to as transformation induced plasticity, where the formation of martensite helps in improving the ductility of the material[99].

4.2 Previous Studies and motivation:

The complex behaviour of deformation induced martensite (DIM) phase transformation in steels depends on several factors including initial microstructure, chemical composition, heat treatments etc. For a fixed composition and initial microstructure, the major factors that have a strong influence on the phase transformation are temperature and strain-rate. It is well documented that increase in the temperature suppresses the martensite transformation [102–105]. Olson and Cohen had also proposed a simple theory connecting the phase transformation rate with temperature [106]. The effect of strain-rate on the phase transformation has been studied over a vast range of deformation rates [40,76,77,107–110]. Effects of strain state (uniaxial tensile and biaxial tensile) and strain-rate (10^{-3}/sec and 10^{3}/sec) in SS304 has been studied in detail by Hecker *et.al* [109] and Murr *et.al* [108]. They could conclude that at low strain, high strain-rate experiments yielded more martensite than low strain-rates. However, at higher strain, low strain-rate yield more percentage compared to the high strain-rate. Hecker *et.al* showed that high strain-rates lead to lower amounts of martensite formation [12]. They argued that high strain rates lead to adiabatic heating causing increased stability of austenite phase [109]. Arpan *et.al.* have carried out characterisation of martensite formed during uniaxial tensile deformation of SS304 LN [40] under strain rates varying from $1x10^{-4}$ /sec to 1/sec. They could conclude that when the strain-rate is increased,

the total volume fraction of martensite decreases which again was attributed to suppression of phase transformation due to temperature rise at high strain rate. They could show that higher strain rate initiated the formation of the martensite at a lower strain but lower strain-rate yielded the maximum volume fraction of martensite at fracture [40]. Experiments by Hokka and Isakov *et.al.*, have showed that strain rate itself may play a decisive role on the rate of phase transformation [76,110]. Hokka showed that there is large difference in the percentage of martensite formed between the low strain-rate (quasi-static) and high strain-rates even at low plastic strains (where the effect of deformation induced heating is absent) [110] which could not be accounted for by the variation of strain-rate alone. Isakov *et.al*. performed tests where the strain-rate was suddenly increased by 4 orders of magnitude resulting in a deceased strain-hardening rate which could not be explained by adiabatic effects alone [76]. In order to uncouple the effect of strain-rate and adiabatic heating in strain induced phase transformation Vazquez-Fernandez *et.al*, [111] have performed experiments covering a large strain rate in both isothermal and adiabatic conditions on AISI 301LN steel. They could show that at high strain-rate and at low strains, the adiabatic heating alone cannot explain the reduced phase transformation rates and strain-rate seems to play an important role. The effect of prior martensite on the strain-induced martensite formation has been studied by P. Mukherjee *et al.* in AISI 304 SS using acoustic emission [85]. They reported that the during the tensile testing, the acoustic emission signals corresponding to the formation of martensite could be observed to much larger strain in samples with prior martensite compared to that of samples with no prior martensite. All the above studies indicate that during deformation, the martensite formation is a highly complex phenomena depending on the strain-state, strain-rate and also the presence of prior martensite in the material.

In this study we have tried to address the following questions in DIM phase transformation of metastable austenite steels during uniaxial tensile deformation: (1) can a

combination of different strain-rates yield higher martensite fraction than a single strain-rate (2) what is the role of prior martensite in yielding higher martensite fraction and (3) what is the critical role of the microstructure of the prior martensite that determines the final martensite fraction.

4.3 Brief description of the work:

We have carried out this study using uniaxial tensile measurement on AISI 304 steel. Considering the various studies from detailed literature survey briefed above, we have selected a combination of pre-strain (0.4, 0.45 and 0.5), pre-strain rate (10^{-1}/sec and 10^{-2}/sec) and post-strain rates ($1x10^{-4}$, $5x10^{-4}$ and $1x10^{-3}$/sec) to carry out this study. The details of the samples are given in the experimental section below. Several complimentary techniques have been used for characterizing the austenite and the martensite phases and also to gather detailed information on the microscopic details of the transformation such as the phase boundaries etc.

The main tool used for the quantification of the martensite phase in this study is the X-ray diffraction technique. Magnetization measurements have also been used to support the results. Detailed Electron Back Scattered Diffraction measurements have been carried out on selected samples in order to characterize the phase boundaries between the austenite and the martensite phase. Additionally, Differential Scanning Calorimetry has also been used to calculate the stored energy in the deformed material.

4.4 Experimental and characterisation details:

The tensile deformation was carried out by controlling the extension rate corresponding to the required strain rate using the Universal Testing Machine. Each tensile sample was deformed with a different combination of high strain rate (10^{-1} to 10^{-2}/sec) followed by low strain rate

(10^{-3} to 10^{-4} /sec) up to fracture. After the pre-strain, the samples were removed from the testing machine and left to relax to remove the elastic strain. Further tensile experiment (post-

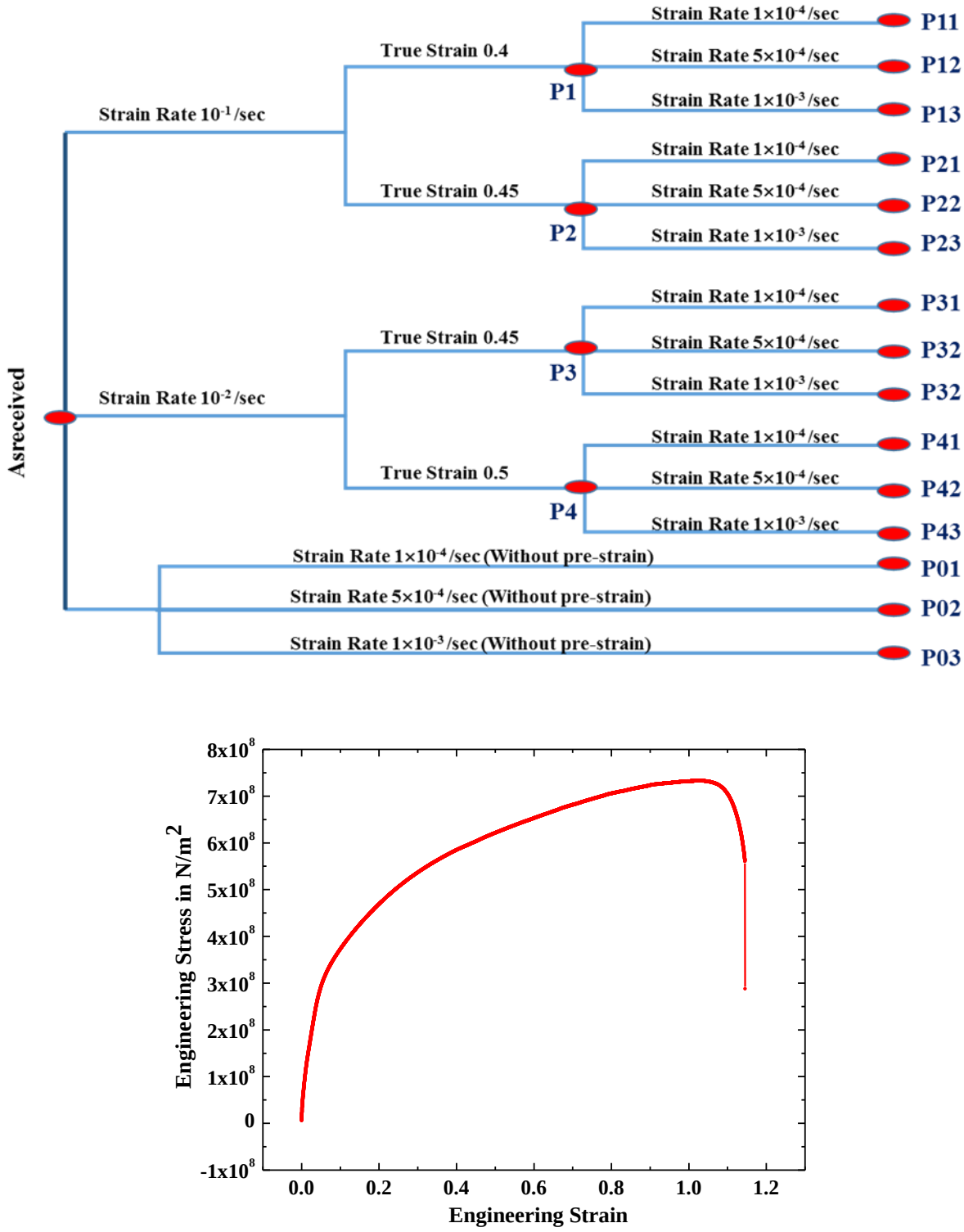

Fig. 4.1: a) Experimental chart for tensile test b) Engineering stress strain curve of the tensile test at strain rate $1x10^{-4}$ / sec

strain) was carried out on the relaxed samples. The sample labelling was done according to the pre-strain, pre-strain rate and the post-strain rate and is shown in detail in Fig. 4.1(a).

Four types of different pre-strain samples were prepared: Samples with strain rate of 10^{-1}/sec and true strain of 0.4 and 0.45 and samples with the strain rate of 10^{-2}/sec and true strain of 0.45 and 0.5. These samples were again subjected to tensile test up to fracture with three different strain rates of 10^{-4}/ sec, 5 x 10^{-4}/sec and 10^{-3}/ sec. Three samples were also deformed up to fracture directly without any pre strain with a same strain rate as above (10^{-4}/ sec, 5 x 10^{-4}/sec and 10^{-3}/ sec). In total, twenty number of samples: 12 samples with both pre-strain and post strain, 4 samples with only pre-strain, 3 fractured samples with only post strain (no pre-strain) and 1 as received sample were subjected to further characterization using both macroscopic and microscopic techniques. Each sample is different by at least a minimum of one parameter i.e., pre-strain or pre-strain rate or post-strain rate. A representative engineering stress strain curve of the tensile test at strain rate 1×10^{-4}/sec is shown in the Fig. 4.1(b).

4.4.1 X-ray diffraction (XRD):

Phase identification (γ-austenite-fcc and α'-martensite-bcc), quantification and microstructural characterisation were carried out on all the twenty samples using X-ray diffraction (XRD) technique. The XRD data was collected using Bruker D8 Advance X-ray diffractometer with Co-K_{α} X-ray source. XRD pattern was obtained in the Bragg-Brentano geometry with a step size of 0.02^0 and time per step was 1 sec in the range of 2θ from 45^0 to 124^0. The average depth from which the XRD data is collected is about ~ 16μm. The diffraction data was corrected for instrumental broadening effects during the analysis stage by using the XRD data of the NIST standard LaB_6 powder sample collected using the same experimental parameters. Since the main aim of this study is to quantify the martensite phase

formed during deformation as a function of strain and strain-rate, it is important to use analysis techniques, where the newly formed phase can be quantified. Also, in order to understand microstructural changes that are taking place during the deformation, it is required to evaluate systematically the microstructural parameters, such as domain size and microstrain within the domain in the parent phase and the newly formed phase in the deformed samples. Different techniques such as WH, MWH, MAUD and CMWP have been used to carry out detailed X-ray LPA of the XRD data.

Here, the modified Rietveld technique (detailed in section 2.3.2, Chapter 2) has been used for both phase quantification and also determination of the microstructural parameters of the phases. The XRD data of all the samples were fitted by introducing two different crystallographic information files (CIF), one for the parent austenite (fcc) and another for the deformation induced martensite phase (bcc). The fitting was carried out by refining the back-ground, the phase percentage and the lattice parameters in the 1^{st} step. In the 2^{nd} step, the microstructural parameters (domain size and microstrain) were also refined. Finally, the texture formed due to the uniaxial tensile stress was refined by using the spherical harmonics model [112,113]. The final fit parameters are then the lattice parameters of the phases, the phase percentages and the microstructural parameters of the two phases.

For more detailed insight on the nature of the defects Convolutional Multiple Whole Profile fitting (CMWP) along with modified Williamson-Hall technique have been used on a few selected samples. The details of these two techniques have already been described in section 2.3.2, Chapter 2.

4.4.2 Vibrating Sample Magnetometer (VSM):

Magnetic measurements have been carried out to help determine the amount of the martensite phase in the deformed samples as a complimentary technique of XRD. The martensite phase

in stainless steels is magnetic in nature and hence the value of the saturation magnetisation gives an estimate of the martensite phase formed in the samples. The samples used for the magnetic measurements were of approximate dimension 1 mm x 1 mm x 3 mm (with weight 70-100 mg). The details of the magnetic measurement were already given in section 2.5, Chapter 2. The magnetic hysteresis loop was measured over the full cycle and the saturation magnetisation (Ms) and the coercive field (Hc) were calculated for each sample.

4.4.3 Differential Scanning Calorimetry (DSC):

In this study, the thermogram measurements have been carried out on some of the samples to supplement the quantification of the martensite using XRD and magnetisation measurements. The heat flow measurements were carried out on small pieces (weighting about 50-70 mg) cut from near the fractured surface of the as-received sample, one pre-strain sample (P1) and three fractured samples (P03, P11 and P13) using the Simultaneous Thermal Analyzer. The thermograms were measured in the temperature range of 298K to 1200K with a heating rate of 40K/min using ($Pt+Al_2O_3$) heating pan. The heating curves of the samples were measured twice and the difference between the two scans was calculated. The second run is required to subtract the heat capacity variation of the sample with temperature. The difference between the two scans gives the absolute value of the energy released or absorbed by the sample. Prior to each set of measurement, the empty pan run was carried out with the same heating rate to obtain the instrumental back ground.

4.4.4 Electron Back Scattered Diffraction (EBSD):

Electron back scattered diffraction (EBSD) measurements has been specifically used to characterise the boundary between the austenitic and martensitic phases in this study. The measurements were carried out on a few selected samples (the choice of the samples will be explained in the results section below) using Field Emission Scanning Electron Microscope.

Small pieces (size ~ 10 mm x 10 mm) of samples were electro-polished using a solution of perchloric acid and acetic acid under 40V at -18C for 20-30 secs. These were mounted on a 70 degree pre-tilted sample stage and subjected to Electron back scattering diffraction analysis. All experimental parameters, such as electron accelerating voltage (20 kV), aperture size (120 μm), distance between sample and detector and image magnification were kept the same for all the samples. The data was measured with a scan area of 185 μm x 250 μm and a step size of 520 nm. A magnification of 350x was chosen so that good statistics of the phase boundaries can be obtained. It is to be noted that in deformed samples, due to the presence of strain in the material, the number of indexed points decreased (number of non-indexed point increases) as compared to the as-received sample. Hence, in order to avoid ambiguity in the results due to the varying non-indexed points the EBSD data has not been used for quantification of the phases fcc and bcc. However, the data were used to analyze the Lattice correlation boundaries (LCB) and Orientation relationship boundaries (ORB) between the two phases.

4.5. Results and Discussion:

Fig. 4.2 shows two representative XRD patterns of as-received sample and one deformed sample (P01). The formation of martensite phase in P01 can be clearly observed. All the peaks of the as-received sample could be indexed to the fcc lattice. However, no discernible peaks corresponding to bcc phase could be observed in the as-received sample. All the new peaks in XRD pattern of the deformed sample could be indexed to the martensite phase with phase group Im-3m (bcc). It can also be observed that all the crystallographic peaks of both the austenite and the martensite phase of P01 sample are broadened which indicates the presence of deformation induced defects (mainly dislocations) in both phases.

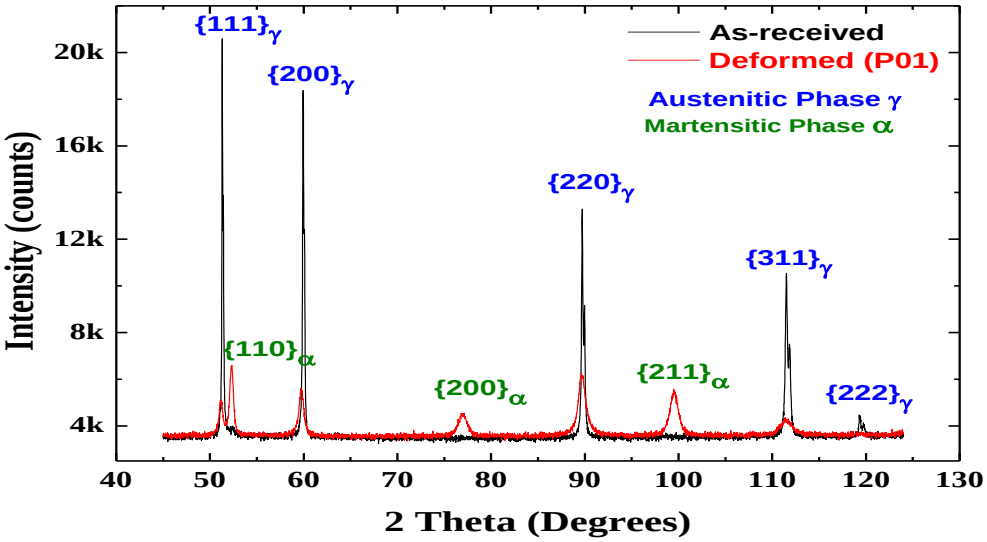

Fig. 4.2: XRD patterns of as-received and deformed sample with a strain rate of $1x10^{-4}$/ sec (P01)

In order to quantify the martensite percentage and also to extract the microstructural parameters (domain size, microstrain, dislocation density and the dislocation character) in the

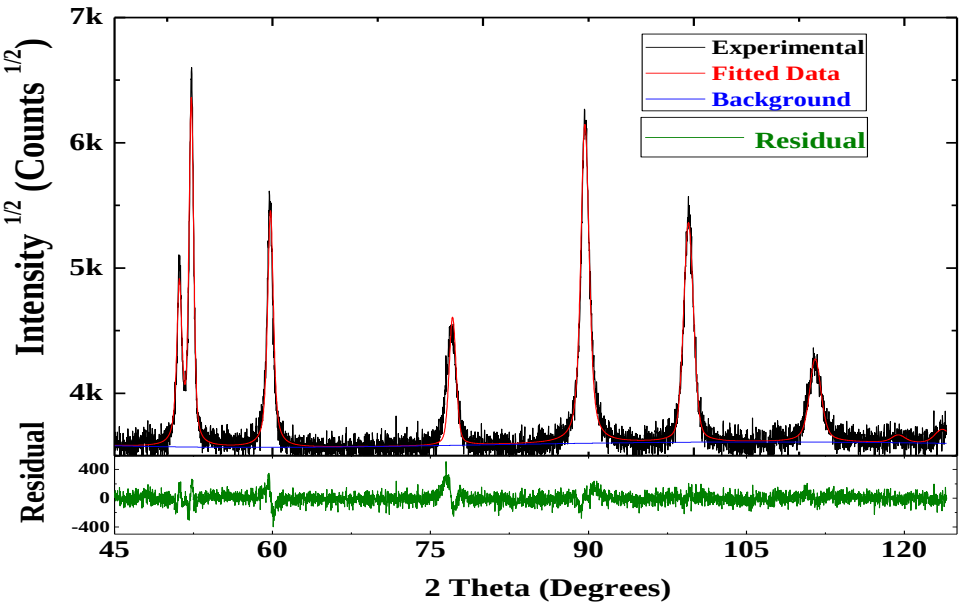

Fig. 4.3: XRD pattern fitting using Maud software for fracture sample (P01) with strain rate 1×10^{-4} / sec

two phases, detailed Line Profile Analysis (LPA) was carried out on the XRD data. The first LPA analysis was carried out using the modified Rietveld method utilizing the MAUD software. Here, the two phases were fitted with two different crystallographic information

files (CIF), one for the austenite fcc phase and other for the martensite bcc phase. A representative fitted pattern is shown in Fig. 4.3 for P01 (deformed) sample.

The amount of martensite phase estimated from the XRD data is plotted in Fig. 4.4 for all the deformed samples. It can be observed that all the four pre-strained samples (P1, P2, P3 & P4) show a small amount (6-8%) of martensite phase. All the other (fractured) samples show significantly high martensite percentage (greater than 30%) depending on the strain and strain rates used during the tensile test up to fracture. The most interesting observation is that, only two samples i.e., P11 & P12 show much larger martensite percentage (~ 60%) compared to the rest. It is also important to note that, although all the three samples (i.e., P11, P12 and P13) in the P1 series have the same pre-strain history (P1 series samples have a true strain of

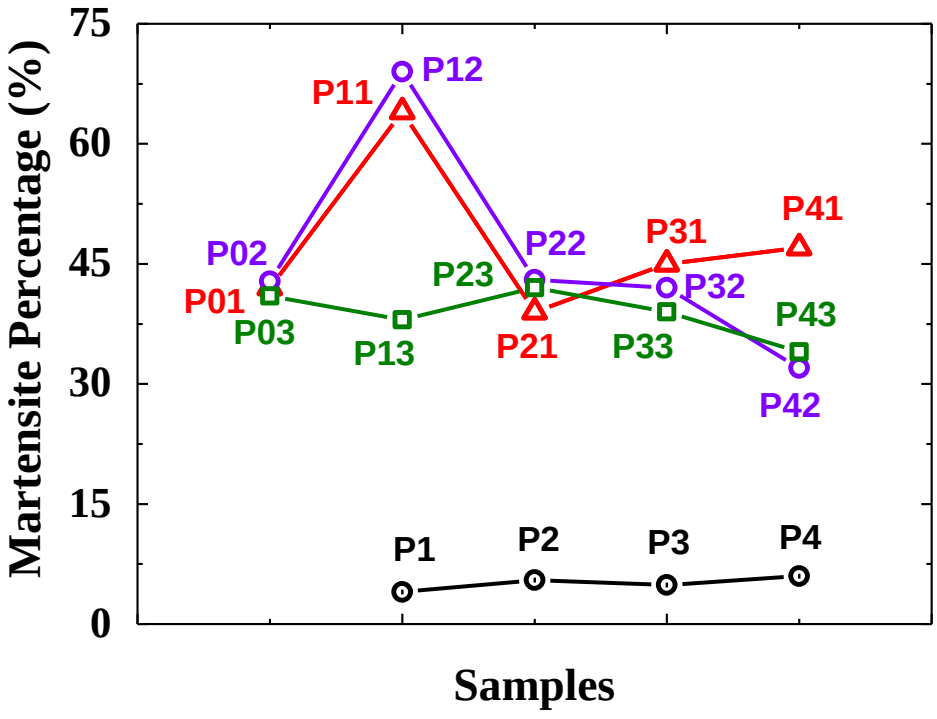

Fig. 4.4: Martensite percentage from the modified Rietveld fitting of the XRD data using MAUD software

0.4 and have been deformed with a strain rate of 10^{-1}/sec), only the P11 (post-strain rate $1x10^{-4}$ /sec) and P12 (post-strain rate $5x10^{-4}$ /sec) samples show a large martensite percentage. It is also a significant observation that these two samples (P11 & P12) shows more amount of martensite phase than that of the P01 & P02 samples (samples without any pre-strain, but have been deformed up to fracture using the same post-strain rate as P11 and P12 respectively). This result clearly shows the effect of pre-strain in the samples on the martensite transformation.

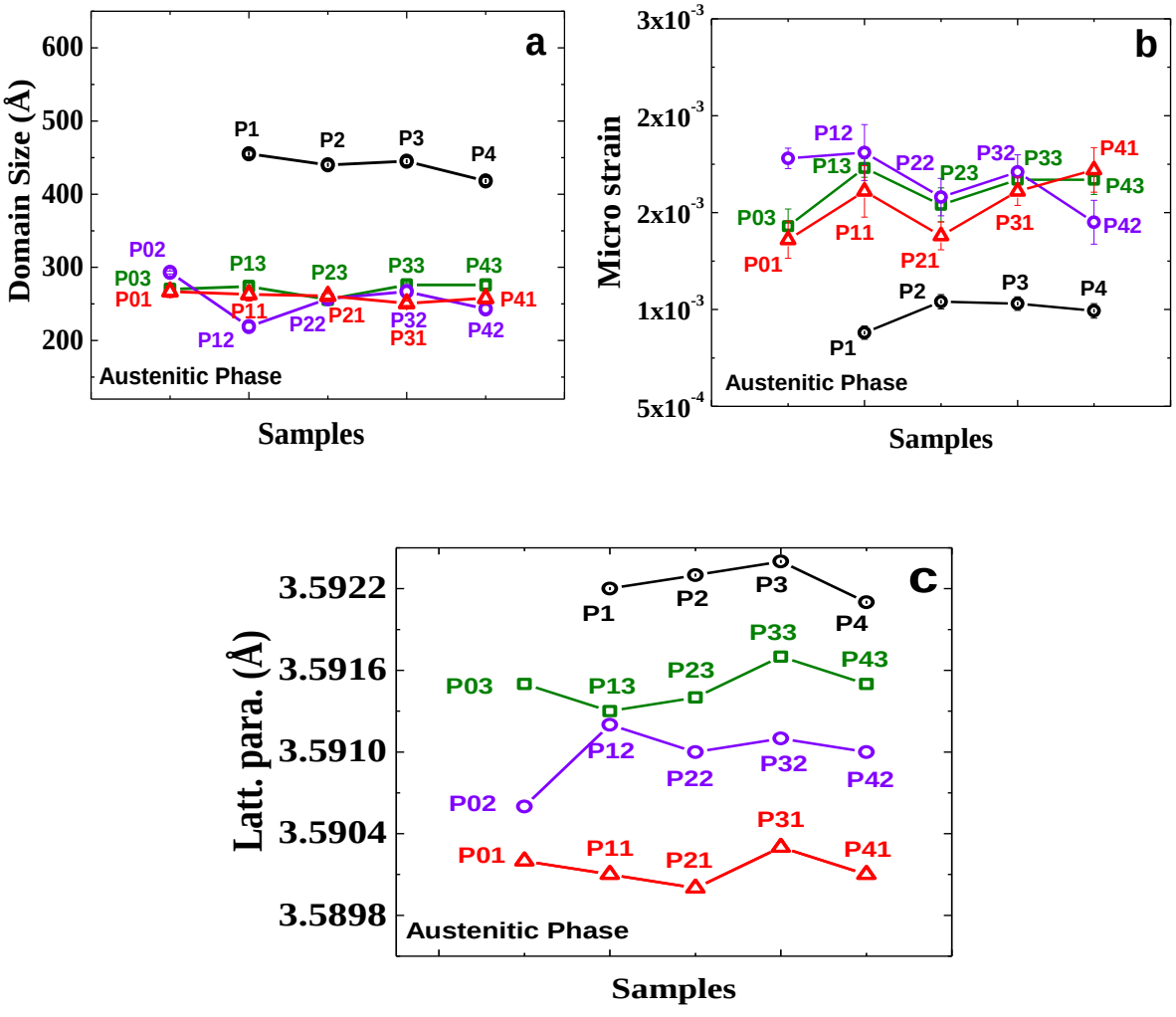

Fig. 4.5: (a) Surface weighted domain size, (b) r.m.s. micro-strain and (c) lattice parameter variation of the γ-fcc phase for all deformed samples.

The average domain size (D_s) and the r.m.s. micro-strain ($<\varepsilon_L^2>^{1/2}$) of both the austenite and the martensite phase were evaluated as a fitting parameter from the modified Rietveld method. The as-received sample had surface weighted domain size of 1835 (± 14) Å and a microstrain of 1.68E-4 (± 1.68E-7) as obtained from the fitting. The microstructural parameters (surface weighted domain size, r.m.s. micro-strain and lattice parameter) of the austenite phase of all the deformed samples are plotted in the Fig. 4.5(a), 4.5(b) and 4.5(c) respectively. The values of domain size and microstrain (of the austenite phase) of the pre-strained samples (P1, P2, P3 & P4) is plotted in Fig. 4.5. The domain size is lower and microstrain is higher than the corresponding values of the as-received samples which is a clear signature of deformation. It is also interesting to note that the domain size values of all the pre-strain samples are more or less the same. However, there is a small difference in the microstrain values among them. The microstrain of the P1 sample is slightly lower compared to that of the other three pre-strained samples. This is an interesting observation which may be helpful in understanding the higher martensite formation in P1 series. The microstructural parameters of the austenite phase of all the fractured samples are significantly different from the pre-strained and as-received sample as expected. The domain size values of all the samples are more or less same and in the range of 210-280 Å. The decrease in the domain size with increasing deformation (pre-strain and fracture) indicates that the significant change in the coherent region due to formation of deformation induced defects in the austenitic phase. The microstrain values (Fig. 4.5(b)) of the fractured samples (ranging between 1.3 x 10^{-3} to 1.8 x 10^{-3}) are greater than that of the as-received and pre-strained samples. This also corroborates with the earlier observation and indicates the accommodation of deformation in the austenite phase resulting in significant micro-strain within the domain in the samples.

Fig. 4.6(a) and 4.6(b) shows the microstructural parameters obtained for the deformation induced martensite phase. The domain size in the newly formed martensite

phase does not show any systematic behaviour as a function of deformation (i.e., there is no clear difference between the domain size values of the pre-strained and the fractured sample). However, a few observations can be made from Fig. 4.6(a). The deformation induced martensite phase in the pre-strained samples and the fractured samples with post-strain rate of 1 x 10^{-4}/sec (P1-P4, P11, P21, P31 and P41) have coherent regions of similar size ~ 675 (± 50) Å. However, the domain size of the post strain samples deformed with a strain rate of 10^{-3}/sec, shows a decreasing trend with increasing pre-strain and pre-strain-rate (P03, P13, P23,

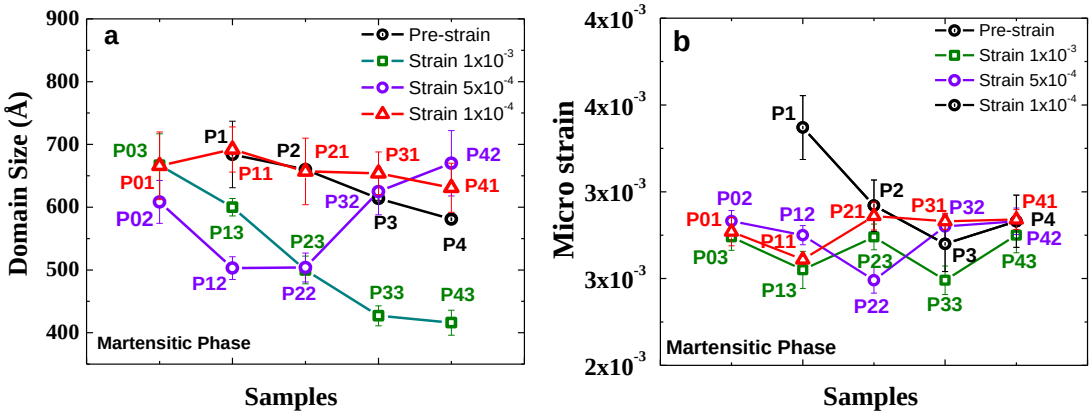

Fig. 4.6: (a) Surface weighted domain size and (b) r.m.s.microstrain variation of the martensite phase of all deformed samples

P33, and P43). On the contrary, the microstrain of the newly formed martensite phase does not show any variation among all the deformed samples, except for the sample P1. All the samples (except P1) have a relatively high microstrain (between 2.5 x 10^{-3} and 3.0 x 10^{-3}) compared to the austenite phase, with P1 showing even higher microstrain (~3.5 x 10^{-3}). This is an important observation that will be invoked at a later part to explain the formation of higher martensite fraction in the P1 series samples. It is worth mentioning here that the martensite phase due to its lathe-like structure is morphologically different from the more isotropic austenite phase and hence may inherently have a large microstrain compared to the austenite phase.

The lattice constant of the crystallographic phases is also an important parameter during the LPA of the XRD data. Fig. 4.5(c), shows the variation of the lattice parameter of the austenite phase of all the deformed samples. The as-received sample has a lattice parameter of 3.5941 ± 0.0002 Å. It is clear from Fig. 4.5(c) that the lattice parameter of the austenite phase of the deformed samples systematically changes as a function of deformation. The pre-strained samples have a lower lattice parameter compared to the as-received sample (the change is ~0.05%). The fractured samples show a further decrease in the lattice parameter compared to the pre-strained sample. Moreover, the decrease is systematic with respect to the post-strain rate used for the deformation of the samples. The samples which have been deformed using the strain-rate 1 x 10^{-4}/sec (the lowest in this study) show the maximum change in the lattice parameter (~0.14%) with respect to the as-received sample, followed by the intermediate strain-rate samples (strain rate 5 x 10^{-4} /sec and change of ~0.09%). The samples deformed using the strain-rate 1 x 10^{-3} /sec (highest post strain rate used in this study) shows the lowest change in the lattice parameter (~0.07%) among all the fractured samples. The decreasing lattice parameter clearly indicates that the austenite phase is subjected to a compressive stress from its surroundings which is the martensite phase formed during the deformation. This compressive stress in the parent phase may be one of the deciding factor to control the formation of the martensitic phase in the materials [114].

Magnetic measurements on the as-received and deformed samples have been performed to substantiate the results of the XRD analysis to understand the martensite phase formation. It has to be noted that the magnetic measurements were carried out using small pieces of the samples cut close to the fractured surface of the deformed samples. The M-H loop was measured for all the samples up to a maximum field of 3 Tesla. In Fig. 4.7, the magnetization obtained in terms of the magnetic moment/gm is plotted for a few representative samples. Inset of Fig. 4.7 shows the M-H curve for the as-received sample. It

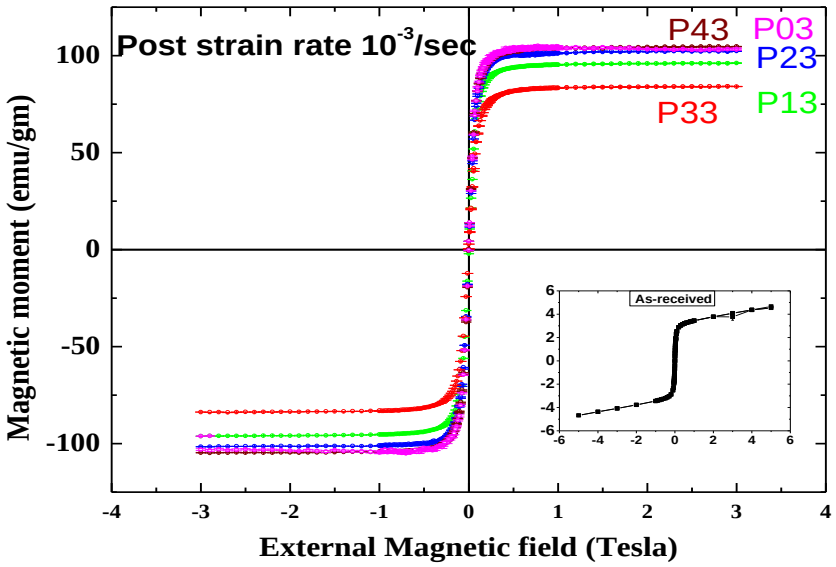

Fig. 4.7: M-H loop of a few representative deformed samples. Inset: M-H loop for the as-received sample

is evident from the inset, that there is no sign of saturation of the magnetic moment even up to 5 Tesla in the as-received sample. This is typically the behaviour of a paramagnetic sample [115]. The magnetic moment (through small) arising in this sample could be due to the very small amount of martensite phase (but sparsely dispersed) present in the as-received sample. The magnetic moment at 3T is 4.63 emu/gm and the cohesive field (Hc) is ~1.38 x 10^{-4} Tesla.

In order to understand the magnetic contribution in the deformed samples, the saturation magnetic moment and the cohesive field of all the samples (except that of the as-received one) are shown in Fig. 4.8(a) and 4.8(b) respectively. It can be clearly seen from Fig. 4.8(a) that the saturation magnetic moment of the pre-strained (P1-P4) samples are lower compared to that of the fractured samples, however, the values of all the deformed samples are much higher compared to that of the as-received sample. This is a clear indication of the formation of the martensite phase (which is magnetic) in the deformed sample. It can also be seen from the Fig. 4.8(a) that the nature of the variation of the saturation magnetic moment is similar to that of Fig. 4.4. P11 and P12 samples show the highest saturation magnetic

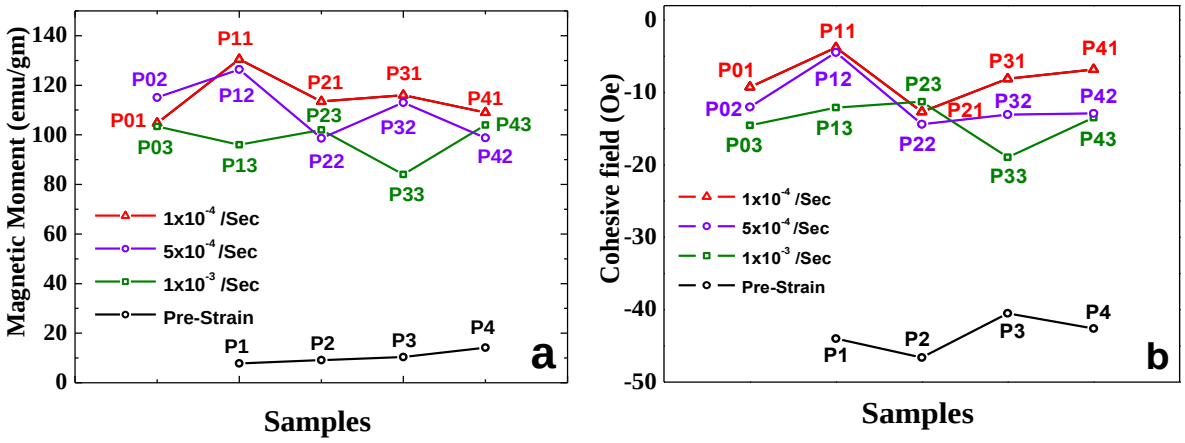

Fig. 4.8: (a) Magnetic moment and (b) Cohesive field for all the deformed samples

moment indicating that these samples have the highest martensite phase. This is in agreement with the martensite percentage obtained from the XRD analysis (Fig. 4.4). Fig. 4.8(b) shows the coercivity of the samples extracted from the B-H loop data. The pre-strained samples show much larger coercivity compared to the fractured samples. This observation is similar to that reported earlier by Mumtaz *et.al.*[116]. They have also reported that the coercive field decreases with increasing deformation and have attributed it to the formation the magnetic phase of different size and shape [116].

From the above study using XRD and VSM it can be concluded that the amount of martensite formed during the deformation of SS304 is highly sensitive to the combination of the pre-strain and the pre and post strain rate used for the deformation. Thus among all the samples studies, the samples deformed with a strain rate of 10^{-1}/sec to a pre-strain of 0.4 (P1 series) and then subsequently deformed to fracture with a strain-rate of $1x10^{-4}$/sec and $5x10^{-4}$/sec seem to show the highest martensite percentage (Samples P11 and P12). This indicates that a high pre-strain rate and a low post strain rate along with a particular pre-strain value is a necessary combination to obtain a large amount of martensite.

In order to obtain more detailed information regarding the microstructural difference among the pre-strained samples and to ascertain the difference within the P1 series samples (i.e., between P11&P12 and P13) the XRD data of some selected samples were analyzed using the CMWP analysis. As mentioned earlier, in this method, the strain contribution to the XRD line broadening is assumed to be arising due to dislocations alone. Among the fitting parameters related to the dislocation contribution to the line broadening, the factor (q) signifying the dislocation character (i.e., edge or screw) dictates the contrast factor of the dislocations. This has been calculated using the modified W-H method. To estimate the theoretical limits of the q value the following procedure has been followed. The contrast factors of dislocation in each individual diffraction plane (C_{hkl}) of Fe (fcc) have been calculated for different dislocations using the program ANIZC [61]. The edge dislocations with slip system <110> {111} and screw dislocation with slip system <110> are considered for the analysis. The elastic constants used for this calculation are C_{11} = 207 GPa; C_{12}=132 GPa; C_{44}=123 GPa [117]. From the calculated value of contrast factors of different planes, the average value of contrast factor for {200} reflection and the value of q are evaluated using Eq. 2.17 for both the edge and screw dislocations respectively. The limit of q corresponding to edge and screw character is 1.604 and 2.392 respectively. The average value of contrast factor for {200} reflection for edge and screw dislocations are found to be 0.292 and 0.302 respectively. It is worth mentioning here that the theoretical values have been estimated using the elastic constants of pure- fcc Fe and variation in the elastic constants due to alloying elements may vary the limit of the q values for the edge and screw dislocation.

These values of the average contrast factor for all the reflections were initially used for plotting the modified W-H plot. Fig. 4.9(a) and 4.9(b) shows the W-H and the modified W-H plot of the as-received, pre-strained (P1-P4), P11 and P13 samples. The values are then

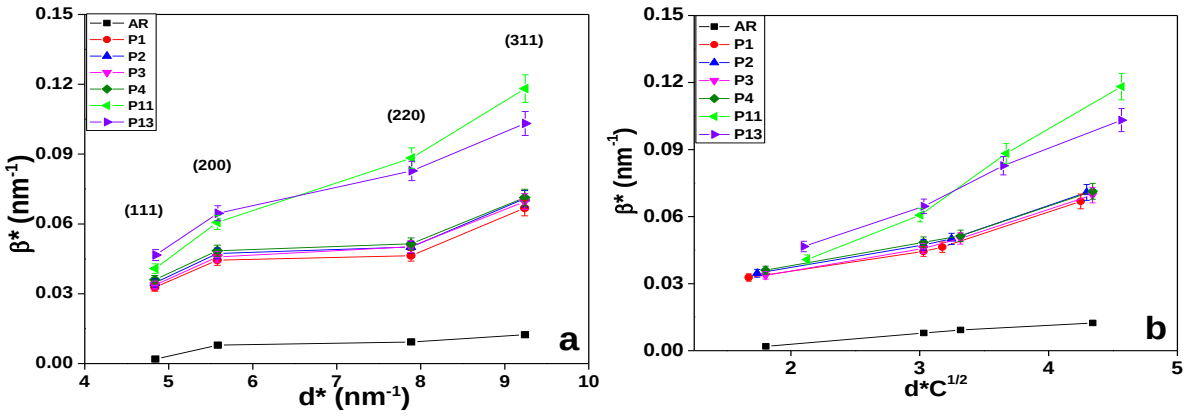

Fig. 4.9: (a) Williamson-Hall and (b) Modified Williamson-Hall plots for the as-received, pre-strained (P1-P4) and P11 & P13 samples.

iterated to obtain a self-consistent solution using the modified W-H equation (Eq. 2.5). The new (final) values of q obtained for all the evaluated samples are plotted in Fig. 4.10. Comparing these values with the theoretical estimate obtained for the edge and screw dislocations, it can be concluded that the dislocations are mostly of edge type is all the samples including the as-received sample.

The q values of the fractured samples (P11 and P13) are however much lower than the calculated limit for the edge dislocation. An important observation of the variation of q is the

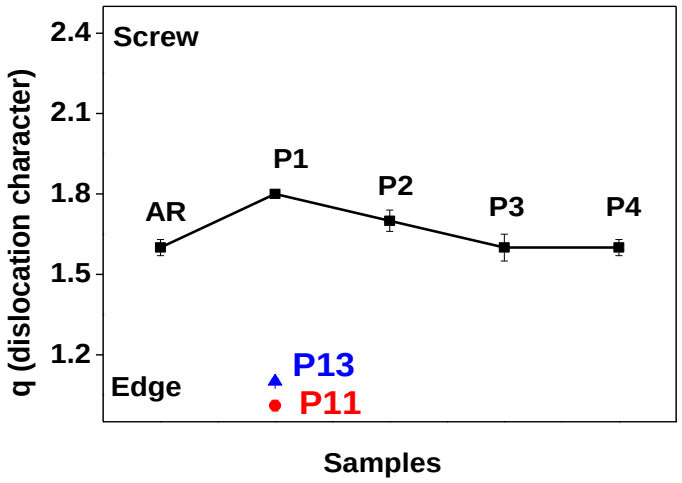

Fig. 4.10: Dislocation character (q) obtained for the best fit of the modified W-H plots of the samples.

fact that there is a small but noticeable increase in its value of the P1 sample compared to other pre-strained samples. This indicates that the dislocations that are formed in the P1 sample may be dominantly of screw type, resulting in an increase in the q value. Using the q values obtained from the modified W-H plot, the detailed LPA analysis using CMWP method was carried out.

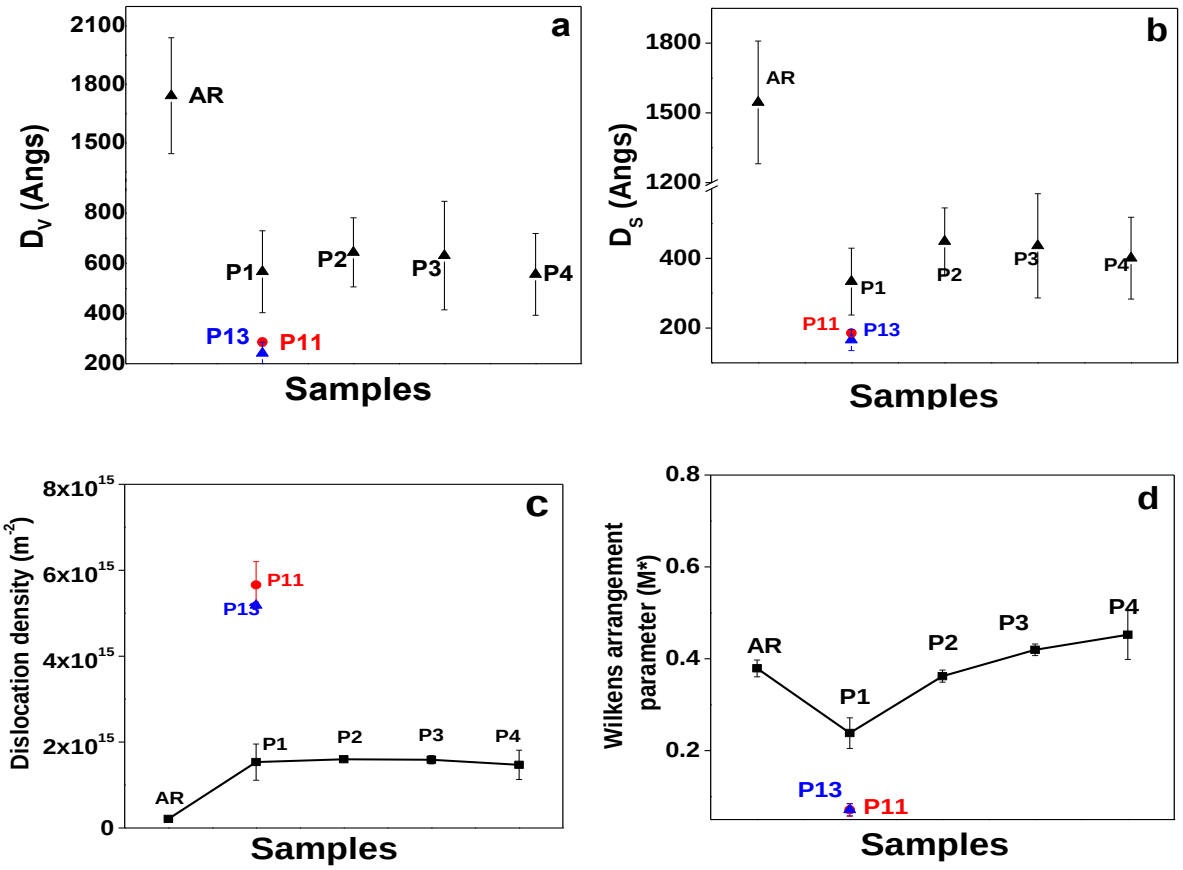

Fig. 4.11: (a) Volume weighted domain size (D_V) (b) Surface weighted domain size (D_S) (c) Dislocation density and (d) Wilkens arrangement parameter (M*) for different deformed samples calculated by CMWP analysis

The important parameters such as the domain size (D_V), microstrain (D_S), the dislocation density and dislocation arrangement parameter (M*) of the austenite phase obtained (using Eq. 2.18) from the CMWP analysis are plotted in Fig. 4.11. It is clearly evident from the Fig. 4.11(a) and 4.11(b) that the domain size (both volume weighted and

surface weighted) variation follows a similar trend as observed in Fig. 4.5(a) which is the result of MAUD analysis. It can also be observed that the dislocation density (In Fig. 4.11(c)) of all the pre-strained samples are almost similar which is concurrent with the results of the microstrain values shown in Fig. 4.5(b) and the dislocation density of the fractured samples P11 and P13 are higher than the pre-strained samples, which is also similar to the earlier results (Fig. 4.5(b)) where the microstrain is higher. However, the arrangement of the dislocations in the pre-strained and the fractured samples are drastically different, which is evident from the Wilken's arrangement parameter M* obtained from the CMWP analysis (plotted in Fig. 4.11(d)). As pointed out by Gubicza [42] a decrease in the value of M* clearly indicates the highly correlated nature of the dislocations which is expected in the fractured sample. Among the pre-strained sample, P1 sample shows a lower M* value compared to the other samples (P2-P4) which is also an indication that the arrangement of the dislocations in the P1 is different from that of the other pre-strained sample.

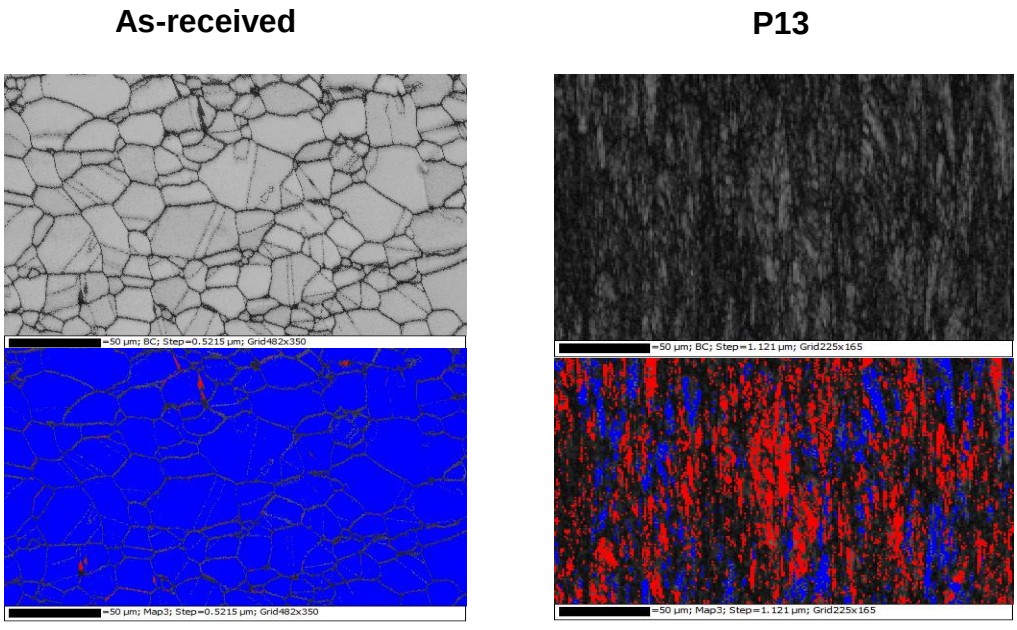

Fig. 4.12: Band contrast and Phase contrast images for as-received and deformed sample

In order to gain insight into the differences in the local microstructure of the austenite and the martensite phase we have carried out detailed EBSD measurements on various deformed samples. The advantage of the EBSD measurement is that one can map the two crystallographic phases in the sample in detail and use the data to obtain comprehensive understanding of the interface of the two phases. EBSD measurements were carried out on only a few selective samples (as-received, P1-P4, P11 and P13). Band contrast images and the phase contrast images of the as-received and P13 sample is shown in Fig. 4.12.

Prominent grains are visible in the band contrast image of the as-received sample. On the contrary, no clear grain structure is seen in the deformed sample and there is a clear increase in the number of non-indexed points (black colour) in the band contrast image. The phase contrast image of the as-received sample reveals the presence of austenitic phase (marked as blue) and small fraction of the martensite phase (marked as red). The increase in the martensite phase is clear in the phase contrast images of the P13 sample. In order to understand the subtle difference between the samples, the phase boundary between the austenite and the martensite phase has been analyzed in terms of the lattice correlation boundaries (LCB) and the orientation relationship boundaries (ORB) between the two phases. The first quantity i.e., the "lattice correlation boundaries" is the measurement of the angular relationship between any two crystallographic planes (or directions) of the two phases. Since, only the planes are considered, and no specific direction within the planes is specified, the LCB values give only a partial relationship between the phases. Orientation relationship boundaries (ORB) are more detailed and give the angular relationship between specific slip planes of the two different phases. The LCB and ORB distribution of the interfaces boundaries of the austenite and martensite has been calculated. LCB angular distribution was calculated considering the highest dense planes ({111} set of planes for fcc structure and {110} for bcc structure) of the two different phases, while the ORB distribution was

calculated using the two primary slip systems of the phases i.e., {111}<110> for austenite and {110}<111> for martensite phase.

There are extensive studies on the crystallography of austenite-martensite transformations and different crystallographic orientation relationships for the transformation of austenite into martensite using Transmission Electron Microscopy [118–123]. Due to the small angular difference between the different orientation relationships the experimental verification of the relationships become difficult and there is still considerable debate on the relative importance of each of them [124]. The fcc-bcc transformations in steels are commonly found to follow the Kurdjumov–Sachs (KS) [125] and the Nishiyama–Wassermann (NW) [118,123] relationships. In both these relationships, the closed packed planes of the two crystallographic phases are parallel or nearly parallel (i.e., $\{111\}_\gamma$ in fcc ‖ $\{110\}_\alpha$ in bcc). They differ in only the slip directions considered within these planes, i.e., KS relationship assumes $<110>_\gamma$ ‖ $<111>_\alpha$ whereas the NW relationship assumes $<110>_\gamma$ ‖ $<100>_\alpha$ [126]. These two relationships differ only by an angular rotation of 5.26 deg [126].

In the present study we have carried out the LCB and the ORB distribution analysis from the EBSD measurements. Since the EBSD data is gathered over a large area compared to that of the TEM data, the analysis provides statistically average information of the boundary characteristics compared to that from the TEM data. The analysis has been carried out assuming that all the boundaries between the austenite and the martensite phase follow the KS relationship only. If the interface boundaries follow the KS relationship ideally, the LCB and the ORB distribution should peak at 0 deg. However, it is observed that most of the boundaries formed show a deviation from the ideal value and are spread up to a maximum of 7-10 deg [127]. In our analysis, we have tried to associate this deviation from the ideal relationship to the differences in the martensite percentages observed among the samples.

Crystallographically the maximum possible angular deviation that can be expected from the KS relationship is 43 deg [127].

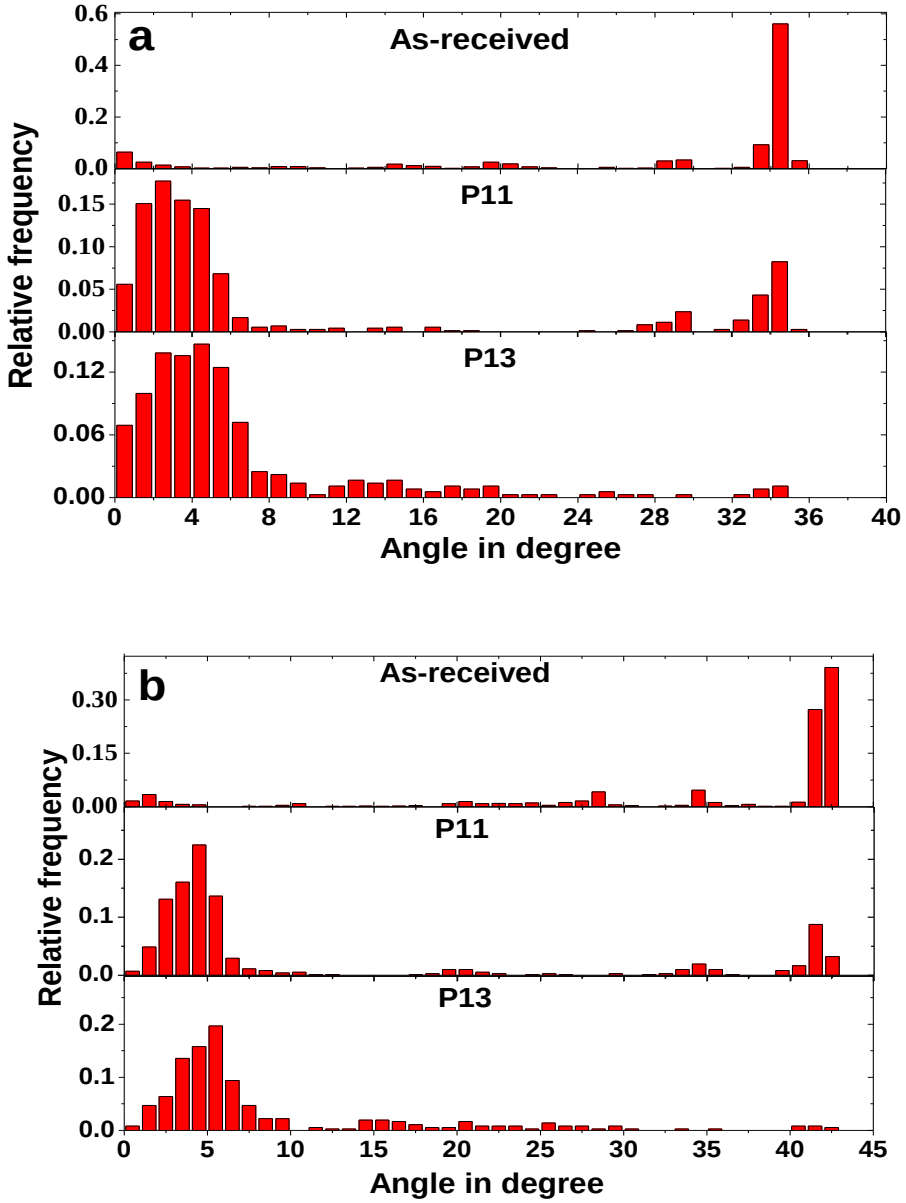

Fig. 4.13: (a) Lattice Correlation Boundaries and (b)Orientation Relationship Boundaries distributions for As-received and two fracture samples

Fig. 4.13(a) and 4.13(b) shows the LCB and the ORB distributions for the as-received and the two fractured samples of the P1 series (P11 and P13). The LCB distribution (Fig. 4.13(a)) of the fractured samples P11 and P13 show large distribution of boundaries at low

angle (2-7 deg) as compared to as-received sample, where most of the boundaries seem to occur near an angle of ~35 deg. This indicates that the boundaries between the austenite and deformation induced martensite phases follows the KS criteria. Similarly, from Fig. 4.13(b) one can clearly observe that the ORB distribution for the as-received sample peaks near the angle of ~42 deg, whereas in P11 and P13 the distribution is maximum at low angle (2-10 degrees) indicating that the boundaries of the fcc and bcc phases have already aligned as per the KS relationship. However, the subtle difference between the P11 and P13 samples can be inferred from these graphs. The LCB and the ORB boundaries in the P13 samples mostly have their angle of deviation concentrated at the lower angles indicating that the there is almost perfect alignment of the two major slip planes in the fcc and bcc lattices following the KS relationship. However, for the P11 samples although majority of the boundaries are almost closely aligned (angle of deviation between 2-7 deg), some of the boundaries still show a larger deviation (angle close to ~35 deg).

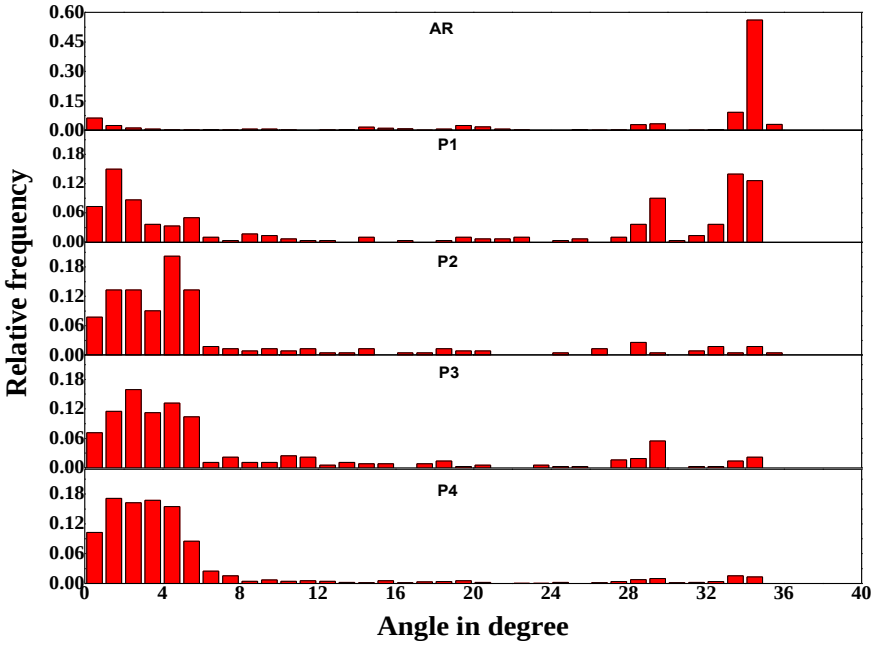

Fig. 4.14: Lattice Correlation Boundaries distribution for all the pre-strain samples (P1-P4)

From the results of the detailed XRDLPA analysis which showed a small difference between P1 and the other pre-strained samples (P2, P3 and P4), we have analyzed the EBSD data of the corresponding samples. The angular distribution of LCB and ORB of the four pre-strain samples (P1-P4) has been evaluated and are shown in Fig. 4.14 and Fig. 4.15 respectively. The difference is clearly noticeable in these figures. The LCB distribution (Fig.4.14) has a peak between 0-5 degrees for all the pre-strain samples except P1, where there is a bi-modal distribution with one peak between 0-5 degrees and other between 30-35

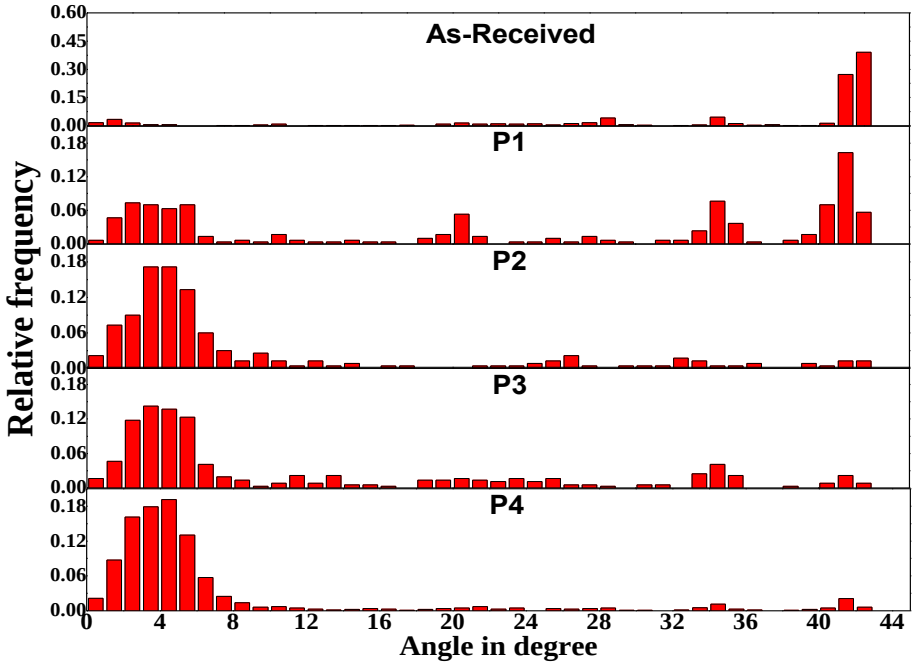

Fig. 4.15: Orientation Relationship Boundaries distribution for all the pre-strain samples (P1-P4)

degrees. This bi-modal nature is also seen the ORB distribution of P1 as seen in Fig. 4.15. Thus, this observation shows that in all pre-strain samples, highest dense plane and the dominant slip systems of the parent fcc phase and the deformation induced bcc phase are aligned almost parallel to each other (again satisfying the KS relationship) except for the P1.The presence of considerable amount of non-parallel primary slip systems of the two phases indicates that a large strain is present in the phase boundaries of the P1 sample as

compared to the other pre-strained samples. This was evident from the microstrain values obtained from the XRD analysis of the austenite and the martensite phases in the pre-strained samples (See Fig. 4.5 and 4.6). The microstrain of the austenite phase in P1 sample is lower compared to that of the other pre-strained sample, whereas that of the martensite phase of P1 is considerably higher than that of other pre-strained samples. It can thus be conjectured that the presence of high strain regions act as high energy site for the further growth or nucleation of new martensite upon further deformation of the P1 sample. Hence it can be conjectured that the pre-strained sample P1 may have the possibility of showing more martensite phase as has been observed compared to other pre-strain samples.

DSC measurements were carried out on some of the samples in order to give supplementary support to the quantification of the martensite formation in this study. Fig. 4.16 shows the thermograms of the as-received, P1, P11, P13 and P03 samples. The endothermic peak observed between 750 K and 950 K in the P11, P13 and P03 samples

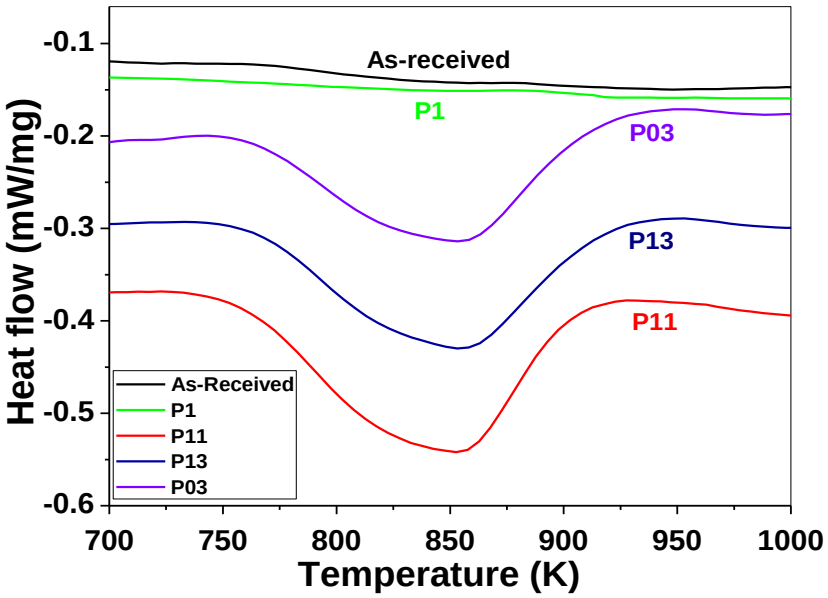

Fig. 4.16: DSC thermograms of As-received and deformed samples

corresponds to the reverse transformation of the martensite phase to the austenite phase [128]. Hence the area under the curve corresponding to the energy absorbed during the transformation is related to the amount of martensite present in the sample. Table 4.1 shows the area under the endothermic peak (energy absorbed) obtained for these samples. The results clearly corroborate with the results of XRD and VSM measurements, where P11 shows a greater martensite (greater energy absorbed) compared to P13 and P03 which shows almost similar amount of martensite phase (corresponding to similar absorbed energy).

The overall important experimental observations can be summarized as follows-

1. The formation of deformation induced martensite in SS304 is sensitive to the path in which the deformation is carried out.

2. A unique combination of pre-strain, pre-strain rate and post-strain rate seems to yield a relatively large amount of martensite within the range of experimental parameters addressed in this study.

3. The LCB and the ORB relationships obtained from the EBSD measurements have helped to identify the differences among the pre-strained samples.

4. Among all the combinations of experimental parameters used in this work, it is observed that pre-strain value of 0.4 carried out with a strain-rate of 10^{-1}/sec and a post-strain rate $\leq 5 \times 10^{-4}$/sec seems to yield the maximum martensite formation (P11 and P12 samples).

5. XRDLPA analysis of the pre-strained samples clearly indicates that the P1 sample with a pre-strain of 0.4 deformed with a strain rate of 10^{-1}/sec has different microstructural parameters compared to the other three. The microstrain of the austenite phase is lower and that of the martensite phase higher in this sample compared to others. The nature of the

dislocations represented by q indicates that the dislocations in P1 have more screw character and the Wilken's arrangement parameter indicates that the dislocations are more correlated in P1 compared to the other three pre-strained samples (P2-P4).

The above results can be explained by the mechanism of deformation induced martensitic formation as a nucleation and growth process.

It is well known that the austenitic-martensitic transformation is accomplished by the nucleation of the martensite phase and subsequently its growth [102]. Extensive research on the MT has led to the general consensus that there are mainly two routes for the formation of the martensite phase, i.e., (1) direct transformation of austenite (γ) to martensite (α') and (2) transformation of austenite (γ) to martensite (α') through the martensite ε-hcp phase [129]. However, it is now accepted that the intermediate ε-hcp is a transient phase [130] and is not an essential precursor for α' [131].

SS304 falls under the category of low stacking fault energy material. When the samples are deformed at a high strain rate, the formation of large number of shear bands is imminent along with increasing probability of intersection of these shear bands. This results in martensite formation both in the intersecting points of shear bands as well as in individual shear bands as also observed by Ye Tian *et.al.* [132]. When this pre-strained sample is again subjected to deformation, the pre-existing nuclei will act as the preferred growth points for the martensite phase. Moreover, new nucleating sites are also formed during deformation. The preferred mode of martensite formation is a competitive process. It depends on whether the growth of pre-existing nuclei is energetically favourable or nucleations of new sites are favourable. The preference for growth to occur from the pre-existing sites is dependent on the energy of the martensite nuclei. It was seen that the microstrain of the martensite phase of the P1 sample is higher compared to that of the

other pre-strained samples and the dislocation arrangement parameter (Fig. 4.10(d)) which is a measure of the interaction/correlation among the dislocations shows a sudden decrease in P1. These may imply that P1 has higher stored energy in comparison to the other pre-strained samples. It was also observed that the LCB and ORB in P1 sample (indicating slip plane alignment between the austenite and the martensite phase) have high angular deviations indicating that these boundaries are in a higher energy state compared to that of P2, P3 and P4 samples. Hence upon further deformation, the growth of the martensite phase in the P1 sample is likely to occur from the pre-existing nuclei as the process is energetically favourable. The lower microstrain of the martensite phase in P2, P3 and P4 samples indicate that upon deformation the growth of the martensite can occur either from new nuclei or will require larger strain to initiate the growth during post-strain.

Recently, Tao-Ho Lee *et.al.* have shown that the screw component of a perfect dislocation plays a crucial role in the γ-fccto ε-hcp martensite transformation [133]. They could categorically demonstrate that the screw component of the dislocation induces a torsional flow of atomic planes resulting in the nucleation of hcp martensite [133]. In our XRDLPA study, we have observed that P1 sample shows an increase in the screw character of the dislocations (Fig. 4.10). It can be conjectured that this increase may be an indication of the precursor for ε-hcp formation in this sample compared to the other pre-strained samples. Hence the observation that P1 pre-strained sample alone shows a large increase the martensite percentage during post strain could be due to the presence of large high energy nucleation sites as well as for the formation of ε-hcp in this sample.

Another important observation is that among all the P1 series samples, only those with low post-strain rate (i.e.,P11 & P12) showed a large increase in the martensite percentage, whereas P13 sample which had the same pre-strain rate but a higher post-strain

rate did not show the increase in the martensite percentage. The difference between P11/P12 and P13 samples is seen in the LCB and ORB distributions as observed in Fig. 4.13(a) and 4.13(b) respectively. It is clear that P11 still shows presence of γ–α'boundaries with large angular deviations as compared to the P13. The martensite phase present in the P1 sample having both low and high angle boundaries have grown during the post straining in the P11 sample compared to the P13 sample. On the other hand, P13 sample shows the growth of only the low angle boundaries. In earlier works, it was observed that the high density of pre-existing dislocations in the austenite increased the resistance to the martensite growth by obstructing the cooperative atomic displacement [134,135]. It was conjectured that the presence of entangled dislocations may pin or slow down the growth of the phase boundary [134,135]. Hence in the P13 sample where the post-strain rate is larger compared to P11 and P12, it is expected that the dislocations formed during the deformation are entangled and hence prevents the growth of the high angle deviated boundaries.

It can be summarized that the volume of the martensite formed during deformation can be controlled by adjusting the pre-strain and also the pre-strain rate and post-strain rate. These aspects have high importance while determining the process parameters in shop floor practices such as ausforming etc. where the increase in the number of nucleating sites as well as refining the martensite plate size is the major criteria of the process. This combination of the pre-strain and pre and post-strain rate may be highly sample dependent and each alloy combination may require a unique combination of these experimental parameters to arrive at a higher martensite percentage.

4.6. Conclusion:

Tensile coupons of SS304 have been subjected to uniaxial deformation with a combination of different pre-strain and pre/post-strain rates. The quantity of the martensitic phase has been

obtained from the XRDLPA analysis. The relative quantitative phase measurement using VSM (magnetic measurement) and the DSC study has supported the result of XRDLPA analysis. The XRDLPA and VSM measurement have shown a few percentage of martensitic phase has formed in the pre-strained samples indicating starting or nucleation of new phase. All these measurements also show the continuation of the growth of martensitic phase during post strain. We have shown that a specific combination of pre-strain (0.4), pre-strain rate (10^{-1}/sec) and post-strain rates ($1x10^{-4}$ and $5x10^{-4}$/sec) within the experimental parameters used in this work yielded a higher martensite fraction. Significant difference in the microstrain (of both the austenite and martensite phase) and the dislocation character of the austenite phase obtained from the detailed XRDLPA analysis of the pre-strained samples indicate that these samples have the necessary precursors for higher martensite growth during the post-straining stage. Detailed EBSD analysis of the $\gamma-\alpha'$ phase boundary in terms of the KS relationship reveals that these pre-strain samples have shown presence of both low angle and high angle deviated LCB and ORB's which would have acted as the nuclei for the growth of the martensite phase during the post strain. During the post strain, the growth of the martensite is supported only at low strain rates, indicating that the entangled dislocations forming at the high strain rate restrict or slow down the growth of the phase boundary which are mainly high angle deviated LCB and ORB's. Overall observation shows that relatively higher strain rate makes it possible to nucleate martensitic phase at all probable sites and relatively low strain rate helps to grow the high angle deviated nuclei also. Thus this study has clearly shown that for tuning the properties of transformation in induced plastic steels, it is necessary to use a unique combination of process parameters.

Chapter 5

In situ XRD studies of the process dynamics during annealing in cold rolled copper

5.1 Introduction:

Property of a well finished material depends on the thermomechanical processes of which it has been subjected to, before achieving its final useful form. The final mechanical properties of the material such as yield stress, fracture stress and ductility are controlled by the microstructural features such as point defects, dislocations, presence of second phase, grain boundaries, grain size, grain shape, texture *etc.* Hence, control over the microstructure is important to obtain the desired final properties of the material. In order to control, improve and optimise the microstructure i.e. grain size, grain shape and texture of the final finished product, a detailed understanding of the physical insight underlying the deformation and annealing phenomena is essential [1]. This requires collecting quantitative information regarding the detailed microstructural evolution during the thermomechanical process.

Rolling is a biaxial deformation process during which both compressive and longitudinal stresses are applied to the material. In this deformation process, the mobile dislocations accommodate the strain produced due to the increase in defect densities inside the material which changes the morphology of the internal grain structure of the materials. These dislocations are then accommodated in the form of various microstructural features (such as cells, domains, sub-grains *etc*.) inside the grains that are characteristics of the

deformed state [136]. The shape of the grain changes with the formation of new grain boundary area by incorporation of a large number of dislocations generated during this process. These external and internal changes in grain structure results in changes in the stored energy of the material. Stored energy of any cold work material represents the elastic energy associated with the defects [137,138]. The sum of stored energies accommodated in isolated defects, grain boundaries and the interfaces of the domains within the grains represents the total stored energy of the deformed material [1]. It may be noted that the amount of stored energy in deformed material not only depends on total dislocation density, but also on the configuration of dislocations [137] which is dictated by the dislocation stress field [139,140]. Dislocation configurations with long range stress fields have higher stored energy compared to the arrangement where the dislocation screening is enhanced [137]. In addition to that the orientation of the grain determines the slip activity (by the orientation relationship of the slip system) which controls the deformation process in the material [141–146]. Therefore, in a polycrystalline material, the overall stored energy during deformation is highly related to direction of applied stress and grain orientation (texture). The stored energy will thus vary from grain to grain depending on its local crystallographic orientation [147,148].

For deformed samples, this stored energy will acts as a driving force for recovery and recrystallization of the material during annealing [138]. The onset of recovery and the completion of recrystallization of a material depend on the amount of stored energy. The higher the stored energy, the faster the material will recover and pave way for formation of new nucleating sites or defect free grains. Thus, different crystallographic orientations will show different time dependence of the release of stored energy during annealing due to the different dislocation movement dynamics in each plane [142]. Hence, different set of crystallographic planes (hkl) will respond differently to the deformation as well as annealing process in the materials. However, in order to achieve the desired properties at the finished

stage of the materials, estimation of stored energy as a function of time along different crystallographic planes during annealing of a deformed material will have a significant impact on selecting the process parameters particularly annealing temperature and time.

The annealing process involves the decrease in stored energy which corresponds to the change in microstructure due to the rearrangement and annihilation of defects. Since, annealing behaviour of a material is not only dependent on the overall stored energy but also the mobility of defects. Thus, annealing process depends on the spatial distribution of defects *i.e.* the crystallographic plane in which the defects are present [1]. Inhomogeneity of stored energy on a local scale will affect the nucleation, whereas the larger scale heterogeneity will influence the growth of the recrystallized grains [1]. Hence, it is of high importance and significance to study the annealing behaviour of a material with different deformations in the light of accumulation of stored energy and distribution of defects**.** In this work, the detailed evolution of defects have been studied and evaluated the amount of stored energy released at different crystallographic planes during annealing of 50% and 80% cold rolled Cu samples.

5.2 Previous Studies and motivation:

Several studies on deformed Cu have been carried out in detail to understand the annealing phenomenon [149–153]. Ph. Gerber *et al.* [142] carried out studies on evolution of global texture during recrystallization of cold rolled copper after various rolling reductions. G. Mohamed *et al.* [154] investigated intergranular work hardening state in moderately cold rolled copper and found that the stored energy varied substantially with the initial orientation, leading to a strong variation of the recrystallization temperature. The influence of cold deformation on the stored energy in other alloys have also been studied with the help of neutron diffraction and Electron Back Scattered Diffraction (EBSD) [147,155]. D. Breuer *et al.* [156] estimated the density of dislocations and its arrangement in plastically deformed

copper using XRD. T. Rzychon *et al.* [157] determined the changes in microstructure during compression and oscillatory torsion of deformed copper by XRD line broadening. K. Piekos *et al.* [144,158] observed stored energy distribution with respect to crystal orientation in polycrystalline copper experimentally as well as using stochastic vertex model of recrystallization. They observed that the release of the stored energy followed a complicated process and was highly orientation dependent. L. Liu *et al.* [159] has measured stored energy and recrystallization temperature in polycrystalline copper as a function of rolling strain. C. Deng *et al.* [143] have estimated the bulk stored energy of cold rolled tantalum by differential scanning calorimetry (DSC) along with the evolution of microstructure. R. D. Doherty *et al.* [160] described the fundamentals of recrystallization with the understanding of as-deformed state on different metals. D. Mandal *et al.* [153] studied the effect of grain boundaries on the stored energy at different grain size of the cold worked copper. J. Schamp *et al.* [161] concluded that the recrystallization is non-homogeneous across the cross-section of the electrolytic tough pitch (ETP) copper wire by measuring the stored energy using DSC. Other studies [136,162] have also been carried out to assess the static and dynamic stored energy on deformed copper. However, the temporal release of stored energy at various deformations and temperature with respect to different crystallographic planes and also the process dynamics involved in releasing the stored energy have not been studied so far.

5.3 Brief description of the work:

In this work, the microstructural evolution during annealing of deformed electrolytic copper has been followed using in-situ high temperature XRD technique. Detailed XRDLPA analysis of the XRD data of different crystallographic planes of the deformed sample was carried out to follow the temporal evolution at different temperatures. The stored energy has also been estimated from the XRD data using modified Stibitz formula [148,163]. However, this formula is only a first order approximation and the error associated in estimation may be

relatively high [164]. Nevertheless, in view of the fact that the main aim of this work is to understand the dynamics of the release of stored energy along different crystallographic planes with respect to temperatures, although the absolute value of the stored energy is not necessarily important. The overall stored energy of the samples has also been measured by DSC at different deformations to corroborate with the estimation by XRD. It is to be mentioned that the other important consequences of deformation and/or annealing such as orientation of individual grains or texture has also been partly addressed. Here, 50% and 80% cold rolled deformed samples were chosen for carrying out the study of the release of stored energy using the X-ray diffraction technique. The higher percentage of deformation offers the advantage of substantially higher initial stored energy (hence higher peak broadening). Hence the temporal release of stored energy at higher deformations and temperatures can be followed in the lab time scale and the corresponding higher peak broadening in XRD data can be clearly analysed to follow the evolution as a function of time. Though the 90% cold rolled specimen is the highest deformed among all, it was not considered because the sample was quite thin (0.5 mm) to handle for EBSD sample preparation which involves grinding, polishing and etching. The intermediate deformation percentages (60% and 70%) were not chosen because, a large difference in the initial stored energy (i.e., between 50% and 80%) can give rise to clear difference in the time scales of the annealing processes.

5.4 Experimental procedure:

5.4.1 Sample description and preparation:

In this study, electrolytic copper was used and its composition is given in Table 5.1. The electrolytic copper sheet was cold rolled from 20% to 90% at room temperature. The as-received copper sheets (thickness 5 mm) were rolled and samples with different reduction (from 20% to 90% -except 30%) were obtained in this study. Each 10% reduction was achieved by the same ten number of passes. During the deformation process, no thermal

annealing was carried out in between the different percentage reduction. This ensured that the deformation was a cumulative process. Small samples were prepared by procedure detailed in section 2.2.2, Chapter 2.These as-deformed samples were then systematically characterised using optical microscopy and X-ray diffraction.

Table 5.1: Composition of the Copper sample

Element	O	Ag	S	Fe	Ni	Sn	As	Pb	Sb	Cu
Amount in ppm	270	25	14	10	8	5	4	3	3	Bal.

5.4.2 Optical Microscopy:

Initial characterisation of the as-received and the deformed samples have been carried out using optical microscopy. The polished samples were chemically etched using Ferrous-chloride solution and the microstructure was observed using Carl Zeiss, Inverted Optical Microscope. In order to observe the changes due to annealing, the optical micrograph of the annealed samples was also observed after proper sample preparation.

5.4.3 X-ray diffraction measurements:

X-ray diffraction (XRD) profiles from as-received and all deformed samples were recorded using Bruker D8 Advance X-ray diffractometer using Cu K_α radiation. The data was collected in the 2θ range of 40° to 100° with a step size of 0.02° using the room temperature stage. The collection time given for each step was 1 sec/step for full profile scan at room temperature and 0.5 sec/step for single peak scan during high temperature dynamics study. The instrumental broadening was corrected by using the XRD data obtained from Si powder (NIST standard SRM 640) with the same experimental parameters.

The high temperature XRD study was required to carry out in-situ measurement at different temperatures and different crystallographic planes to understand the defect evolution as a function of time in the deformed samples. In order to identify the suitable temperatures

for this in-situ XRD study, an ex-situ experiment was carried out. Samples of 80% deformed sheet were soaked in a (temperatures 400 K, 414K, 441K and 471K) Silicone oil bath for 15 minutes which was preheated using a magnetic stirrer attached with thermostat. The samples were then characterized using X-ray diffraction using the same experimental parameters as mentioned earlier.

For the in-situ studies, small samples of 50% and 80% rolled copper sheet were polished carefully and mounted on the high temperature XRD stage consisting of a Platinum (Pt) strip heater using small amount of thermally conducting silver paste. The sample used in the high temperature XRD stage were thinned down to less than 0.2 mm to satisfy the focussing condition of the Brag-Brentano geometry. The whole stage was evacuated and the vacuum was maintained better than 5×10^{-5} mbar during the experiment so that the sample did not oxidise. Time dependent annealing study was carried out at three different temperatures (458K, 473K and 488K chosen from the initial ex-situ study). Samples were heated at a rate of 2 K/sec, up to the desired temperature and then the X-ray scan of any one crystallographic peak (e.g. {111}, {200} and {220} etc.) was taken as a function of time. In all cases, a freshly-prepared sample was taken from the rolled sheet to collect the data for a particular {hkl} plane and also for different temperatures. The data collection time of each {hkl} plane was chosen after optimizing the peak to background ratio for obtaining an acceptable peak. The 2θ range for the scans was also determined such that the desired amount of background points is available on either side of the peak to carry out further XRDLPA analysis. Each peak evolution was followed up to a time till no change in the integral breadth of the peak is observed for a few successive peak profile measurements. This indicated that the microstructural evolution (as observed by XRD) has reached its saturation for this particular temperature. The time coordinate was calculated from the time stamps at the beginning and end of each scan provided along with the data saved after each scan by the XRD data

collection program. The actual time corresponding to each scan is calculated as follows: After mounting the sample, the temperature was set using the programmable Eurotherm controller provided with the XRD high temperature stage. When the set value is reached, the XRD instrument starts collecting the data and the time is designated as t_i (which includes the time for the source and the detector to move to the required θ_1 angle). If the time taken for scanning the particular peak is taken as $\delta t = t(\theta_2) - t(\theta_1)$, then the time of each scan is calculated as $t_n = t_i + (n-0.5)* \delta t$.

5.4.4 Electron backscatter diffraction (EBSD):

Electron microscopy studies were also carried out for more detailed understanding of the microstructural changes among the deformed and annealed samples, using FESEM (Carl Zeiss Supra 55). Electron Back Scattered Patterns (EBSP) was captured with a beam voltage of 20 kV, step size of 0.3 μm, at a working distance of 16 mm and a 70° tilt angle of the sample. The polished surface was electrochemically etched by D2 electrolyte (supplied by Struers), to obtain an optimum microstructure with high indexing ratio. In each case, the sample was mounted with the rolling direction parallel to the horizontal direction of the EBSD sample mount. Use of electrochemically etched sample ensured that the optimum microstructure could be obtained with high indexing ratio.

5.4.5 Differential scanning calorimetry (DSC):

The overall stored energy of the deformed samples was measured on both the 50% and 80% rolled samples using DSC/TGA attachment of the Simultaneous Thermal Analyser (Netzsch STA 449F1) to compare with the measured stored energy using XRD. Small pieces (~ 60-80 mg) of the deformed samples from the rolled sheets were used for this study. The experiment was carried out at a heating rate of 40K/min on both the samples up to 873K. Two consecutive runs were carried at the same heating rate for calculation of the quantitative

stored energy. Ultra-high pure argon gas (5N purity) was used to protect the sample against oxidation during the entire experiment.

5.5 Results and Discussion:

The results were divided into two parts (deformation and annealing) as described below-

5.5.1 Deformation Study:

Deformation causes the microstructural changes in various ways where the shape of the grain changes depending on the direction of deformation and this leads to a large increase in the total grain boundary area [1]. For cubic metals, the main mechanism of deformation is slipping and twinning. The slipping mechanism is mostly predominant for the metals with high stacking fault energy [23]. Though copper has stacking fault energy of 78 mJ m^{-2} [23], it is still considered to be moderately high [165] and the mechanism of deformation of Cu is primarily by slip followed by twinning. The essential difference between the deformed and the annealed states lies in the dislocation content and their arrangement. It is well understood that the evolution of the microstructure during recovery and recrystallization is determined by the deformation microstructure based on the density, distribution and arrangement of the dislocations [1]. Hence, it is of utmost importance to study the microstructure (grain size and shapes, domains size (the coherent size of the crystal determines by the dislocation cells within the cell blocks), micro-strain inside the domain), stored energy along different crystallographic planes and also the overall stored energy in the deformed material. In this study, the deformed samples were characterised using various techniques to understand the dislocation and its arrangement and its manifestation in the different length scales.

(a) Micro-graphical study:

The grain morphology of as-received and deformed samples was characterised by optical microscopy as well as with the help of FESEM using the EBSD technique. Fig. 5.1 represents

the optical micrographs of as-received, 50%, 60%, 70% and 80% rolled samples. All the rolled samples clearly reveal the effect of deformation on the grain morphology. The as-

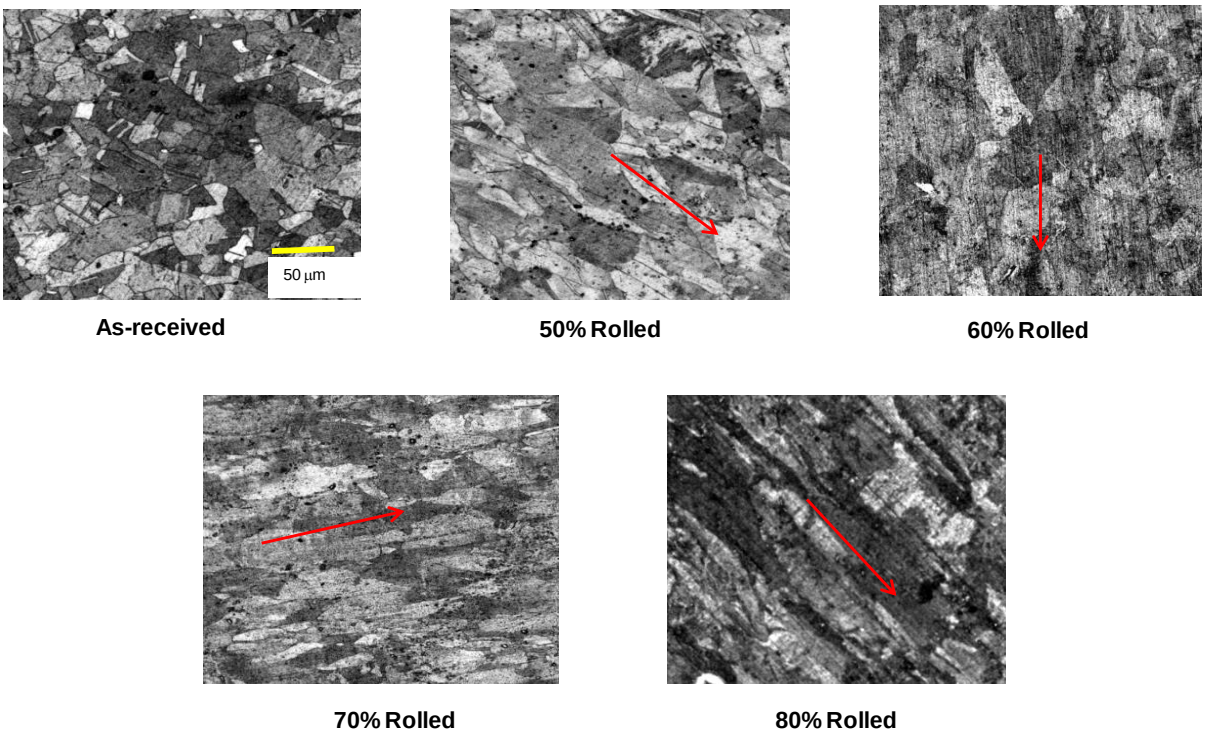

Fig. 5.1: Optical Micrographs of As received and rolled copper samples (50%, 60%, 70% and 80% rolled samples)

received sample shows clear well-defined grains with an average grain size of about 30 µm. During the deformation process, grains are becoming elongated along the rolling direction. The figure clearly shows the ductile nature of the Cu sample in which higher the deformation, larger the elongation of the grains (The red arrows in the optical micrograph shows the rolling direction and the elongation is also along the same direction as expected)

The deformation microstructure is more clearly evident in the EBSD micrographs as shown in Fig. 5.2(a), 5.2(b) and 5.2(c) for as-received, 50% and 80% rolled samples respectively. The 50% rolled sample shows a smaller grain size with irregular grain boundaries whereas, the 80% rolled sample clearly shows the elongated structure with highly

irregular boundaries. The small angle grain boundaries have been generated using the EBSP with a minimum and maximum misorientation angle of 2 deg and 15 deg respectively.

Fig. 5.2: EBSD Band contrast image of (a) As-Received, (b) 50% rolled and (c) 80% rolled sample

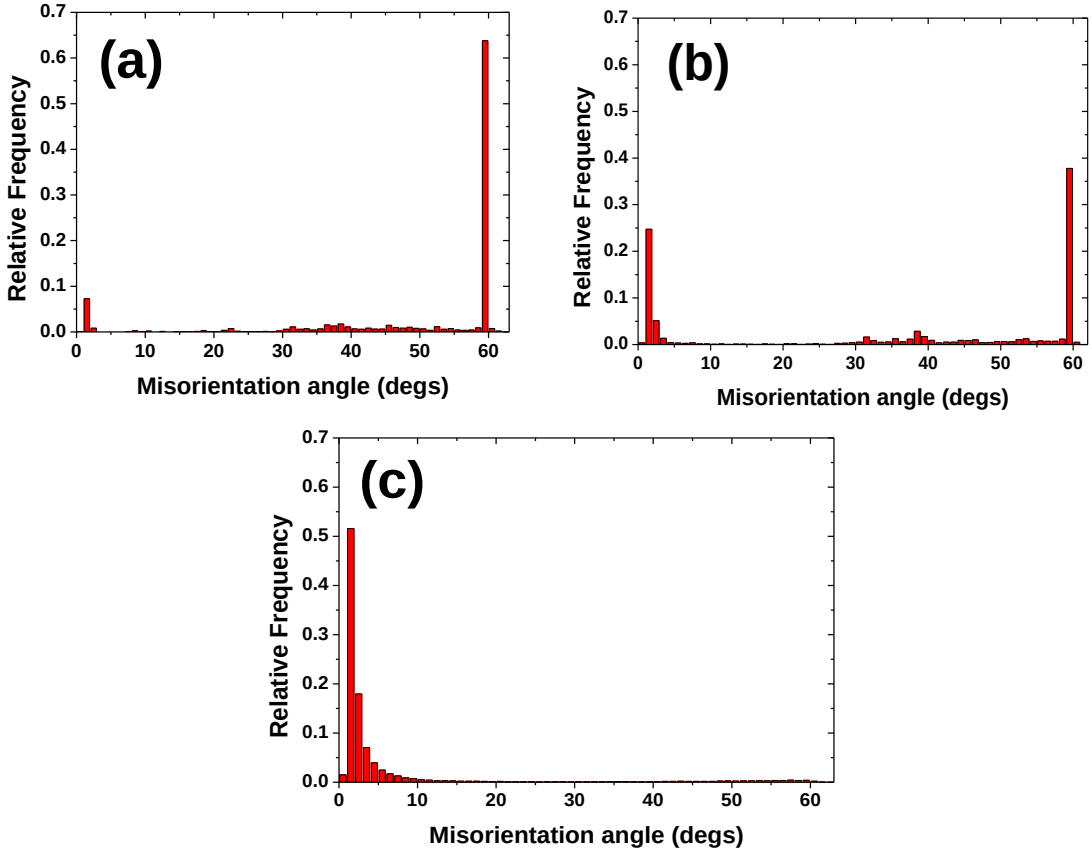

Fig. 5.3: Relative frequency distribution of misorientation angles of (a) As-Received, (b) 50% rolled and (c) 80% rolled sample

Using the HKL Channel 5 software, the relative frequency distribution of the misorientation angle between two consecutive EBSP has been evaluated for as-received, 50% rolled and 80% rolled samples and presented in Fig. 5.3. The EBSD micrograph and relative frequency distribution of misorientation angle of the 80% rolled sample (Fig. 5.2(c) & 5.3(c)) reveals a significantly larger fraction of low misorientation angles as compared to 50% rolled sample (Fig. 5.2(b) and 5.3(b)). Another parameter that can be used to understand the effect of deformation is the band contrast (BC) of the EBSP [166]. It is a quality factor derived from the Hough transform that describes the average intensity of the Kikuchi bands with respect to the overall average intensity within the EBSP [165].

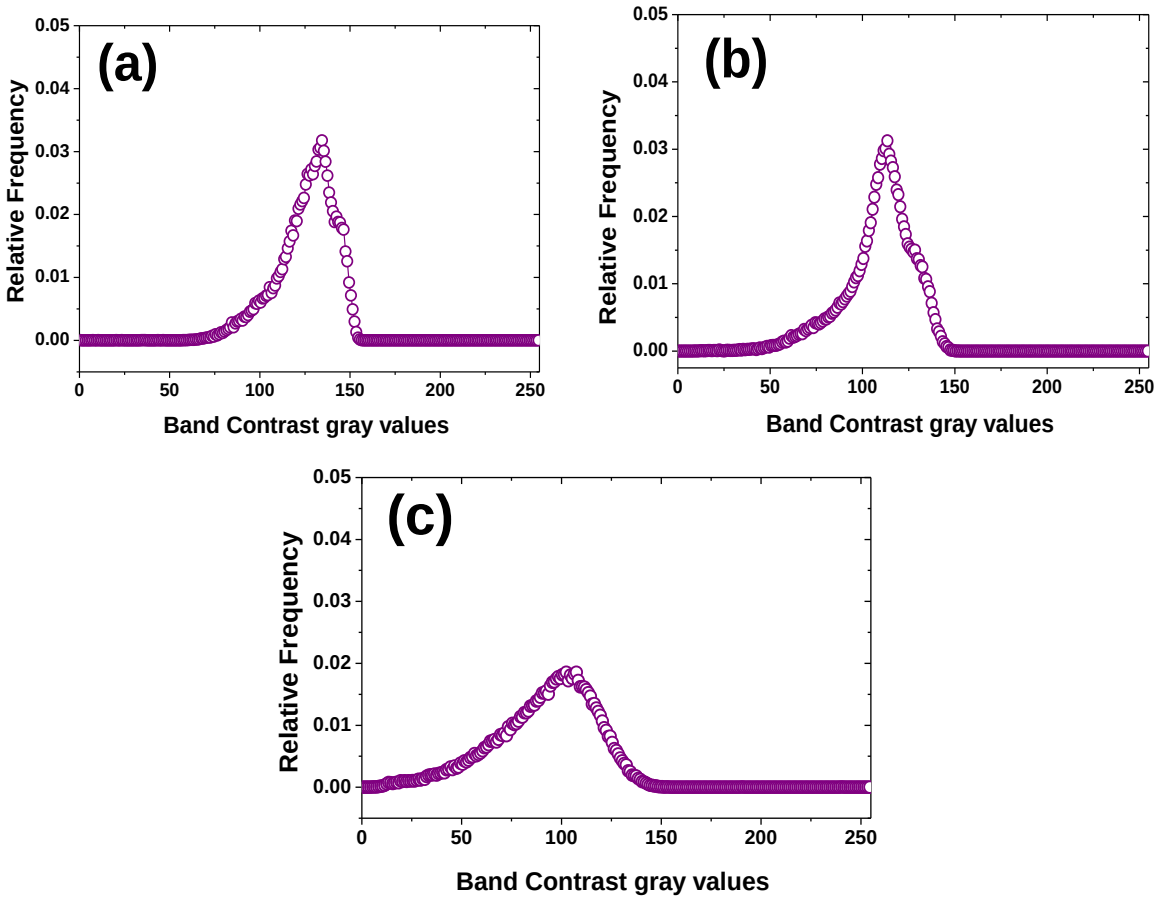

Fig. 5.4: Relative frequency distribution of band contrast of (a) As-Received, (b) 50% rolled and (c) 80% rolled sample

The values are scaled to a range from 0 to 255 (low to high contrast). In general, the grain boundaries and deformed regions tend to be darker than the interior of the well recrystallized grains [18]. Similar parameters (such as pattern quality, image quality etc.) defining the quality of the Kikuchi pattern generated in an EBSD have been used recently to understand a qualitative difference in the microstructure in the deformed, recovered and recrystallized stages of a sample [18,155,166,167]. The histogram of the BC values obtained in the three samples are shown in Fig. 5.4(a), 5.4(b) and 5.4(c) respectively and it can be clearly seen that the histogram becomes broader and the peak gradually shifts to a lower gray value with increasing deformation.

(b) X-ray diffraction studies:

The X-ray diffraction pattern of the as received and the deformed samples are shown in Fig. 5.5. It is clearly observed that there is a systematic increase in the intensity of the {220} peak and a decrease in the {111} peak in the rolled samples respectively compared to the as

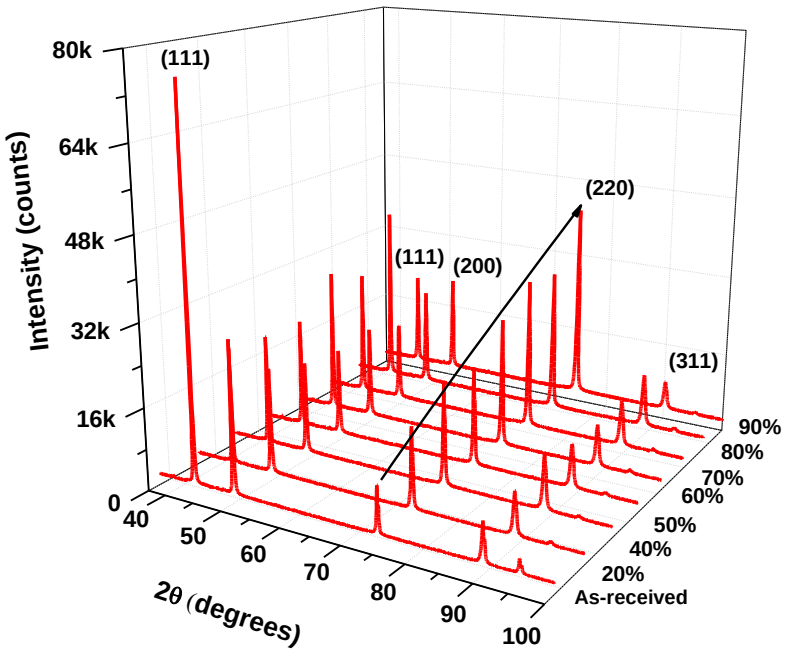

Fig. 5.5: X-ray diffraction patterns of all the rolled samples with as-received sample

received sample. A significant broadening of the diffraction peaks of the deformed samples is also observed indicating that the deformation has introduced changes in the internal structure within the grains causing the formation of substructure (domains) inside the grains and the micro-strain inside the domains [1]. During cold rolling, a large number of dislocations are introduced in the material but these may not be randomly distributed in the material. These dislocations are accommodated into the material in a variety of ways including creation of internal boundaries. In order to decrease internal energy, the individual dislocations arrange themselves creating substructures within the grains. It is seen that in case of copper rolled to low strains, the microstructure consists mainly of cells or domains (tangle of dislocations) and also thin plate like micro bands [1,165].

To get a qualitative idea of the texture evolution, a relatively old method using the relative intensity ratios of the different crystallographic planes has been used. In this method the relative intensity ratio of each {h'k'l'} plane of the deformed sheet was calculated using the following equation -

$$(I_R)_{h'k'l'}=(I_{h'k'l'}/I_{hkl})/\sum(I_{h'k'l'}/I_{hkl}) \qquad \textbf{(5.1)}$$

Where, the unprimed and primed indices indicate corresponding Bragg reflections of the as-received and the deformed samples. The relative intensity ratio of each {hkl} plane has been

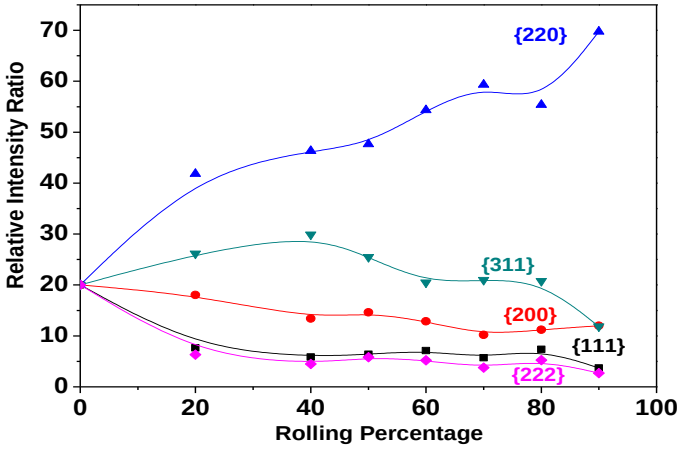

Fig. 5.6: Relative Intensity Ratio for different {hkl} Planes

plotted with respect to rolling percentages (as shown in Fig. 5.6). This plot clearly reveals the preferred orientation of {220} crystallographic plane (parallel plane to {110} set of planes). This type of texture formation is generally observed when the compressive stress is dominating over the tensile stress during the rolling process.

In a rolling process, the sample is subjected to biaxial stress i.e. (i) tensile stress along the rolling direction and (ii) compressional stress in the direction normal to the rolling plane as shown in the Fig. 5.7(a) and 5.7(b). The thickness reduction during each pass determines the compressional stress and the rolling speed determines the tensile stress. Type of texture formation during rolling depends on which among the two stresses (compressional or tensile) is dominating during the deformation. In fcc copper, the major slip system is {111}<110> [23]. The increase in the peak intensity of the {220} peak as seen in Fig. 5.5 and 5.6 indicates that the {110} planes are preferentially oriented along the rolling plane during the deformation process. It is well understood that during the rolling process (shows in Fig. 5.7(a)), if the compressive stress is more than the longitudinal stress, then the majority of {220} planes tend to orient along the rolling plane [168]. This is because, the {111}<110> slip system becomes active and tend to align the {111} (as explained in Fig. 5.7(b)) planes

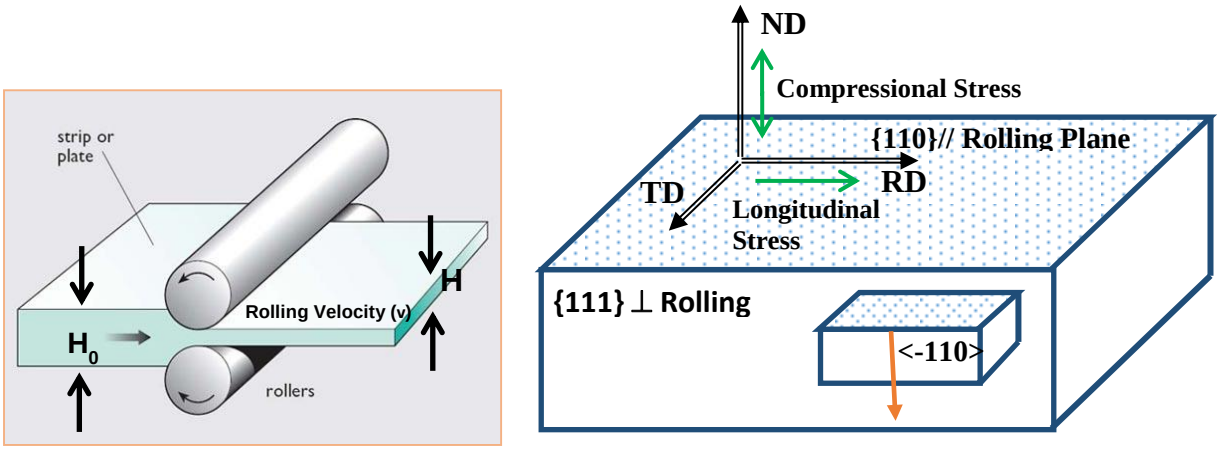

Fig. 5.7: Schematic diagram of (a) Rolling process and (b) {110} texture formation (red arrow showing the slip direction <-110>)

perpendicular to the rolling plane and since <110> is the slip direction, the corresponding {110} planes tend to align parallel to the rolling plane containing the rolling and the transverse directions.

Domain size and microstrain evaluation:

The X-ray diffraction line profile analysis (XRDLPA) was used to evaluate the microstructural parameters such as domains size and micro-strain inside the domains generated due to the deformation inside the materials. This measurement helps to understand more details of the deformation effect on the materials. The surface weighted domain size (D_s) and the average microstrain values $< \varepsilon_L^2 >^{\frac{1}{2}}$ were obtained by the modified Rietveld technique (using LS1 and MAUD) [8,67] which was described in detailed at the chapter 2. The microstructural parameters obtained by this LS1 program for the 50% and 80% rolled samples are shown in Table 5.2. The volume weighted domain size (D_v) along different {hkl} planes was also calculated using Scherrer equation (Eq. 2.2) after the appropriate instrumental broadening correction [57]. The integral breadth (β) was calculated considering that the peak profile follows the Lorentzian function. The peaks could not be fitted with a Gaussian or a pseudo-Voigt function which implies that the strain contribution to the broadening is almost negligible. The values of the corrected D_v are also given in Table 5.2. It is clearly seen from the Table 5.2 that both D_v and D_s decreases with increasing deformation resulting in smaller coherent region or domains, but the values of the microstrain did not change with deformation. Copper being a material with medium stacking fault energy [23,165], the mode of deformation in some grains may be accommodated by two mechanisms namely slipping and twinning. It is also observed that the relative shift in 2θ is not significant in case of both 50% and 80% rolled samples as compared to as-received sample. Hence, it may be possible that the stacking faults are absent even after 80% deformation. With the

increase in strain, the dislocation initially forms the cell structure and subsequently the deformation is accommodated by twinning [1,165] and the amount of which increases with increasing deformation. However, we could not observe any deformation twins in FESEM as these may be extremely fine. Humphrey *et.al.* [1] have reported that the thickness of these twins is in the range of 0.2-0.3 nm which may not be possible to observe in either XRD or in the EBSD measurements.

Table 5.2: Volume weighted domain size D_V (calculated using Scherrer formula) of different {hkl} planes and surface weighted domain size D_S and microstrain ε (calculated by modified Rietveld technique LS1) of the as received and deformed samples.

Sample	Domain size (D_v) of {111} at RT (Å)	Domain size (D_v) of {200} at RT (Å)	Domain size (D_v) of {220} at RT (Å)	Domain size (D_v) of {311} at RT (Å)	Average Domain size (D_s) (Å)	Microstrain (ε)
As received	487.3	274.0	338.6	253.4	----	----
50%rolled	355.3	279.6	269.6	196.3	294	$8.6x10^{-4}$
80%rolled	327.6	213.9	261.5	163.2	245	$8x10^{-4}$

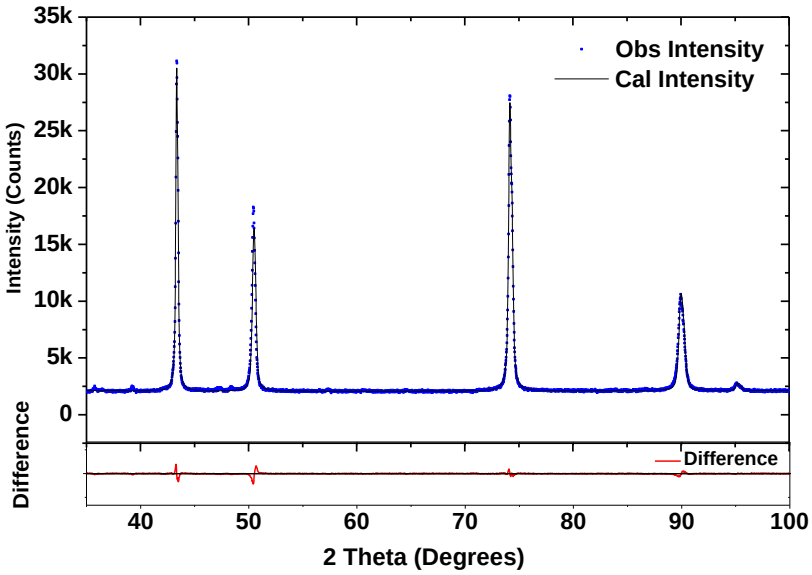

Fig. 5.8: Representative modified Rietveld fitting (by MAUD) of the 80% rolled sample

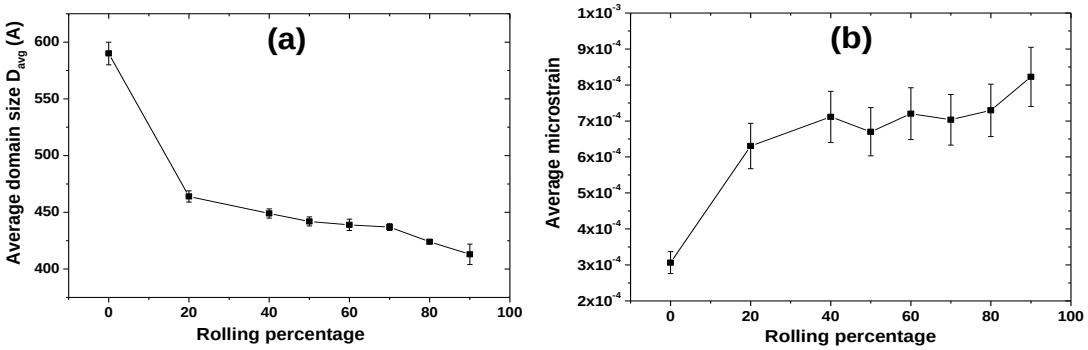

Fig. 5.9: The variation of (a) Average domain size (D_{avg}) and (b) Average microstrain (ε_{avg}) with rolling percentage obtained by MAUD analysis

Detail microstructural analysis was also carried out (using MAUD software) on all the rolled samples. Fig. 5.8 shows a representative MAUD fitting of the 80% rolled sample. Average domain size (D_{avg}) and the average microstrain (ε_{avg}) were calculated after correcting for the anisotropy and the texture as outlined in Chapter 2.

The average domain size and microstrain variation are shown in the Fig. 5.9(a) and 5.9(b) respectively. Domain size is systematically decreasing and the microstrain is increasing with increasing deformation. This indicates that the formation of lower angle misorientation boundaries and increasing lattice strain with increased percentage of rolling.

Calculation of stored energy:

Rajmohan *et.al.* [148] have used a modified Stibitz [163] formula for calculating the stored energy [$E_{<hkl>}$] along different crystallographic orientations [148] using direction dependent elastic modulus [$Y_{<hkl>}$] & Poisson's ratio [$\nu_{<hkl>}$] as given below.

$$E_{<hkl>} = \frac{3}{2} Y_{<hkl>} \frac{\left(\frac{\Delta d}{d}\right)^2}{(1+2\nu_{<hkl>}{}^2)} \quad \textbf{(5.2)}$$

Where, $Y_{<hkl>}$ is the Youngs modulus and $\nu_{<hkl>}$is the Poisson's ratio which are both direction dependent. The relative change in the lattice spacing $\left(\frac{\Delta d}{d}\right)$ can be obtained from the broadening of the X-ray diffraction peaks using the following relation:

$$\left(\frac{\Delta d}{d}\right) = \frac{\beta}{2\tan\theta} \quad \textbf{(5.3)}$$

Where, β is the integral breadth after instrumental broadening correction at the Bragg angle 2θ as explained in the previous section.

The values of the stored energy along the planes {111}, {200}, {220} and {311} have been estimated using the direction dependent $Y_{<hkl>}$and $\nu_{<hkl>}$ and are presented in Table 5.3 as a function of deformation. It is evident from Table 5.3 that the stored energy is highly orientation dependent and the value of stored energy is more in the highest atom density planes (i.e. {111} for fcc materials) as compared to the other planes even in the as-received samples. The stored energy has increased in all the planes with increasing deformation with the change being maximum in the {111} plane. The other planes show a relatively lower increase in the stored energy. {111} crystallographic plane being the slip plane can accommodate more dislocations and hence show a greater increase in stored energy as compared to other planes. It should be noted that the error in full width at half maximum value was high for the peaks with low signal to noise ratio ({311} XRD peak) and also low intensity values.

Table 5.3: Stored Energy of different {hkl} planes of the As-received, 50% and 80% rolled samples

Sample	SE of {111} at RT (J/Mole)	SE of {200} at RT (J/Mole)	SE of {220} at RT (J/Mole)	SE of {311} at RT (J/Mole)
As received	10.48	7.48	5.22	4.79
50% rolled	19.92	7.15	8.09	7.73
80% rolled	23.17	12.24	8.63	11.35

(C) Differential Scanning Calorimetry (DSC):

The stored energy provides the driving force for recovery and recrystallization at the time of annealing [1,163]. Hence it is necessary to quantify the overall stored energy in both the samples which will help to determine the approximate annealing temperature. Fig. 5.10

shows the DSC curves of the 50% and 80% rolled samples heated at a rate of 40K/min after the baseline correction. It is clearly seen that the peaks are obtained at temperature of 592K and 552K for 50% and 80% rolled samples respectively.

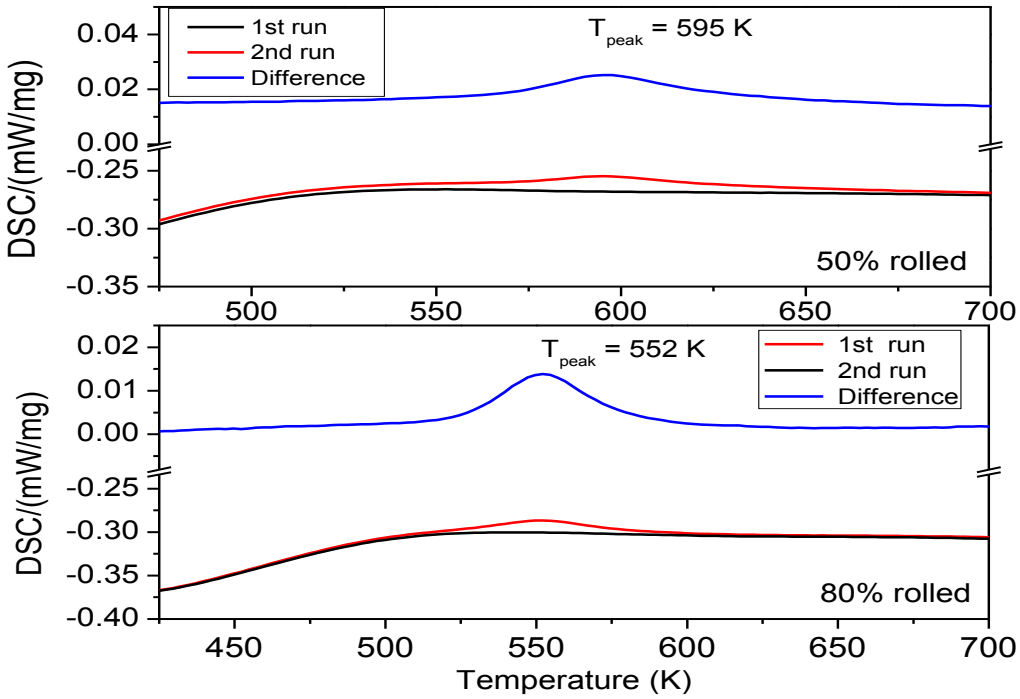

Fig. 5.10: DSC curves of 50% rolled and 80% rolled samples

The area under the curve of the peak gives a measure of the stored energy. It is found to be 38 J/mole and 46 J /mole for 50% and 80% rolled samples respectively as seen in Fig. 5.10. These values corroborate with the studies done by L. Liu *et. al.* as a function of strain in pure copper [159].

It is evident that the stored energy of the 80% rolled sample is larger as compared to the 50% rolled sample. Moreover, the release of the stored energy is found to occur at a lower temperature for the 80% deformation. It is well known that the stored energy causes the recovery and the recrystallization process to occur at a lower temperature [169,170]. This may be attributed to the fact that smaller activation energy is required to release the overall stored energy for the 80% rolled sample, causing the process to start at a lower temperature.

5.5.2. Annealing Study:

When a deformed material is annealed, recovery and recrystallization occur resulting in the formation of defect free grains and thus restoring the property of the material to a significant extent [23,136]. During the recovery process, the microstructural changes are very subtle and occur on a small scale while new defect free grains are nucleated and subsequently grown during the recrystallization process [1]. A division between recovery and recrystallization is thus difficult to define; since recovery mechanism plays a crucial role in nucleating recrystallization [160]. As recovery lowers the driving force for recrystallization, a significant amount of prior recovery may in turn influence the nature and kinetics of recrystallization [168–171]. The evolution of recovery and recrystallization processes in a material depend on the extent of deformation (stored energy in the sample) and also on the nature of the material i.e., the stacking fault energy, impurities etc. [1]. As observed in the last section, the accumulation of stored energy is highly orientation dependent and thus it is expected that the release of the stored energy along different crystallographic orientations will show a different behaviour as a function of time. The in-situ study follows the release of stored energy with time at a particular temperature to understand the dynamics of recovery and recrystallization.

The temperatures for the dynamic study were chosen based on the information from the reported literature [142]. Ph. Gerber*et.al.* [142] have observed that for 90% and 70% rolled pure Cu sample recrystallization of pure Cu starts at around 398 K and 448 K and ends at 473 K and 573 K respectively.

(a) X-ray diffraction studies

The XRD profiles of the ex-situ heated copper samples are plotted for all the four temperatures in the Fig. 5.11(a). From this XRD patterns, the relative intensity ratio of each crystallographic planes are calculated using Eq. 5.1 and plotted in the Fig. 5.11(b). It is evident from Fig. 5.11(b) that in between 441 K and 471 K recrystallization has started and

the {200} cubic texture has formed (the relative intensity ratio of {200} plane has changed between 441 K and 471 K). Hence, the in-situ annealing study has been carried out at three different temperatures 458 K, 473 K and 488 K to understand the dynamics of annealing process.

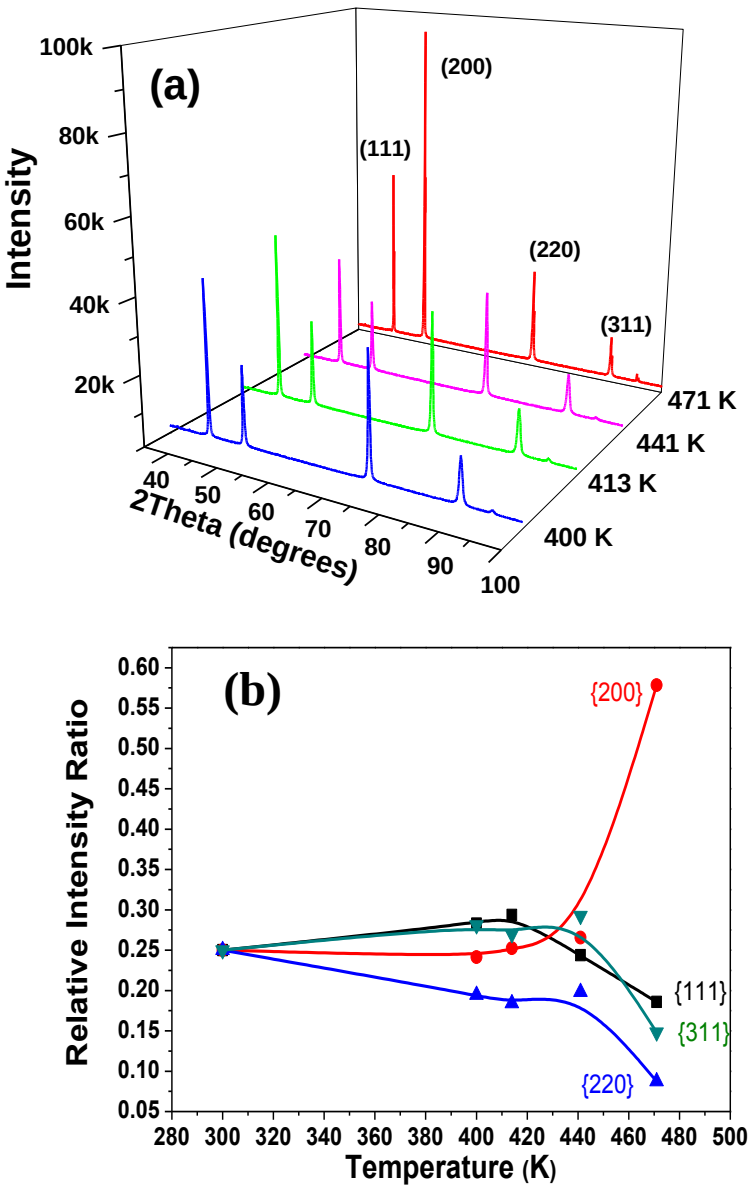

Fig. 5.11: (a) The XRD profile of annealed 80 % rolled copper sample in silicon oil bath at different temperature (b) Relative intensity ratio plot of the annealed sample at different temperature

The primary slip system in the fcc copper material is {111}<110>. As a result, the two major crystallographic planes which show prominent changes in the values of the integrated intensity during the deformation process are the {111} and the {220} planes. Also, at the time of recrystallization, it was observed (in Fig. 5.11(a) and Fig. 5.11(b))from the ex-situ annealing study that cubic texture (alignment of {200} planes) has formed. Hence the in-situ annealing experiment using high temperature XRD has been carried out on these three crystallographic planes ({111}, {220} and {200} planes) only.

The intensity variations of the three crystallographic planes ({111}, {200} and {220} planes) during the annealing of 80% rolled Cu, have been plotted in the Fig. 5.12 (a, b and c).

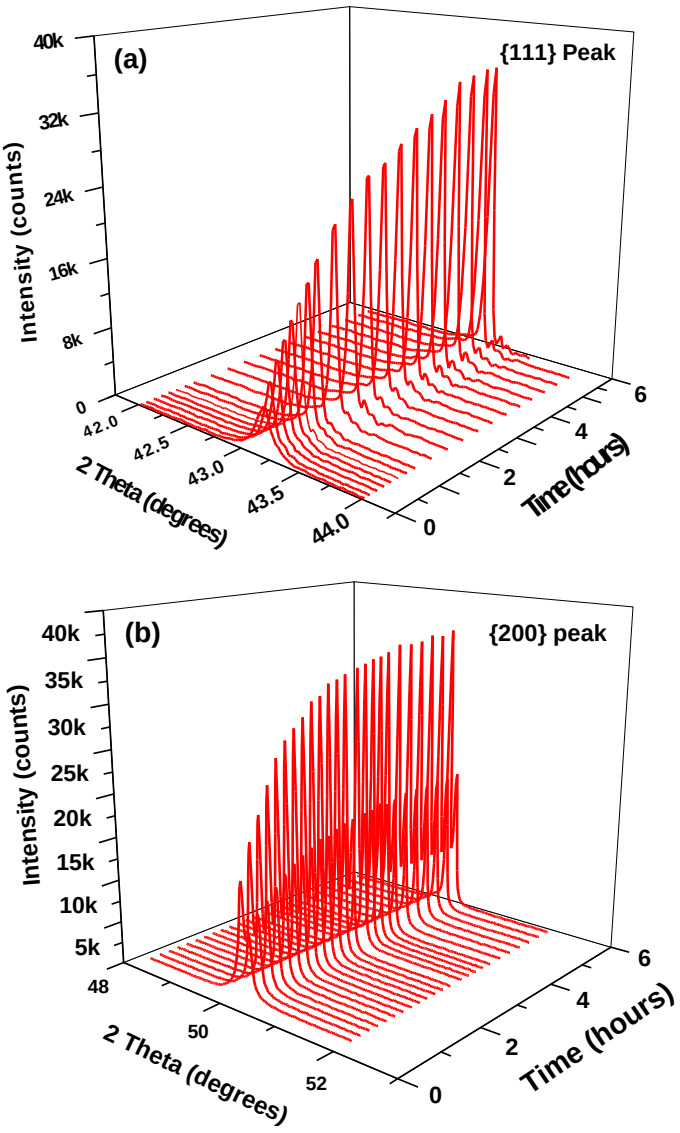

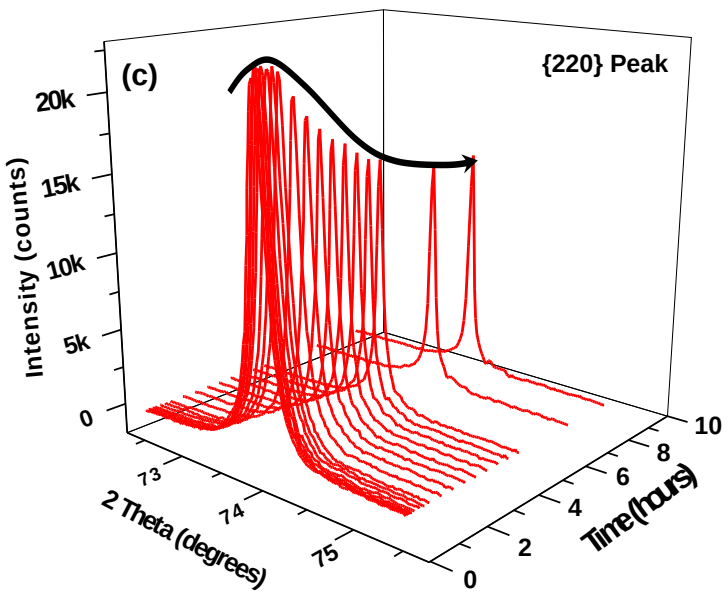

Fig. 5.12: Intensity variation of the XRD profile of (a) {111, (b) {200} and (c) {220} planes during annealing at 458 K of 80 % rolled Cu

The intensity of the {111} and {200} planes systematically increase during the annealing (Fig. 5.12(a) and 5.13(b)). On the other side, the intensity of the {220} plane at first increases and then decreases with annealing time (Fig. 5.12(c)).

Domain size variation along different crystallographic planes:

The single peak analysis of the XRD peaks of {111} and {220} set of planes has been performed to characterise the in-situ evolution of microstructure with time at different temperatures for 80% rolled sample. The corrected integral breadths of {111} and {220} peaks as a function of time are evaluated after correcting for the instrumental broadening and the Debye Waller factor at 458K and 473K. The volume weighted domain sizes for {111} and {220} planes are estimated using the Scherrer's equation (Eq. 2.2) [57] and plotted as a function of time. Fig. 5.13(a) and 5.13(b) reveal that at two different temperatures, a distinct variation in the size of the domains in {111} and {220} planes are observed as a function of time at the initial stage for both the deformed samples.

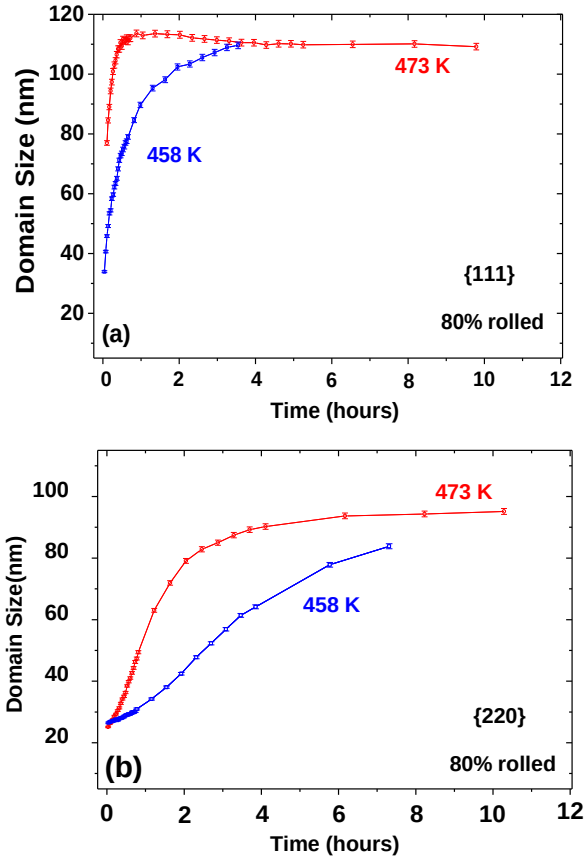

Fig. 5.13: Domain Size variation on (a) {111} planes and (b) {220} planes at two temperatures 458 K and 473 K

The domain size increases rapidly followed by a saturation for {111} and {220} peaks at 473K. But the rise in the domain size is observed to be gradual following a straight line at the initial stage and then saturates with time at an annealing temperature of 458K. In the heavily deformed sample, recovery occurs prior to recrystallization primarily with the changes of dislocation structure in the material. It is to be noted that recovery and recrystallization are competing processes and both are driven by the stored energy of the deformed state [1]. Initially there is a rearrangement of dislocations followed by annihilation which causes increase in the domain size. This may be considered as the recovery stage and the onset of saturation in the domain size as the start of recrystallization stage. The variation in the profile of the evolution of domain size at two different temperatures (Fig. 5.13(a) and 5.13(b)) may have occurred due to the difference in the amount of thermal energy supplied to

the deformed material. Hence, the increase in annealing temperature causes a significant amount of prior recovery at a much lower time.

Measurement of stored energy in different crystallographic planes:

Fig. 5.14 shows the variation of the stored energy with time as calculated using Eq. 5.2 for the 80% rolled sample from the diffraction peak broadening along the {111} planes in a semi-log plot. The variation along {111} planes is monotonic (similar to an exponential decay) at the three different temperatures.

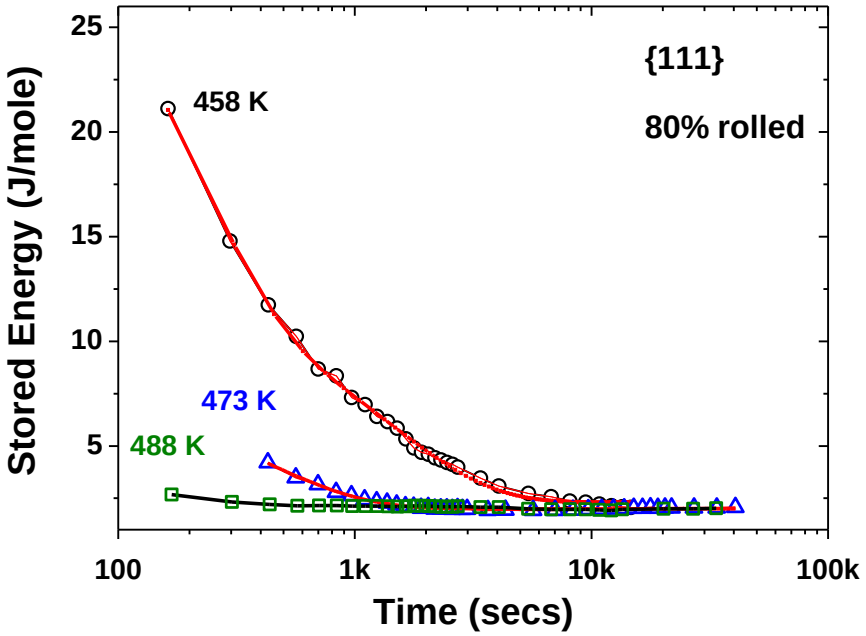

Fig. 5.14: Stored Energy variation in {111} planes at three temperatures 458K, 473K and 488K on 80%rolled Cu. The red line shows the fitted curves (for 458 K and 473K except 488K because of smaller variation).

It is worth noting that the saturation values of the stored energy at the end of the experiments for all the three temperatures are same (within the error bar) which gives good confidence in the experimental procedure. Fig. 5.15(a) and 5.15(b) show the stored energy release with time along the {220} planes for the 50% and the 80% rolled samples at the temperature 458K and

473K respectively. It can be clearly seen that the nature of the variation of the SE with time in the {220} planes (Fig. 5.15) is quite different compared to that of {111} planes (Fig. 5.14).

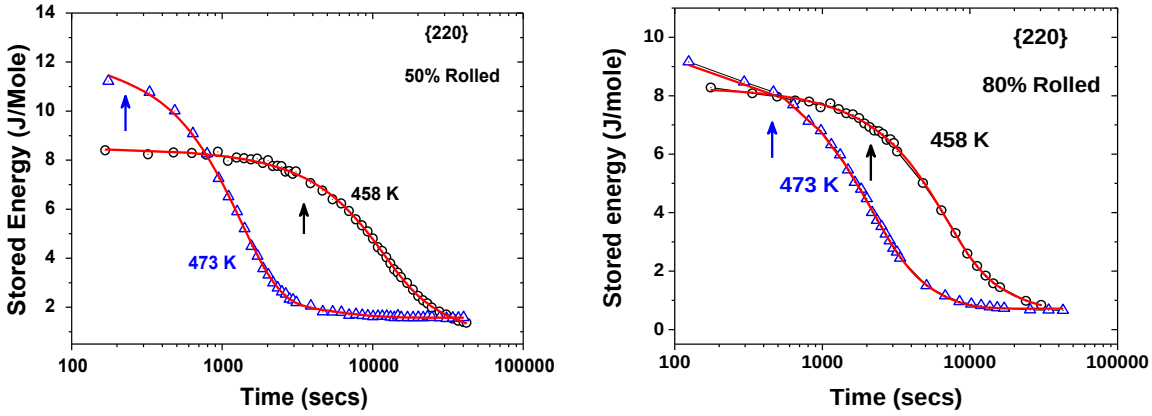

Fig. 5.15: Stored Energy variation for {220} plane at two temperatures 458 K and 473 K on (a) 50% rolled and (b) 80% rolled. The red line shows the fit of the data.

The curve shows two distinct regions: a smaller decrease in the stored energy in the early stage (which will be called as stage I) and then an exponential decay (which will be called as stage II), almost similar to the behaviour of {111} set of planes (Fig. 5.14). The time corresponding to the change-over between the two kinetics is significantly different in the two deformed samples (marked by arrows in Fig. 5.15(a) and 5.15(b)). The change is found to occur at a lower time for 80% deformed sample as compared to 50%, which is expected. In the initial stage, recovery occurs by the rearrangement and annihilation of dislocations and the stored energy vs time curve shows different time dependence compared to that in the second stage which arises due to the initiation of recrystallization processes seen in Fig. 5.15. Since, the amount of stored energy is the driving force of recrystallization, the onset of recrystallization occurs at a lower time for higher deformation (80% deformation). This is also evident from the clear signature of the initial increase in intensity for {220} peaks due to recovery followed by a sharp decrease due to the formation of recrystallized texture as seen in Fig. 5.16. This phenomenon could not be observed for the {111} planes as the release of

stored energy and the dynamic process of annealing are so fast that it could not be followed within the laboratory time scale.

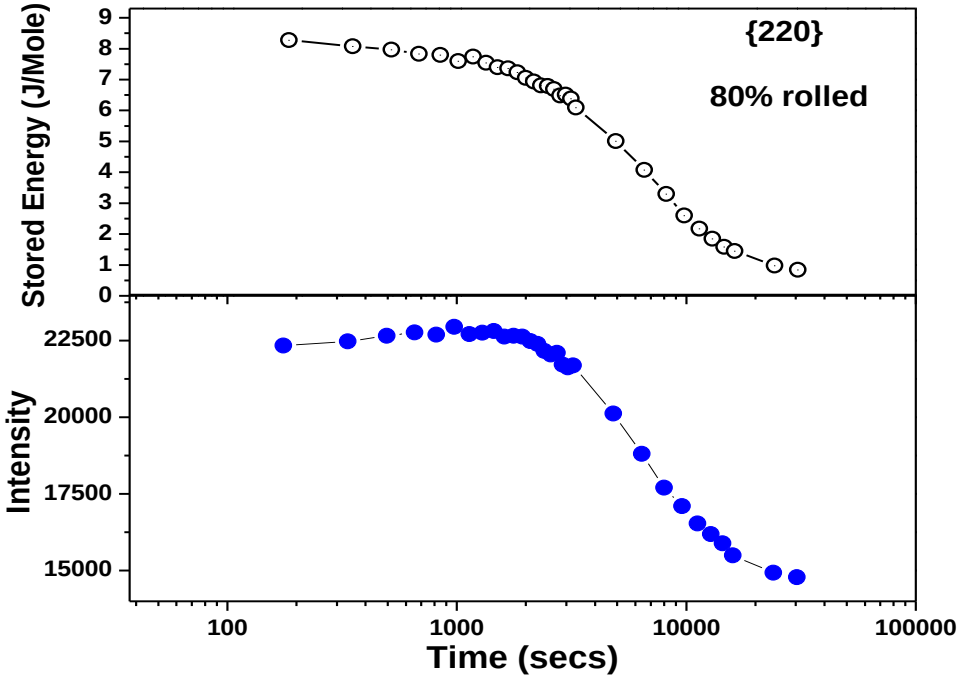

Fig. 5.16: Stored Energy and Peak Intensity variation for {220} plane at temperature 458 K on 80% rolled Cu

The faster dynamics in the {111} can be explained by considering the fact that this plane has the highest planar density of atoms and the initial stored energy is highest (Table 5.3) indicating that this plane can accommodate more dislocations during the deformation process and subsequently on annealing, the stored energy is released at a much faster rate by the faster annihilation of dislocations.

These dynamic processes of annealing responsible for release of the stored energy can be mathematically modelled in the following way. Recovery and recrystallization are the primary process involved in the change in the stored energy of the deformed material. Recovery involves the movement of the dislocations and subsequently their annihilation causing a decrease in the stored energy, and recrystallization involves the process of nucleation and growth of new defect free grains which is also again driven by the stored

energy in the material. The kinetics of these two processes will hence determine the overall variation of the stored energy as a function of time. In a medium stacking fault energy material, the mobility of the dislocation is reduced [172] and hence the movement of the dislocations can thus be considered to be restricted to quasi two dimension and can be modelled as a second order process. The recrystallization on the other hand is restricted to the boundaries of the grains and the interfaces, and hence can be modelled as a first order process [1,173]. As we clearly see from the experimental results above, the kinetics of the release of stored energy is different along the {111} and {220} crystallographic planes in the experimental duration. Hence, it can be conjectured that the time scale of the two processes involved in the release of the stored energy is different along the two planes. This is expected because, {111} set of planes have a higher stored energy and would thus have a lower activation energy compared to the {220} set of planes. The stored energy variation is thus fitted to the following equation.

$$SE(t) = SE_{t=\infty} + Ae^{-\left(\frac{t+t0}{\tau_1}\right)^2} + Be^{-\left(\frac{t+t0}{\tau_2}\right)} \quad \textbf{(5.4)}$$

Where, τ_1 and τ_2 are the time constants of the second order (recovery) and the first order (recrystallization) process respectively. A time 't_0' has been included in the two terms to account for the experimental delay time (required to be introduced to account for the time during which both the processes have already began before the start of the experimental observation). Coefficients A and B give the relative contribution of recovery and recrystallization process to the dynamics. The stored energy variation has been fitted using this equation and the values obtained are tabulated in Table 5.4. The fitting curves are superposed on the experimental data in Fig. 5.14, 5.15(a) and 5.15(b). It can be seen from the Table 5.4 that the time constants of the two processes are varying systematically with temperature as well as the deformation. In the 80% rolled sample, the time constants of the

recovery and recrystallization processes are much less along the {111} plane compared to the {220} plane. In fact, at T=473K, the curve could be fitted with only the first order process with a small time constant of 423 secs. Along the {220} plane, the 80% rolled sample has lower time constants compared to the 50% rolled sample. This is also expected since the 80% rolled sample has a higher stored energy thus enabling the recovery and also the recrystallization process to start at an earlier time compared to that of the 50% rolled sample. From Table 5.4, it can be seen that for the 50% rolled sample, annealed at 458K, the time constants of the two processes are quite large and is comparable to the maximum experimental time. It can also be seen from Fig. 5.16 (b) that the release of the stored energy is not completed in the sample subjected to 458K within the experimental time. This can also be corroborated with the EBSP analysis and the misorientation angle distribution of the same sample as discussed below. The large differences in the time constants along the {111} and {220} planes clearly indicate that there is a marked difference in the kinetics of the two processes i.e., recovery and recrystallization along the different crystallographic planes and the activation energy of the processes is also different in the different planes.

Table 5.4: Parameters obtained by fitting Eq. (5.2) to the observed stored energy variation as a function of time.

Sample	Temperature (K)	Peak	$SE_{t=\infty}$ (J/mole)	t0 (secs)	$\tau 1$ (secs)	$\tau 2$ (secs)	A (J/mole)	B (J/mole)
80% rolled	458	{111}	2.3	1200	704	1420	409.3	23.7
	473	{111}	2.0	577	-	423	0	23.5
	458	{220}	0.6	1200	7565	9784	3.8	4.4
	473	{220}	0.7	577	2461	2657	3.5	6.6
50% rolled	458	{220}	0.9	1200	12160	17500	3.3	4.6
	473	{220}	1.6	577	1729	3615	1.3	10.6

(b) EBSP study on the annealed samples:

The band contrast images of the annealed samples using EBSP shows clear indication of well recrystallized grains as shown in Fig. 5.17(a) and 5.17(b). It is evident from the observations

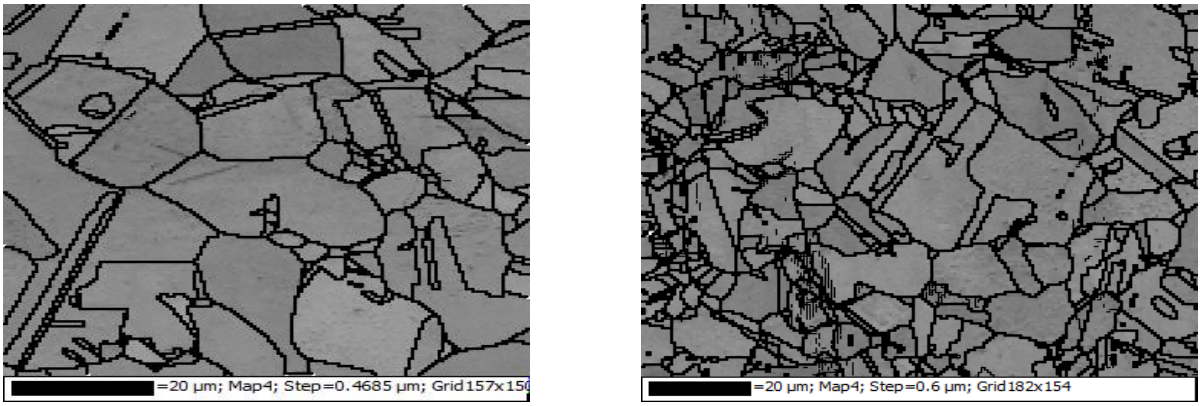

Fig. 5.17: EBSD band contras images of the annealed samples after (a) 50% rolled and (b) 80% rolled

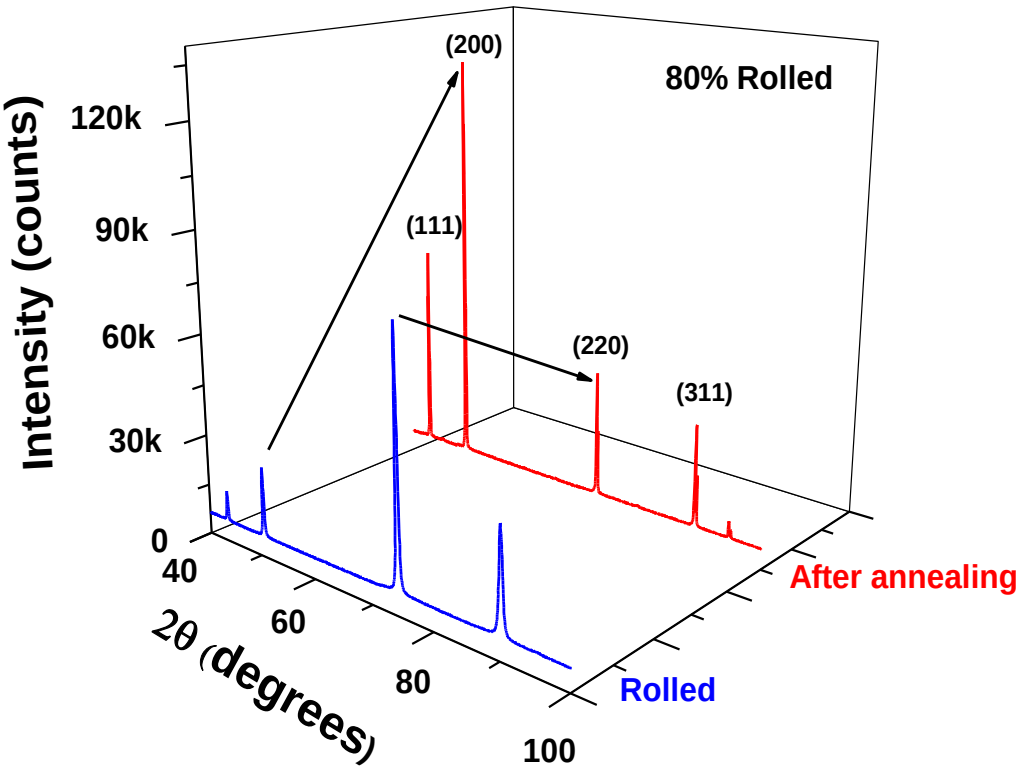

Fig. 5.18: X-ray diffraction patterns of the 80% rolled sample before and after annealing. (Arrows indicate the decrease in the (220) intensity and the increase in the (200) intensity).

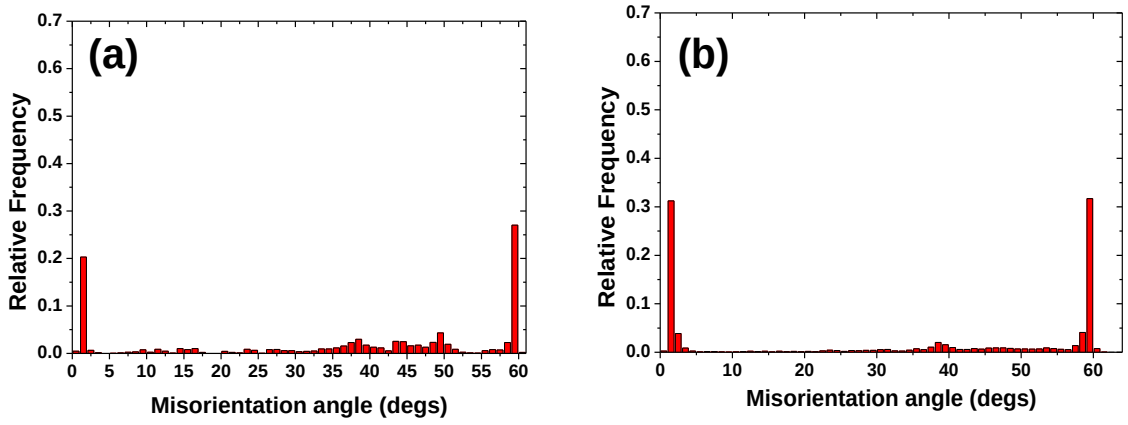

Fig. 5.19: Frequency distribution of misoriention angle of the annealed samples (a) 50% rolled and (b) 80% rolled

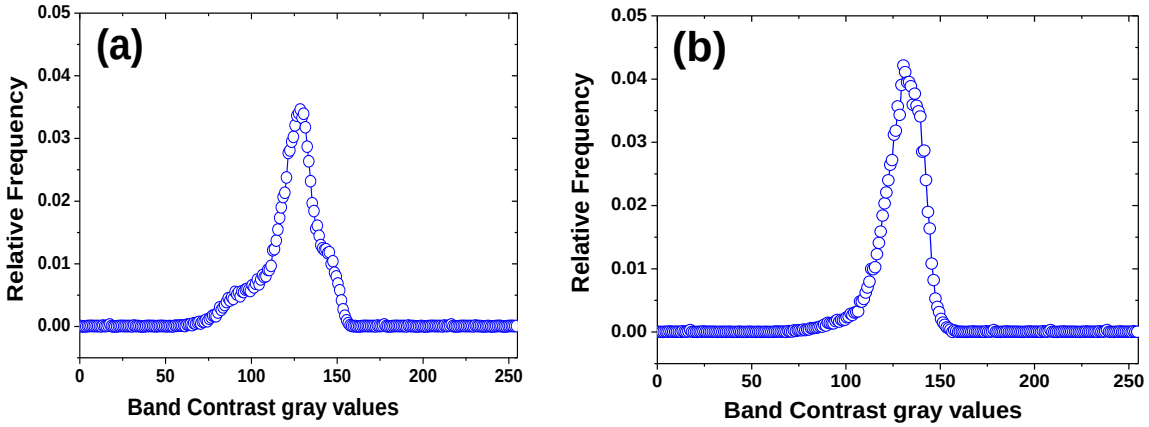

Fig. 5.20: Frequency distribution of band contrast of the annealed samples (a) 50% rolled and (b) 80% rolled

that the irregular shaped boundaries as seen in Fig. 5.2(b) and 5.2(c) have changed to sharper boundaries with larger misorientation among the grains. This is especially more significant in the 80% rolled sample.

This can also be corroborated with the XRD peaks (Fig. 5.18) which show clear changes in the peak intensity of {200} and {220} planes indicating the formation of recrystallized texture. It can be seen that for the 80% rolled sample, both the misorientation angle distribution (Fig. 5.19(b) which shows a significant number of high misorientation angle boundaries) and the band contrast distribution (Fig. 5.20(b) which shows a peak shift

towards the high gray values and a much sharper distribution function) clearly show that new defect free grains are formed. In the case of the 50% rolled sample, the misorientation angle distribution (Fig. 5.19(a)) and the band contrast (Fig. 5.20(a)) clearly indicates that significant recrystallization has not taken place. There are formation of new grains with lower misorientation angle and only a slight shift of the band contrast distribution function to higher gray values.

5.6 Conclusion:

Detailed characterisation of a deformed materials has been carried out with respect to microstructure (grain size, domain size, microstrain), stored energy (overall and along specific planes), temporal evolution of microstructure and release of stored energy at different temperatures to study the annealing phenomenon. The deformed Cu samples have been used to understand the kinetics of the release of stored energy along different crystallographic planes during the annealing process. The microstructure has been characterised using EBSP which reveals irregular grain boundaries with increasing deformation. The microstructural parameters as evaluated using XRDLPA technique show a decrease in domain size whereas the microstrain remains almost constant. The overall stored energy is found to increase with deformation. The stored energy along the different crystallographic planes has been evaluated using the modified Stibitz formula and it is seen that the accumulation of stored energy is much higher in {111} set of planes as compared to the other planes. The kinetics of the release of the stored energy along the {111} and {220} set of planes are followed using in-situ XRD measurements carried out at 458K and 473K on the deformed samples. The process dynamics of the recovery and the recrystallization are explained clearly from the observed time dependent variation of the stored energy in the {220} set of planes. The two processes are found to follow second order and first order dynamics respectively.

Chapter 6

Conclusion and future scope of the work

In this thesis, three different problems of high significance related to ion irradiation and deformation of fcc materials has been studied in detail. The topics are (1) understanding the defect dynamics and importance of pre-existing defects (that act as sinks), in determining the final microstructure of ion irradiated material, (2) determining the combined effect of varying the strain-state (pre-strain), the pre-strain and post-strain rates on the deformation induced austenite-martensite phase transformation in steels and (3) assessing the process dynamics along different crystallographic planes during biaxial deformation and subsequent annealing of fcc material. The evaluation of the microstructure in terms of the size of the coherent domain (determined by the arrangement of the defects) and the micro strain caused by the presence of defects (mainly dislocations in our study) has been studied in detail using different techniques of X-ray diffraction line profile analysis. Along with the XRD analysis, the microstructure has also been assessed using EBSD. Additional experimental tools have also been used to give support to the results obtained from XRDLPA and EBSD analysis. The outcome of the studies discussed in this thesis can give impetus for similar studies to be carried out in the field of deformation and ion irradiation of materials.

The study of depth wise assessment of the microstructure in α- irradiated alloy D9 discussed in Chapter 3 clearly showed the evidence of the phenomena of radiation enhanced diffusion (RED) where new diffusion channels are created due to the irradiation produced defects. The importance of the presence of pre-existing sinks in determining the final microstructure could be clearly observed. In our study, the alloy D9 had the microstructure of hot rolled, solution annealed and rapidly quenched material. This resulted in significant

amount of microstructural imperfections which could act as sinks for the irradiation induced defects. It was observed that at low doses of irradiation where the defect concentration is less, the variation in the microstructure (domain size) was significant but systematic as a function of depth. With increasing dose, the pre-existing sinks are completely annihilated and the defect diffusion causes a homogenous microstructure as a function of depth. With further increase in dose, there is no significant change in the microstructure which indicates that a steady state has been reached. This is due to the delicate balance of the defect production rate, radiation enhanced diffusion and defects annihilation at pre-existing and newly created sinks. This study could hence show the importance of both the initial microstructure of the material and also the phenomena of radiation enhanced diffusion. This study also indicates that one should exercise caution while carrying out characterisation of ion irradiated materials, since the final microstructure is an interplay of many factors. Hence assessing the damage profile as a function of depth is important before arriving at a conclusion on the radiation induced changes in material properties.

The second study (Chapter 4) was on austenite- martensite (phase) transformation in SS304 during uniaxial tensile deformation using different pre-strain, pre-strain rates and post-strain rates. This study could clearly show that the percentage of martensitic phase could be enhanced by suitable combination of these deformation parameters. XRDLPA results along with that of EBSD studies on the lattice correlation and the orientation relationship of the phase boundaries between austenite and martensite could give a clue for this observation. It could be shown that higher pre-strain rate helps in the formation of two types of martensite nuclei (with different angular deviation from KS relationship), while the slow post-strain rate could help in the growth of more martensite in all the nucleated points. Considering that multiple combination of parameters controls the mechanism of martensitic transformation, this study can considerably contribute to the deformation induced phase transformation of

similar materials. Moreover, such studies can help during the quest of special alloys with improved ductility and strength.

The evolution of stored energy (hence changes in the microstructure) along different crystallographic planes in rolled copper is described in Chapter 5. From this study we could categorically show that defect dynamics during annealing of a deformed material is highly crystallographic plane dependent. The changes in the X-ray line profile of each crystallographic plane during high temperature annealing was followed meticulously using in-situ measurements on 50% and 80% deformed copper samples. The temporal variation of the stored energy evaluated using the XRD data could clearly show that the process of recovery and recrystallization is different along different crystallographic planes and also dependent on the initial deformation stage. This study could show that in any thermo-mechanical treatment of the material during manufacturing process proper choice of parameters are important. This will ensure that the required mechanical properties dictated by the microstructure can be achieved during the production of the material.

All the above studies have thrown open many questions some of which are outlined below.

1. The role of the pre-existing sinks in determining the final microstructure of ion irradiated materials can be understood systematically by carrying out irradiation on materials with different percentage of initial deformation (which determines the number of pre-existing sinks). By choosing a combination of deformation, irradiation dose, dose-rate and temperature of irradiation an exhaustive study of importance of all parameters in deciding the final microstructure of irradiated materials can be understood.

2. In general, biaxial deformation is mostly used during material forming. There have been contradicting reports on martensite formation during biaxial loading in stainless steels. Taking clue from our study, the martensite phase formation can be carefully manipulated

using the deformation process parameters. Hence, carrying out similar studies during biaxial loading will help to resolve these issues.

3. BCC metals and alloys are being explored as candidate materials for several high temperature applications. This is due to their improved high temperature mechanical properties in comparison to fcc. However, most bcc materials are brittle and careful procedures have to be followed during the manufacture of their components. Study of evolution of stored energy along the different crystallographic planes in deformed bcc materials can help is deciding the thermomechanical parameters for proper finished product. Preliminary studies in laboratory scale can help in finding the correct temperature and time scales for the processing of the materials. Since bcc does not have a closed packed plane unlike fcc, it doesn't have any well-defined single slip system and at high temperature many of the 48 slip systems may be active hence may result in a different defect dynamic compared to fcc which may aid the defect dynamics in a different manner compared to in fcc.

4. All these studies have been carried out using the materials with coarse grain structure. But it is well known that the grain boundary area by volume ratio will alter the defect dynamics. On the other hand, the grain boundaries act as probable nucleation site for new phases. Thus, various materials with different grain size can alter the dynamics of deformation induced phase transformation. So the study related to the effects of deformation and irradiation on any material with ultrafine, fine and coarse grain structure have its majestic impact on metallurgical study.

Chapter 6

Conclusion and future scope of the work

In this thesis, three different problems of high significance related to ion irradiation and deformation of fcc materials has been studied in detail. The topics are (1) understanding the defect dynamics and importance of pre-existing defects (that act as sinks), in determining the final microstructure of ion irradiated material, (2) determining the combined effect of varying the strain-state (pre-strain), the pre-strain and post-strain rates on the deformation induced austenite-martensite phase transformation in steels and (3) assessing the process dynamics along different crystallographic planes during biaxial deformation and subsequent annealing of fcc material. The evaluation of the microstructure in terms of the size of the coherent domain (determined by the arrangement of the defects) and the micro strain caused by the presence of defects (mainly dislocations in our study) has been studied in detail using different techniques of X-ray diffraction line profile analysis. Along with the XRD analysis, the microstructure has also been assessed using EBSD. Additional experimental tools have also been used to give support to the results obtained from XRDLPA and EBSD analysis. The outcome of the studies discussed in this thesis can give impetus for similar studies to be carried out in the field of deformation and ion irradiation of materials.

The study of depth wise assessment of the microstructure in α- irradiated alloy D9 discussed in Chapter 3 clearly showed the evidence of the phenomena of radiation enhanced diffusion (RED) where new diffusion channels are created due to the irradiation produced defects. The importance of the presence of pre-existing sinks in determining the final microstructure could be clearly observed. In our study, the alloy D9 had the microstructure of hot rolled, solution annealed and rapidly quenched material. This resulted in significant

amount of microstructural imperfections which could act as sinks for the irradiation induced defects. It was observed that at low doses of irradiation where the defect concentration is less, the variation in the microstructure (domain size) was significant but systematic as a function of depth. With increasing dose, the pre-existing sinks are completely annihilated and the defect diffusion causes a homogenous microstructure as a function of depth. With further increase in dose, there is no significant change in the microstructure which indicates that a steady state has been reached. This is due to the delicate balance of the defect production rate, radiation enhanced diffusion and defects annihilation at pre-existing and newly created sinks. This study could hence show the importance of both the initial microstructure of the material and also the phenomena of radiation enhanced diffusion. This study also indicates that one should exercise caution while carrying out characterisation of ion irradiated materials, since the final microstructure is an interplay of many factors. Hence assessing the damage profile as a function of depth is important before arriving at a conclusion on the radiation induced changes in material properties.

The second study (Chapter 4) was on austenite- martensite (phase) transformation in SS304 during uniaxial tensile deformation using different pre-strain, pre-strain rates and post-strain rates. This study could clearly show that the percentage of martensitic phase could be enhanced by suitable combination of these deformation parameters. XRDLPA results along with that of EBSD studies on the lattice correlation and the orientation relationship of the phase boundaries between austenite and martensite could give a clue for this observation. It could be shown that higher pre-strain rate helps in the formation of two types of martensite nuclei (with different angular deviation from KS relationship), while the slow post-strain rate could help in the growth of more martensite in all the nucleated points. Considering that multiple combination of parameters controls the mechanism of martensitic transformation, this study can considerably contribute to the deformation induced phase transformation of

similar materials. Moreover, such studies can help during the quest of special alloys with improved ductility and strength.

The evolution of stored energy (hence changes in the microstructure) along different crystallographic planes in rolled copper is described in Chapter 5. From this study we could categorically show that defect dynamics during annealing of a deformed material is highly crystallographic plane dependent. The changes in the X-ray line profile of each crystallographic plane during high temperature annealing was followed meticulously using in-situ measurements on 50% and 80% deformed copper samples. The temporal variation of the stored energy evaluated using the XRD data could clearly show that the process of recovery and recrystallization is different along different crystallographic planes and also dependent on the initial deformation stage. This study could show that in any thermo-mechanical treatment of the material during manufacturing process proper choice of parameters are important. This will ensure that the required mechanical properties dictated by the microstructure can be achieved during the production of the material.

All the above studies have thrown open many questions some of which are outlined below.

1. The role of the pre-existing sinks in determining the final microstructure of ion irradiated materials can be understood systematically by carrying out irradiation on materials with different percentage of initial deformation (which determines the number of pre-existing sinks). By choosing a combination of deformation, irradiation dose, dose-rate and temperature of irradiation an exhaustive study of importance of all parameters in deciding the final microstructure of irradiated materials can be understood.

2. In general, biaxial deformation is mostly used during material forming. There have been contradicting reports on martensite formation during biaxial loading in stainless steels. Taking clue from our study, the martensite phase formation can be carefully manipulated

using the deformation process parameters. Hence, carrying out similar studies during biaxial loading will help to resolve these issues.

3. BCC metals and alloys are being explored as candidate materials for several high temperature applications. This is due to their improved high temperature mechanical properties in comparison to fcc. However, most bcc materials are brittle and careful procedures have to be followed during the manufacture of their components. Study of evolution of stored energy along the different crystallographic planes in deformed bcc materials can help is deciding the thermomechanical parameters for proper finished product. Preliminary studies in laboratory scale can help in finding the correct temperature and time scales for the processing of the materials. Since bcc does not have a closed packed plane unlike fcc, it doesn't have any well-defined single slip system and at high temperature many of the 48 slip systems may be active hence may result in a different defect dynamic compared to fcc which may aid the defect dynamics in a different manner compared to in fcc.

4. All these studies have been carried out using the materials with coarse grain structure. But it is well known that the grain boundary area by volume ratio will alter the defect dynamics. On the other hand, the grain boundaries act as probable nucleation site for new phases. Thus, various materials with different grain size can alter the dynamics of deformation induced phase transformation. So the study related to the effects of deformation and irradiation on any material with ultrafine, fine and coarse grain structure have its majestic impact on metallurgical study.

Summary

Microstructure of a material strongly influences some of its major physical and mechanical properties. This can in principle be controlled during the metal forming process (which includes both deformation and annealing). In service conditions, the microstructure may get altered and as a consequence can affect the properties of the material. Deformation and particle irradiation are two such processes among others during which changes in the microstructure can occur. The effect of such changes on the physical properties may be either beneficial or detrimental. To achieve the desired final properties of the material for a particular application and to understand the changes during in-service conditions, a thorough knowledge of the material should be gathered beforehand.

In this thesis, we have studied some of the relevant but so far unaddressed problems related to deformation and irradiation phenomena in face centered cubic (fcc) materials. X-ray diffraction technique has been used as the major tool for characterising the microstructure of the materials throughout this study. Detail X-ray line profile analysis techniques have been used to understand in-depth the microstructural changes in the materials to varying levels of complexity. Other characterization tools such as electron back scattering diffraction (EBSD), differential scanning calorimetry (DSC) and vibrating sample magnetometer (VSM) have been additionally employed to support the findings of XRD.

The three main topics that have been addressed are: defects diffusion in ion irradiated materials, deformation induced phase transformation and nature of defects dynamics along different crystallographic planes during annealing of a deformed material. The choice of the material to carry out the individual studies was based on the property of the material and its relevance in the different applications. Alloy D9, SS304 and electrolytic Copper were chosen to carry out the studies respectively.

In summary, the work in this thesis demonstrates that systematic evaluation of the microstructure of the material during irradiation and deformation (and subsequent annealing) is important to understand the defect dynamics, which controls the final material properties. The depth wise characterisation of the microstructure of ion irradiated alloy D9 (which is an important material for in-core application in fast breeder nuclear reactors) has categorically shown that the final microstructure is controlled by the radiation enhanced defect diffusion and presence of pre-existing sinks in the initial material. It is observed that after a certain dose of irradiation a steady state is reached due to the fine balance between the production of the defects and their annihilation in sinks (pre-existing and newly formed) aided by the radiation enhanced diffusion. In the deformation induced phase transformation study carried out on SS304 sample, it is shown that a combination of deformation parameters such as pre-strain (strain state), pre-strain and post-strain rates help to enhance the martensite percentage. The findings in this study may help in designing high performance materials with improved plasticity. The difference in the dynamics of the release of stored energy along different crystallographic planes during annealing (of a deformed material) has been studied in biaxially rolled copper. Due to the availability of preferred slip systems in fcc material, it is seen that the evolution of the defects and hence the release of stored energy has different temporal behaviour along the different planes. This result can have significant impact on selecting the process parameters particularly annealing temperature and time in order to achieve the desired properties.

The results presented in this thesis can give impetus to carry out meticulous experiments for characterisation of deformed and ion irradiated materials.

References

[1] F.J. Humphreys, M. Hatherly, Recrystallization and related annealing phenomena, Elsevier, 2012.

[2] G.S. Was, Fundamentals of radiation materials science: metals and alloys, springer, 2016.

[3] M. Eckert, Max von Laue and the discovery of X-ray diffraction in 1912, Ann. Phys. 524 (2012) 83–85. doi:10.1002/andp.201200724.

[4] G.B. Greenough, Quantitative X-ray diffraction observations on strained metal aggregates, Prog. Met. Phys. 3 (1952) 176–219.

[5] B.E. Warren, X-ray studies of deformed metals, Prog. Met. Phys. 8 (1959) 147–202. doi:10.1016/0502-8205(59)90015-2.

[6] M. De, S.P. Sen Gupta, Lattice imperfection studies in polycrystalline materials by x-ray diffraction line-profile analysis, Pramana. 23 (1984) 721–744.

[7] R.K. Nandi, H.K. Kuo, W. Schlosberg, G. Wissler, J.B. Cohen, B. Crist, Single-peak methods for Fourier analysis of peak shapes, J. Appl. Crystallogr. 17 (1984) 22–26.

[8] L. Lutterotti, P. Scardi, P. Maistrelli, LSI-a computer program for simultaneous refinement of material structure and microstructure, J. Appl. Crystallogr. 25 (1992) 459–462. doi:10.1107/S0021889892001122.

[9] G.K. Williamson, W.H. Hall, X-ray line broadening from filed aluminium and wolfram, Acta Met. 1 (1953) 22–31.

[10] T.H. De Keijser, J.I. Langford, E.J. Mittemeijer, A.B.P. Vogels, Use of the Voigt function in a single-line method for the analysis of X-ray diffraction line broadening, J. Appl. Crystallogr. 15 (1982) 308–314.

[11] L. Lutterotti, S. Matthies, H.R. Wenk, MAUD: a friendly Java program for material analysis using diffraction, IUCr Newsl. CPD. 21 (1999).

[12] G. Ribárik, T. Ungár, J. Gubicza, MWP-fit: a program for multiple whole-profile fitting of diffraction peak profiles by ab initio theoretical functions, J. Appl. Cryst. 34 (2001) 669–676.

[13] G. Sharma, P. Mukherjee, A. Chatterjee, N. Gayathri, A. Sarkar, J.K. Chakravartty, Study of the effect of α irradiation on the microstructure and mechanical properties of nanocrystalline Ni, Acta Mater. 61 (2013) 3257–3266.

[14] M. Knoll, E. Ruska, Das elektronenmikroskop, Zeitschrift Für Phys. 78 (1932) 318–339.

[15] F.L. Deepak, A. Mayoral, R. Arenal, Advanced transmission electron microscopy: Applications to nanomaterials, Springer, 2015.

[16] E. Ruska, The development of the electron microscope and of electron microscopy (Nobel Lecture), Angew. Chemie Int. Ed. English. 26 (1987) 595–605.

[17] D. McMullan, Scanning electron microscopy 1928--1965, Scanning. 17 (1995) 175–185.

[18] A.J. Schwartz, M. Kumar, B.L. Adams, D.P. Field, Electron backscatter diffraction in materials science, Springer, 2009.

[19] F.J. Humphreys, Characterisation of fine-scale microstructures by electron backscatter diffraction (EBSD), Scr. Mater. 51 (2004) 771–776.

[20] V. Randle, Microtexture determination and its applications, Maney Publishing, 2003.

[21] O. Kelly, Brian Thomas, Irradiation damage to solids, Pergamon Press Oxford, 1966.

[22] A. E521-16, Standard Practice for Investigating the Effects of Neutron Radiation Damage Using Charged-Particle Irradiation, (2016).

[23] G.E. Dieter, D.J. Bacon, Mechanical metallurgy, McGraw-hill New York, 1986.

[24] DE Laughlin and K. Hono, Physical Metallurgy, Fifth Edit, Elsevier, Oxford, 2014. doi:https://doi.org/10.1016/B978-0-444-53770-6.18001-3.
[25] G.I. Taylor, The mechanism of plastic deformation of crystals. Part I.—Theoretical, Proc. R. Soc. London. Ser. A, Contain. Pap. a Math. Phys. Character. 145 (1934) 362–387.
[26] M. Polanyi, Über eine Art Gitterstörung, die einen Kristall plastisch machen könnte, Zeitschrift Für Phys. 89 (1934) 660–664.
[27] E. Orowan, Zur kristallplastizität. iii, Zeitschrift Für Phys. 89 (1934) 634–659.
[28] J.M. Hedges, J.W. Mitchell, The observation of polyhedral sub-structures in crystals of silver bromide, London, Edinburgh, Dublin Philos. Mag. J. Sci. 44 (1953) 223–224.
[29] D. Hull, D.J. Bacon, Introduction to dislocations, Elsevier, 2011.
[30] D. Zhang, L. Jiang, B. Zheng, J.M. Schoenung, S. Mahajan, E.J. Lavernia, I.J. Beyerlein, J.M. Schoenung, E.J. Lavernia, Deformation Twinning (Update), Ref. Modul. Mater. Sci. Mater. Eng. (2016) 1–24. doi:10.1016/b978-0-12-803581-8.02878-2.
[31] D.A. Porter, K.E. Easterling, Phase transformations in metals and alloys (revised reprint), CRC press, 2009.
[32] E. Pereloma, D. V Edmonds, Phase transformations in steels: Diffusionless transformations, high strength steels, modelling and advanced analytical techniques, Elsevier, 2012.
[33] S. Allen, Todd R and Stoller, Roger E and Yamanaka, Comprehensive nuclear materials, Elsevier, 2012.
[34] G.S. Was, R.S. Averback, Radiation damage using ion beams, in: Compr. Nucl. Mater., Elsevier Ltd, 2012: pp. 195–221.
[35] K. V Kasiviswanathan, V. Karthik, C.N. Venkiteswaran, T. Johny, N.G. Muralidharan, J. Joseph, Performance assessment of fuel and core structural materials irradiated in FBTR, Energy Procedia. 7 (2011) 129–139.
[36] C. David, B.K. Panigrahi, S. Balaji, A.K. Balamurugan, K.G.M. Nair, G. Amarendra, C.S. Sundar, B. Raj, A study of the effect of titanium on the void swelling behavior of D9 steels by ion beam simulation, J. Nucl. Mater. 383 (2008) 132–136.
[37] S. Latha, M.D. Mathew, P. Parameswaran, K.B.S. Rao, S.L. Mannan, Thermal creep properties of alloy D9 stainless steel and 316 stainless steel fuel clad tubes, Int. J. Press. Vessel. Pip. 85 (2008) 866–870.
[38] M.D. Mathew, K.A. Gopal, S. Murugan, B.K. Panigrahi, A.K. Bhaduri, T. Jayakumar, Development of IFAC-1 SS: an advanced austenitic stainless steel for cladding and wrapper tube applications in sodium-cooled fast reactors, in: Adv. Mater. Res., 2013: pp. 749–756.
[39] V. Seetharaman, Deformation and martensitic transformation, Bull. Mater. Sci. 6 (1984) 703–716.
[40] A. Das, S. Sivaprasad, M. Ghosh, P.C. Chakraborti, S. Tarafder, Morphologies and characteristics of deformation induced martensite during tensile deformation of 304 LN stainless steel, Mater. Sci. Eng. A. 486 (2008) 283–286. doi:10.1016/j.msea.2007.09.005.
[41] A.S.T.M. Internasional, ASTM D638-02 Standard Test Methods for Tensile Properties of Plastic, in: Am. Soc. Test. Mater., 2002.
[42] J. Gubicza, X-ray line profile analysis in materials science, IGI Global, 2014.
[43] G. Caglioti, A. t Paoletti, F.P. Ricci, Choice of collimators for a crystal spectrometer for neutron diffraction, Nucl. Instruments. 3 (1958) 223–228.
[44] G. Ribárik, Modeling of diffraction patterns based on microstructural properties, Eötvös Loránd University, 2008.

[45] T. Ungár, H. Mughrabi, M. Wilkens, An X-Ray line-broadening study of dislocations near the surface and in the bulk of deformed copper single crystals, Acta Metall. 30 (1982) 1861–1867. doi:https://doi.org/10.1016/0001-6160(82)90026-8.
[46] A. Sarkar, P. Mukherjee, P. Barat, X-ray diffraction studies on asymmetrically broadened peaks of heavily deformed zirconium-based alloys, Mater. Sci. Eng. A. 485 (2008) 176–181. doi:https://doi.org/10.1016/j.msea.2007.07.063.
[47] P. Mukherjee, A. Sarkar, P. Barat, S.K. Bandyopadhyay, P. Sen, S.K. Chattopadhyay, P. Chatterjee, S.K. Chatterjee, M.K. Mitra, Deformation characteristics of rolled zirconium alloys: a study by X-ray diffraction line profile analysis, Acta Mater. 52 (2004) 5687–5696.
[48] P.S. Chowdhury, N. Gayathri, P. Mukherjee, M. Bhattacharya, A. Chatterjee, A. Dutta, P. Barat, In situ studies of evolution of microstructure with temperature in heavily deformed Ti-modified austenitic stainless steel by X-ray diffraction technique, Mater. Sci. Eng. A. 528 (2011) 967–972. doi:https://doi.org/10.1016/j.msea.2010.09.102.
[49] P. Mukherjee, P. Barat, S.K. Bandyopadhyay, P. Sen, S.K. Chottopadhyay, S.K. Chatterjee, M.K. Mitra, Characterisation of microstructural parameters in oxygen-irradiated Zr-1.0% Nb-1.0% Sn-0.1% Fe, J. Nucl. Mater. 305 (2002) 169–174.
[50] P. Mukherjee, A. Sarkar, P. Barat, Microstructural changes in oxygen-irradiated zirconium-based alloy characterised by X-ray diffraction techniques, Mater. Charact. 55 (2005) 412–417.
[51] P. Mukherjee, F.A. Sarkar, P. Barat, B. Raj, U.K. Mudali, Microstructural studies on lattice imperfections in irradiated titanium and Ti-5 pct Ta-2 pct Nb by X-ray diffraction line-profile analysis, Metall. Mater. Trans. A. 36 (2005) 2351–2360.
[52] S. Neogy, P. Mukherjee, A.P. Srivastava, M.N. Singh, N. Gayathri, A.K. Sinha, D. Srivastava, G.K. Dey, Proton irradiation of Zr-1 wt.% Nb cladding material: A depth-wise assessment of inhomogeneous microstructural damage using X-ray diffraction line profile analyses, J. Alloys Compd. 640 (2015) 175–182.
[53] P. Mukherjee, A. Sarkar, M. Bhattacharya, N. Gayathri, P. Barat, Post-irradiated microstructural characterisation of cold-worked SS316L by X-ray diffraction technique, J. Nucl. Mater. 395 (2009) 37–44.
[54] A.D. Gupta, P. Mukherjee, N. Gayathri, P. Bhattacharyya, M. Bhattacharya, A. Sarkar, S. Sen, M.K. Mitra, Proton irradiation studies on pure Ti and Ti-6Al-4V, Nucl. Instruments Methods Phys. Res. Sect. B Beam Interact. with Mater. Atoms. 387 (2016) 63–72.
[55] P. Bhattacharyya, N. Gayathri, M. Bhattacharya, A.D. Gupta, A. Sarkar, S. Dhar, M.K. Mitra, P. Mukherjee, Proton irradiation studies on Al and Al5083 alloy, Radiat. Phys. Chem. 139 (2017) 132–140.
[56] S. Miro, D. Grebille, D. Chateigner, D. Pelloquin, J.P. Stoquert, J.J. Grob, J.M. Costantini, F. Studer, X-ray diffraction study of damage induced by swift heavy ion irradiation in fluorapatite, Nucl. Instruments Methods Phys. Res. Sect. B Beam Interact. with Mater. Atoms. 227 (2005) 306–318. doi:10.1016/j.nimb.2004.08.025.
[57] P. Scherrer, Estimation of the size and internal structure of colloidal particles by means of röntgen, Nachr. Ges. Wiss. Göttingen. 2 (1918) 96–100.
[58] Y.T. Prabhu, K. Venkateswara Rao, V. Sesha Sai Kumar, B. Siva Kumari, X-ray Analysis of Fe doped ZnO Nanoparticles by Williamson-Hall and Size-Strain Plot, Int. J. Eng. Adv. Technol. 2 (2013) 268–274.
[59] T. Ungár, Strain broadening caused by dislocations, Mater. Sci. Forum. 278–281 (1998) 151–156. doi:10.4028/www.scientific.net/msf.278-281.151.
[60] T. Ungár, I. Dragomir, Á. Révész, A. Borbély, The contrast factors of dislocations in cubic crystals: The dislocation model of strain anisotropy in practice, J. Appl.

Crystallogr. 32 (1999) 992–1002. doi:10.1107/S0021889899009334.
[61] A. Borbély, J. Dragomir-Cernatescu, G. Ribárik, T. Ungár, Computer program ANIZC for the calculation of diffraction contrast factors of dislocations in elastically anisotropic cubic, hexagonal and trigonal crystals, J. Appl. Crystallogr. 36 (2003) 160–162. doi:10.1107/S0021889802021581.
[62] T. Roisnel, J. Rodríquez-Carvajal, WinPLOTR: a windows tool for powder diffraction pattern analysis, in: Mater. Sci. Forum, 2001: pp. 118–123.
[63] D. Balzar, H. Ledbetter, Voigt-function modeling in Fourier analysis of size-and strain-broadened X-ray diffraction peaks, J. Appl. Cryst. 26 (1993) 97–103.
[64] R.A. Young, The Rietveld Method, 1st ed., Oxford University Press, New york, 1995.
[65] L. Lutterotti, Total pattern fitting for the combined size-strain-stress-texture determination in thin film diffraction, Nucl. Instruments Methods Phys. Res. Sect. B Beam Interact. with Mater. Atoms. 268 (2010) 334–340. doi:10.1016/j.nimb.2009.09.053.
[66] L. Lutterotti, P. Scardi, Simultaneous structure and size-strain refinement by the Rietveld method, J. Appl. Crystallogr. 23 (1990) 246–252. doi:10.1107/S0021889890002382.
[67] H. Lutterotti, L and Matthies, S and Wenk, MAUD: a friendly Java program for material analysis using diffraction, Newsl. CPD. 21 (1999) 14–15.
[68] S.M. and H.R.W. L. Lutterotti, Proceeding of the Twelfth International Conference on Textures of Materials (ICOTOM-12), 1999.
[69] R.B. Von Dreele, Quantitative texture analysis by Rietveld refinement, J. Appl. Crystallogr. 30 (1997) 517–525.
[70] N.C. Popa, The (hkl) dependence of diffraction-line broadening caused by strain and size for all Laue groups in Rietveld refinement, J. Appl. Crystallogr. 31 (1998) 176–180.
[71] N.C. Popa, Texture in Rietveld refinement, J. Appl. Crystallogr. 25 (1992) 611–616. doi:10.1107/S0021889892004795.
[72] R. Delhez, T.H. de Keijser, J.I. Langford, D. Louër, E.J. Mittemeijer, E.J. Sonneveld, Crystal imperfection broadening and peak shape in the Rietveld method, in: The Rietveld Method, Oxford University Press Oxford, UK, 1993: p. 132.
[73] M. Wilkens, The determination of density and distribution of dislocations in deformed single crystals from broadened X-ray diffraction profiles, Phys. Status Solidi. 2 (1970) 359–370. doi:10.1002/pssa.19700020224.
[74] M. Wilkens, Theoretical aspects of kinematical X-ray diffraction profiles from crystals containing dislocation distributions, in: R.D.W. and R.B. J. Simmons (Ed.), Fundam. Asp. Dislocation Theory, National Bureau of Standards, Washington, 1970: pp. 1195–1221.
[75] M.A. Krivoglaz, Theory of X-ray and Thermal-neutron Scattering by Real Crystals, 1st ed., Plenum Press, New York, 1969.
[76] M. Isakov, S. Hiermaier, V.T. Kuokkala, Effect of Strain Rate on the Martensitic Transformation During Plastic Deformation of an Austenitic Stainless Steel, Metall. Mater. Trans. A Phys. Metall. Mater. Sci. 46 (2015) 2352–2355. doi:10.1007/s11661-015-2862-z.
[77] R. Alturk, W.E. Luecke, S. Mates, A. Araujo, K.S. Raghavan, F. Abu-Farha, Rate effects on transformation kinetics in a metastable austenitic stainless steel, Procedia Eng. 207 (2017) 2006–2011. doi:10.1016/j.proeng.2017.10.1059.
[78] C.M.C. Ma, T. Lomax, Proton and carbon ion therapy, CRC press, 2012.
[79] J. Ziegler, The Stopping and Range of Ions in Matter, 2–6 (2012). doi:10.1016/B978-0-12-780621-1.50005-8.

[80] R. Sizmann, The effect of radiation upon diffusion in metals, J. Nucl. Mater. 69 (1978) 386–412.
[81] C.L. Xie, E. Nakamachi, Design of texture for improved formability of high-strength steel, Mater. Sci. Eng. A. 340 (2003) 130–138. doi:10.1016/S0921-5093(02)00192-2.
[82] Y. Murata, S. Ohashi, Y. Uematsu, Recent trends in the production and use of high strength stainless steels, ISIJ Int. 33 (1993) 711–720.
[83] A. Kisko, R.D.K. Misra, J. Talonen, L.P. Karjalainen, The influence of grain size on the strain-induced martensite formation in tensile straining of an austenitic 15Cr-9Mn-Ni-Cu stainless steel, Mater. Sci. Eng. A. 578 (2013) 408–416. doi:10.1016/j.msea.2013.04.107.
[84] E. Nagy, V. Mertinger, F. Tranta, J. Sólyom, Deformation induced martensitic transformation in stainless steels, Mater. Sci. Eng. A. 378 (2004) 308–313. doi:10.1016/j.msea.2003.11.074.
[85] P. Mukherjee, P. Barat, T. Jayakumar, P. Kalyanasundaram, C. Rajagopalan, B. Raj, Acoustic emission studies on welded and thermally treated AISI 304 stainless steel during tensile deformation, Scr. Mater. 37 (1997) 1193–1198. doi:10.1016/S1359-6462(97)00228-5.
[86] J.G. Gigax, T. Chen, H. Kim, J. Wang, L.M. Price, E. Aydogan, S.A. Maloy, D.K. Schreiber, M.B. Toloczko, F.A. Garner, Lin Shao, Radiation response of alloy T91 at damage levels up to 1000 peak dpa, J. Nucl. Mater. 482 (2016) 257–265.
[87] J.B. Whitley, G.L. Kulcinski, P. Wilkes, H. V Smith Jr, The depth dependent damage profile in nickel irradiated with nickel or copper ions, J. Nucl. Mater. 79 (1979) 159–169.
[88] K. Shiraishi, K. Fukai, Depth dependent damage profile in stainless steel irradiated with He-ions, J. Nucl. Mater. 117 (1983) 134–142.
[89] C. Se-Hwan, H. Jun-Hwa, K. In-Sup, Damage depth profile and recovery characteristics of 16 MeV proton irradiated 12Cr-1MoV steel, J. Nucl. Mater. 209 (1994) 236–241.
[90] X. Wang, Y. Zhang, S. Liu, Z. Zhao, Depth profiling by Raman spectroscopy of high-energy ion irradiated silicon carbide, Nucl. Instruments Methods Phys. Res. Sect. B Beam Interact. with Mater. Atoms. 319 (2014) 55–61.
[91] M.D. Mathew, B.K. Choudhary, S.K. Albert, Selection of materials for PFBR nuclear steam supply system components. Report-PFBR, 2002.
[92] P.J. Maziasz, Void swelling resistance of phosphorus-modified austenitic stainless steels during HFIR irradiation at 300–500°C to 57 dpa, J. Nucl. Mater. 200 (1993) 90–107. doi:https://doi.org/10.1016/0022-3115(93)90013-O.
[93] H. Lutterotti, L and Matthies, S and Wenk, MAUD (material analysis using diffraction): a user friendly Java program for Rietveld texture analysis and more, in: Proceeding Twelfth Int. Conf. Textures Mater., 1999: p. 1599.
[94] I.W. Chen, Anisotropic diffusion of point defects to edge dislocations, J. Nucl. Mater. 125 (1984) 52–63. doi:10.1016/0022-3115(84)90514-2.
[95] D.A. Hughes, D.C. Chrzan, Q. Liu, N. Hansen, Scaling of misorientation angle distributions, Phys. Rev. Lett. 81 (1998) 4664.
[96] S. Sridhar, H.Y. Sohn, The kinetics of metallurgical reactions, in: S. Seetharaman (Ed.), Fundam. Metal., Woodhead Publishing and Maney Publishing, 2005: pp. 270–349.
[97] H. Yamagata, The science and technology of materials in automotive engines, Elsevier, 2005.
[98] G. Grimvall, Thermophysical properties of materials, Elsevier, 1999.
[99] M.Y. Demeri, Advanced high-strength steels: science, technology, and applications,

ASM international, 2013.
[100] A.P. R. Andersson, E. Schedin, C. Magnusson, J. Ocklund, Proceedings of the 4th European Stainless Steel Science and Market Congress, Paris, 2002.
[101] T.P. P.J.Cunat, Proceedings of the 4th European Stainless Steel Science and Market Congress, Paris, 2002.
[102] G.B. Olson, M. Cohen, A general mechanism of martensitic nucleation: Part I. General concepts and the FCC → HCP transformation, Metall. Trans. A. 7 (1976) 1897–1904. doi:10.1007/BF02659822.
[103] G.B. Olson, M. Cohen, A general mechanism of martensitic nucleation: Part II. FCC→BCC and other martensitic transformations, Metall. Trans. A. 7 (1976) 1897–1904. doi:10.1007/BF02659822.
[104] G.B. Olson, M. Cohen, A general mechanism of martensitic nucleation: Part III. Kinetics of martensitic nucleation, Metall. Trans. A. 7 (1976) 1915–1923. doi:10.1007/BF02659824.
[105] T. Angel, Formation of martensite in austenitic stainless steels, J. Iron Steel Inst. 177 (1954) 165–174.
[106] G.B. Olson, M. Cohen, Kinetics of Strain-Induced Martensitic Nucleation, Metall. Trans. A. 6 (1975) 791–795.
[107] J. Talonen, P. Nenonen, G. Pape, H. Hänninen, Effect of strain rate on the strain-induced γ, → α′-martensite transformation and mechanical properties of austenitic stainless steels, Metall. Mater. Trans. A Phys. Metall. Mater. Sci. 36 A (2005) 421–432. doi:10.1007/s11661-005-0313-y.
[108] L.E. Murr, K.P. Staudhammer, S.S. Hecker, Effects of Strain State and Strain Rate on Deformation-Induced Transformation in 304 Stainless Steel: Part II. Microstructural Study, Metall. Trans. A. 13 (1982) 627–635. doi:10.1007/BF02644428.
[109] S.S. Hecker, M.G. Stout, K.P. Staudhammer, J.L. Smith, Effects of Strain State and Strain Rate on Deformation-Induced Transformation in 304 Stainless Steel: Part I. Magnetic Measurements and Mechanical Behavior, Metall. Trans. A. 13 (1982) 619–626. doi:10.1007/BF02644427.
[110] M. Hokka, Effects of strain rate and temperature on the mechanical behavior of advanced high strength steels, Tampere University of Technology, 2008.
[111] N.I. Vázquez-Fernández, T. Nyyssönen, M. Isakov, M. Hokka, V.T. Kuokkala, Uncoupling the effects of strain rate and adiabatic heating on strain induced martensitic phase transformations in a metastable austenitic steel, Acta Mater. 176 (2019) 134–144. doi:10.1016/j.actamat.2019.06.053.
[112] H.J. Bunge, Texture Analysis in Materials Science, Butterworths, London, 1982.
[113] H.J. Bunge, C. Esling, Quantitative texture analysis, Dtsch. Gesellschaft Fur Met. (1982).
[114] J.M. Alves, L.P. Brandao, A. dos S. Paula, Determination of phases and residual stresses after martensitic transformation induced by rolling in 304L stainless steel, Matéria (Rio Janeiro). 24 (2019).
[115] B.D. Cullity, C.D. Graham, Introduction to magnetic materials, John Wiley & Sons, 2011.
[116] K. Mumtaz, S. Takahashi, J. Echigoya, Y. Kamada, L.F. Zhang, H. Kikuchi, K. Ara, M. Sato, Magnetic measurements of martensitic transformation in austenitic stainless steel after room temperature rolling, J. Mater. Sci. 39 (2004) 85–97. doi:10.1023/B:JMSC.0000007731.38154.e1.
[117] H.M. Ledbetter, Monocrystal-Polycrystal Elastic Constants of a Stainless Steel, Phys. Status Solidi. 85 (1984) 89–96. doi:10.1002/pssa.2210850111.
[118] G. Wassermann, Influence of the α-γ transformation of an irreversible Ni steel onto

crystal orientation and tensile strength, Arch. Eisenhüttenwes. 16 (1933) 647–651.
[119] G. Kurdjumow, G. Sachs, Über den mechanismus der stahlhärtung, Zeitschrift Für Phys. 64 (1930) 325–343.
[120] A.B. Greninger, A.R. Troiano, The mechanism of martensite formation, Trans. AIME. 185 (1949) 590–598.
[121] W.Pitsch, Der Orientierungszusammenhang zwischen Zementit und Austenit, Acta Metall. 10 (1962) 897–900. doi:https://doi.org/10.1016/0001-6160(62)90108-6.
[122] E.C. Bain, The Nature of Martensite, Trans., AIME. 70 (1924) 25–35.
[123] Z. Nishiyama, X-ray investigation of the mechanism of the transformation from face centered cubic lattice to body centered cubic, Sci. Rep. Inst. 23 (1934) 638.
[124] K. Verbeken, L. Barbé, D. Raabe, Evaluation of the Crystallographic Orientation Relationships between FCC and BCC Phases in TRIP Steels, 49 (2009) 1601–1609.
[125] G. Kurdjumow, G. Sachs, Der Mechanismus der Stahlhärtung, Naturwissenschaften. 18 (1930) 534. doi:10.1007/BF01513427.
[126] P. Jacques, Phase transformations in steels Volume 2: Diffusionless transformations, high strength steels, modelling and advanced analytical techniques, Pereloma E, Edmonds D, 1st Ed. UK Woodhead Publ. Ser. Met. Surf. Eng. (2012) 680.
[127] K. Hata, M. Wakita, K. Fujiwara, K. Kawano, T. Tomida, M. Sugiyama, T. Fukuda, T. Kakeshita, In Situ EBSD Analysis on the Crystal Orientation Relationship between Ferrite and Austenite during Reverse Transformation of an Fe-Mn-C Alloy, Mater. Trans. 57 (2016) 1514–1519.
[128] P. Hedström, Deformation and martensitic phase transformation in stainless steels, Luleåtekniska universitet, 2007.
[129] G.B. Olson, A mechanism for the strain-induced nucleation of martensitic transformations, J. Less-Common Met. 28 (1972) 107–118.
[130] M. Humbert, B. Petit, B. Bolle, N. Gey, Analysis of the $\gamma - \varepsilon - \alpha'$ variant selection induced by 10 % plastic deformation in 304 stainless steel at − 60 ◦C, 455 (2007) 508–517. doi:10.1016/j.msea.2006.11.112.
[131] P. Hedström, U. Lienert, J. Almer, M. Odén, Stepwise transformation behavior of the strain-induced martensitic transformation in a metastable stainless steel, Scr. Mater. 56 (2007) 213–216. doi:10.1016/j.scriptamat.2006.10.009.
[132] Y.E. Tian, O.I. Gorbatov, A. Borgenstam, A. V Ruban, P. Hedstro, Austenitic Fe-Cr-Ni Alloys Depending on Stacking Fault Energy, Metall. Trans. A. 48 (2017) 1–7. doi:10.1007/s11661-016-3839-2.
[133] T.-H. Lee, S.-D. Kim, H.-Y. Ha, J.H. Jang, J. Moon, J.-Y. Kang, C.-H. Lee, S.-J. Park, W. Woo, J.-H. Shin, J.-W. Lee, D.-W. Suh, H.-U. Hong, Screw dislocation driven martensitic nucleation: A step toward consilience of deformation scenario in fcc materials, Acta Mater. 174 (2019) 342–350.
[134] D. Fahr, Stress-and strain-induced formation of martensite and its effects on strength and ductility of metastable austenitic stainless steels, Metall. Trans. 2 (1971) 1883–1892.
[135] C.K. Syn, B. Fultz, J.W. Morris, Mechanical stability of retained austenite in tempered 9Ni steel, Metall. Trans. A. 9 (1978) 1635–1640.
[136] E. Nes, Modelling of work hardening and stress saturation in FCC metals, Prog. Mater. Sci. 41 (1997) 129–193. doi:10.1016/S0079-6425(97)00032-7.
[137] A.A. Benzerga, Y. Bréchet, A. Needleman, E. der Giessen, The stored energy of cold work: Predictions from discrete dislocation plasticity, Acta Mater. 53 (2005) 4765–4779.
[138] S. Kolupaeva, M. Semenov, The stored energy of plastic deformation in crystals of face-centered cubic metals, in: IOP Conf. Ser. Mater. Sci. Eng., 2015: p. 12077.

[139] A. Seeger, H. Kronmüller, Stored energy and recovery of deformed FCC metals, Philos. Mag. 7 (1962) 897–913.
[140] J.E. Bailey, The dislocation density, flow stress and stored energy in deformed polycrystalline copper, Philos. Mag. 8 (1963) 223–236.
[141] W.G. Burgers, Recrystallisation power and shear hardening in aluminium single crystals, Nature. 131 (1933) 326–327.
[142] P. Gerber, J. Tarasiuk, T. Chauveau, B. Bacroix, A quantitative analysis of the evolution of texture and stored energy during annealing of cold rolled copper, Acta Mater. 51 (2003) 6359–6371.
[143] C. Deng, S.F. Liu, X.B. Hao, J.L. Ji, Z.Q. Zhang, Q. Liu, Orientation dependence of stored energy release and microstructure evolution in cold rolled tantalum, Int. J. Refract. Met. Hard Mater. 46 (2014) 24–29.
[144] K. Piękoś, J. Tarasiuk, K. Wierzbanowski, B. Bacroix, Use of stored energy distribution in stochastic vertex model, in: Mater. Sci. Forum, 2008: pp. 231–236.
[145] C.S. Barrett, L.H. Levenson, The structure of aluminum after compression, Trans. Aime. 137 (1940) 112–127.
[146] P. Paufler, C.S. Barrett, T.B. Massalski, Structure of Metals. Pergamon Press Oxford, New York, Toronto, Sydney, Paris, Krist. Und Tech. 16 (1981). doi:10.1002/crat.19810160904.
[147] A.L. Etter, M.H. Mathon, T. Baudin, V. Branger, R. Penelle, Influence of the cold rolled reduction on the stored energy and the recrystallization texture in a Fe--53% Ni alloy, Scr. Mater. 46 (2002) 311–317.
[148] N. Rajmohan, Y. Hayakawa, J.A. Szpunar, J.H. Root, Neutron diffraction method for stored energy measurement in interstitial free steel, Acta Mater. 45 (1997) 2485–2494. doi:10.1016/S1359-6454(96)00371-0.
[149] B. Hutchinson, S. Jonsson, L. Ryde, On the kinetics of recrystallisation in cold worked metals, Scr. Metall. 23 (1989) 671–676.
[150] M. Richert, J. Richert, A. Hotloś, W. Pachla, J. Skiba, Structure and properties of copper deformed by severe plastic deformation methods, J. Achiev. Mater. Manuf. Eng. 44 (2011) 50–56.
[151] H.W.F. Heller, C.A. Verbraak, B.H. Kolster, Recrystallization at grain boundaries in deformed copper bicrystals, Acta Metall. 32 (1984) 1395–1406.
[152] A. Mucsi, Recrystallization of pure copper investigated by calorimetry and EBSD, in: Mater. Sci. Forum, 2013: pp. 455–459.
[153] D. Mandal, I. Baker, The influence of grain boundaries on the stored energy of cold-work and recrystallization kinetics, in: Mater. Sci. Forum, 1996: pp. 521–524.
[154] G. Mohamed, B. Bacroix, Role of stored energy in static recrystallization of cold rolled copper single and multicrystals, Acta Mater. 48 (2000) 3295–3302.
[155] Y. Ateba Betanda, A.-L. Helbert, F. Brisset, M.-H. Mathon, T. Waeckerlé, T. Baudin, Measurement of stored energy in Fe–48%Ni alloys strongly cold-rolled using three approaches: Neutron diffraction, Dillamore and KAM approaches, Mater. Sci. Eng. A. 614 (2014) 193–198. doi:https://doi.org/10.1016/j.msea.2014.07.037.
[156] D. Breuer, P. Klimanek, W. Pantleon, X-ray determination of dislocation density and arrangement in plastically deformed copper, J. Appl. Crystallogr. 33 (2000) 1284–1294.
[157] T. Rzychoń, R. K, Microstructure characterization of deformed copper by XRD line broadening, Arch. Mater. Sci. Eng. 28 (2007) 605–608.
[158] K. Piękoś, J. Tarasiuk, K. Wierzbanowski, B. Bacroix, Generalized vertex model of recrystallization--Application to polycrystalline copper, Comput. Mater. Sci. 42 (2008) 584–594.

[159] L. Liu, I. Baker, The dependence of recrystallization temperature and stored energy on rolling strain in polycrystalline copper, Scr. Metall. Mater. 28 (1993) 197–200.
[160] R.D. Doherty, D.A. Hughes, F.J. Humphreys, J.J. Jonas, D.J. Jensen, M.E. Kassner, W.E. King, T.R. McNelley, H.J. McQueen, A.D. Rollett, Current issues in recrystallization: a review, Mater. Sci. Eng. A. 238 (1997) 219–274. doi:https://doi.org/10.1016/S0921-5093(97)00424-3.
[161] J. Schamp, B. Verlinden, J. Van Humbeeck, Recrystallization at ambient temperature of heavily deformed ETP copper wire, Scr. Mater. 34 (1996).
[162] D. Rittel, A.A. Kidane, M. Alkhader, A. Venkert, P. Landau, G. Ravichandran, On the dynamically stored energy of cold work in pure single crystal and polycrystalline copper, Acta Mater. 60 (2012) 3719–3728.
[163] G.R. Stibitz, Energy of lattice distortion, Phys. Rev. 49 (1936) 859.
[164] A. Borbély, J.H. Driver, T. Ungár, An X-ray method for the determination of stored energies in texture components of deformed metals; application to cold worked ultra high purity iron, Acta Mater. 48 (2000) 2005–2016.
[165] C.V.S. Lim, Length scale effect on the microstructural evolution of copper layers in a roll-bonded copper-niobium composite, Carnegie Mellon University, 2008.
[166] W. Zhou, Z.L. Wang, Scanning microscopy for nanotechnology: techniques and applications, Springer science & business media, 2007.
[167] S. Wronski, J. Tarasiuk, B. Bacroix, K. Wierzbanowski, H. Paul, Microstructure heterogeneity after the ECAP process and its influence on recrystallization in aluminium, Mater. Charact. 78 (2013) 60–68.
[168] M.B. Bever, R. Maddin, Creep and recovery, ASM, Clevel. (1957) 14–15.
[169] M.B. Bever, D.L. Holt, A.L. Titchener, The stored energy of cold work, Prog. Mater. Sci. 17 (1973) 5–177.
[170] A.L. Titchener, M.B. Bever, The stored energy of cold work, Prog. Met. Phys. 7 (1958) 247–338.
[171] P.A. Beck, Annealing of cold worked metals, Adv. Phys. 3 (1954) 245–324.
[172] R. De Angelis, T. Snyder, J. House, W. Hosford, Quantitative description of fiber textures in cubic metals, Adv. X-Ray Anal. 42 (2000) 510–520.
[173] T.L. Richards, S.F. Pugh, H.J. Stokes, The kinetics of recovery and recrystallization of copper from hardness and thermoelectric-power measurements, Acta Metall. 4 (1956) 75–83.

Thesis Highlight

Name of the Student: Shri Santu Dey **Enrolment No.:** PHYS04201304011

Name of the CI/OCC: VECC, Kolkata

Thesis Title: Study of effect of deformation & irradiation on the microstructure of fcc materials using X-ray diffraction

Discipline: eg. Physical Sciences **Sub-Area of Discipline:** Material Science

Date of viva voce: 18/12/2020

Microstructure of a material strongly influences some of its major physical and mechanical properties. This can in principle be controlled during the metal forming process (which includes both deformation and annealing) or may get altered in service conditions (which includes deformation, irradiation etc). The effect of such changes on the physical properties may be either beneficial or detrimental. To achieve the desired final properties of the material for a particular application and to understand the changes during in-service conditions, a thorough knowledge of the material should be gathered beforehand.

In this thesis, some of the relevant but so far unaddressed problems related to deformation and irradiation phenomena in face centered cubic (fcc) materials have been studied using detailed X-ray diffraction detail X-ray line profile analysis techniques in order to understand in-depth the microstructural changes in the materials to varying levels of complexity.

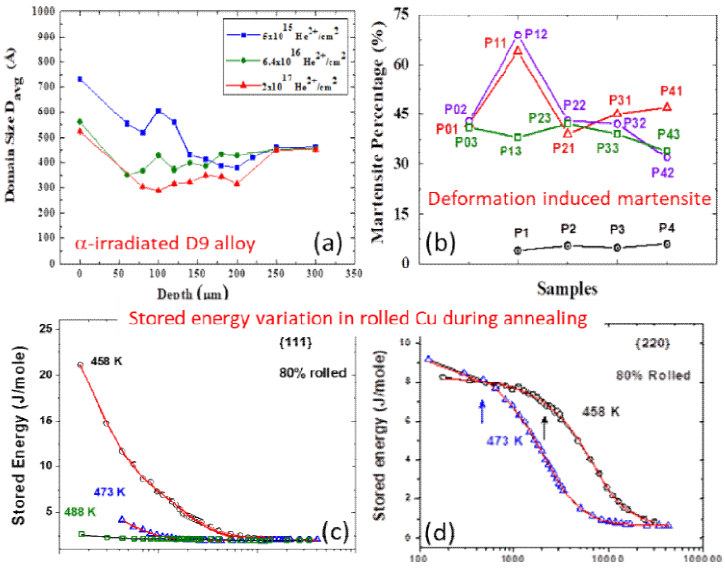

(a) Depth wise variation of domain size in α-irradiated D9 alloy; (b) Variation of martensite percentage with different pre-strain and pre- & post-strain rates; (c) and (d) Stored energy variation with time along {111} and {220} peaks of rolled Cu at different temperatures.

The three main problems that have been addressed in this study are: (i) Defects diffusion in ion irradiated materials to understand the importance of radiation enhanced diffusion; (ii) Deformation induced phase transformation and the dependence of deformation path history and (iii) Nature of defects dynamics along different crystallographic planes during annealing of a deformed material. The choice of the material to carry out the individual studies was based on the property of the material and its relevance in the different applications. Alloy D9, SS304 and electrolytic Copper were chosen to carry out the studies respectively.